



Dipl.-Ing. Patricia Monika Handel, BSc

Investigations of Next Generation Cathodes and Thermal Aging Effects of Electrolytes in Lithium-Ion Batteries

DOCTORAL THESIS

to achieve the university degree of
Doktorin der technischen Wissenschaften
submitted to

Graz University of Technology

Supervisor

Univ.-Prof. Dipl.-Chem. Dr.rer.nat. Frank Uhlig

Institute for Inorganic Chemistry

In cooperation with VARTA Micro Innovation GmbH

Company supervisor: Dr. techn. Christoph Stangl

Graz, July 2015

AFFIDAVIT

I declare that I have authored this thesis independently, that I have not used other than the declared sources/resources, and that I have explicitly indicated all material which has been quoted either literally or by content from the sources used. The text document uploaded to TUGRAZonline is identical to the present doctoral thesis.

Date

Signature

„Every mountain top is within reach if you just keep climbing.“

(Barry Finlay)

Acknowledgement

I would like to take the opportunity to express my sincere thanks to all those who have contributed to the success of this PhD thesis.

First and foremost I would like to express my appreciation and thanks to my advisor Univ.-Prof. Dr. Frank Uhlig, head of the Institute for Inorganic Chemistry, for giving me the opportunity to perform this thesis under his supervision and for donating me theoretical support within the last three years. I would also like to give thanks to Univ.-Prof. Dr. Ferdinand Hofer, head of the Institute for Electron Microscopy and Nanoanalysis (FELMI), for assuming the tasks as second assessor.

I would like to express my gratitude to Dr. Stefan Koller, CEO of VARTA Micro Innovation (VMI) GmbH for provision of financial support, expertise and excellent laboratory equipment. Furthermore, I would like to thank Dr. Christoph Stangl, my project manager, for his guidance and support through all these years. He was always on hand with help and valuable advice, not least when performing the four point resistivity measurements.

Further, I would like to express my gratitude and my warmest wishes to all my colleagues VMI GmbH for their willingness to help and the good working atmosphere. I am indeed grateful to Ing. Katja Kapper, Dipl.-Ing. Gisela Fauler, Dr. Martin Schmuck and Dr. Christoph Stangl for their patience and time that they provided me during the initial training phase as PhD. I would like to extend my gratitude to Dr. Colin God for his extensive expertise, his encouragement and his brilliant ideas. Once again, I owe special thanks to Ing. Katja Kapper and Dipl.-Ing. Gisela Fauler for their practical assistance and advices throughout my time as PhD. For scientific and non-scientific discussions as well as for becoming friends within the last years I would like to thank Dipl.-Ing. Katharina Gruber, Dr. Sandra Pötz and Dr. Michaela Scharfegger. I wish to express my gratitude also to MSc. Pierre Baumann, Ing. Christian Baumann, Ing. Stephania Toulis, Andrea Droisner, Dr. Harald Kren, Dr. Bernd Fuchsbichler and Christian Lenardt.

Additionally, I want to thank all scientific and non-scientific employees at Institute of Inorganic Chemistry as well as at the Institute of Chemistry and Technology of Materials for the good cooperation and the great time. In particular, I would like to thank Oberraetin Dr. Brigitte Bitschnau and Univ.-Prof. Dr. Franz-Andreas Mautner for their help with the XRD measurements and analysis of the XRD diagrams. My special thanks also go to Monika Filzwieser for performing the elemental analysis, Dr. Helmar Wiltsche for carrying out the ICP-OES measurements and Ing. Hartmuth Schroettner for recording of the SE-BSE images.

Lastly, I would like to express my thanks to all my family and my friends. Special thanks are directed to my mother, Ingrid Handel, who has supported me through my whole life and Ing. Christian Gejer, to whom my heart belongs.

Abstract

Concerning prospective energy storage in hybrid and battery electric vehicles, lithium-ion batteries (LIBs) are one of the most outstanding technologies due to their high energy density as well as great cycle stability. However, before a systematic replacement of fossil fuels proceeds, the achievement of high energy densities and acceptable life time of LIBs must be granted to be able to compete with the driving ranges of combustion engines.

One possibility to enhance the energy density is the application of high voltage cathode materials. Hence, one aim of this doctoral thesis is the development of an energy-saving, microwave-assisted solvothermal synthesis of phospho-olivines and solid solutions thereof like LiMPO_4/C , $\text{LiMM}'\text{PO}_4/\text{C}$ and $\text{LiMM}'\text{M}''\text{PO}_4/\text{C}$ (M= Fe, Mn, Co). This synthesis method is compared to a conventional solid state procedure. The physical properties of all synthesized materials are analyzed and their influence on electrochemical performance is investigated. It has been noticed that there is a correlation between solid solution formation and the different steps within material preparation. The solid solution formation of $\text{LiFe}_x\text{Mn}_{1-x}\text{PO}_4/\text{C}$ as well as $\text{LiFe}_x\text{Mn}_y\text{Co}_{1-x-y}\text{PO}_4/\text{C}$ definitely improves the electrochemical performance compared to LiMnPO_4/C and LiCoPO_4/C . A trend regarding the isovalent doping of $\text{LiFe}_x\text{Mn}_{1-x}\text{PO}_4/\text{C}$ and higher stability of the cell against high charge and discharge rates becomes apparent.

Not only the hydrolysis sensitivity, but also the thermal instability of the most common conductive salt lithium hexafluorophosphate LiPF_6 in the presence of organic carbonates is directly connected to the cycle stability and cycle life of the LIB. Therefore, another scope of this thesis is the characterization of a thermally aged state-of-the-art electrolyte as well as its impact on the electrochemical performance in a LIB. A measurement setup is developed that avoids the external influences on the thermal electrolyte degradation. The applied analysis techniques show that n-SiO₂ powder and glassware (e.g Duran®) definitely promote the electrolyte decomposition, whereby also polypropylene of the pouch bag is partly degraded. Even the addition of n-Si powder leads to an enhancement of the thermal electrolyte degradation. Hence, its application as anode material might be problematic. As far as glass surface is absent, the addition of protic impurities mainly leads to the development of hydrofluoric acid HF and difluoro phosphoric acid $\text{O}=\text{PF}_2(\text{OH})$. The influence of the thermally aged electrolyte on the electrochemical performance can be ascertained due to the assembly of battery test cells. This method is still used to study the influence of different battery components on the thermal aging of the electrolyte and their consequences for electrochemical performance.

Kurzfassung

Aufgrund ihrer vergleichsweise hohen Energiedichte und Zyklenfestigkeit gelten Lithium-Ionen-Batterien (LIBs) als eine der bedeutsamsten Technologien zur elektrochemischen Energiespeicherung in Hybrid- und Elektrofahrzeugen. Bevor jedoch ein systematischer Ersatz fossiler Brennstoffe erfolgen kann, müssen hohe Energiedichten sowie eine akzeptable Lebensdauer der LIBs gewährleistet sein, um mit den Reichweiten von Verbrennungsmotoren in Konkurrenz treten zu können.

Eine Möglichkeit, deren Energiedichte zu erhöhen, stellt die Applikation von Hochvolt-Kathodenmaterialien dar. Deshalb ist ein Ziel dieser Dissertationsarbeit die Entwicklung einer energiesparenden und mikrowellenunterstützten Solvothermalsynthese von (Misch)Phosphaten LiMPO_4/C , $\text{LiMM}'\text{PO}_4/\text{C}$ und $\text{LiMM}'\text{M}''\text{PO}_4/\text{C}$ ($\text{M} = \text{Fe}, \text{Mn}, \text{Co}$). Diese Synthesemethode wird mit einer konventionellen, festkörperchemischen Synthesemethode verglichen. Alle synthetisierten Materialien werden hinsichtlich ihrer physikalischen Eigenschaften untersucht und deren Auswirkung auf die elektrochemische Performance getestet. Eine Abhängigkeit der Mischkristallbildung zwischen Übergangsmetallen von den unterschiedlichen Schritten in der Präparationsmethode kann festgestellt werden. Die Mischkristallbildung verbessert eindeutig die elektrochemische Performance von $\text{LiFe}_x\text{Mn}_{1-x}\text{PO}_4/\text{C}$ sowie $\text{LiFe}_x\text{Mn}_y\text{Co}_{1-x-y}\text{PO}_4/\text{C}$ im Vergleich zu LiMnPO_4/C sowie LiCoPO_4/C . Es zeigt sich, dass isovalentes dotieren von $\text{LiFe}_x\text{Mn}_{1-x}\text{PO}_4/\text{C}$ die Stabilität der Zelle gegenüber hohen Lade- und Entladeraten erhöht.

Nicht nur die Hydrolyseempfindlichkeit, sondern auch die thermische Instabilität des gebräuchlichsten Leitsalzes Lithiumhexafluorophosphat LiPF_6 in Gegenwart von organischen Carbonaten steht im direkten Zusammenhang mit der Zyklenfestigkeit sowie der Lebensdauer von LIBs. Daher stellt ein weiteres Ziel dieser Arbeit die Charakterisierung der thermisch bedingten Alterung eines konventionellen Elektrolyten sowie dessen Auswirkung auf das elektrochemische Verhalten von LIBs dar. Es kann ein Messsetup entwickelt werden, das die Einwirkung äußerer Einflüsse auf die thermische Elektrolytalterung exkludiert. Mit den angewandten Analysetechniken zeigt sich, dass $n\text{-SiO}_2$ Pulver sowie Glas (z.B. Duran®) die Elektrolytalterung signifikant beschleunigen, wobei auch die Polypropylenschicht der Verbundfolie teilweise angegriffen wird. Auch die Zugabe von $n\text{-Si}$ Pulver führt zu einer Erhöhung der thermischen Elektrolytzersetzung. Daher können Probleme beim Einsatz als Anodenmaterial entstehen. Die Zugabe von protischen Verunreinigungen führt hauptsächlich zur Entstehung von Flusssäure HF sowie auch Difluorosphorsäure $\text{O}=\text{PF}_2(\text{OH})$, sofern der Einfluss von Glasoberfläche vermieden wird. Durch die Assemblierung von Batterietestzellen kann die Auswirkung der thermisch gealterten Elektrolyten auf die elektrochemische Performance festgestellt werden. Der Einfluss unterschiedlicher Batteriekomponenten auf die thermische Elektrolytalterung sowie deren Konsequenzen für die elektrochemische Performance wird weiterhin mittels dieser Methode untersucht.

Table of Contents

1	INTRODUCTION.....	1
2	THEORETICAL BACKGROUND	4
2.1	The galvanic cell	4
2.1.1	About the lead-acid battery, electrochemical series of metals and Nernst equation.....	5
2.1.2	Thermodynamic and kinetic basics.....	7
2.1.3	Glossary	11
2.2	Lithium-ion battery	13
2.2.1	Brief historical development	13
2.2.2	Active materials for LIBs	14
2.2.2.1	Carbonaceous materials as negative electrode materials	15
2.2.2.2	Other feasible negative electrode materials	17
2.2.2.3	One-dimensional positive electrode materials.....	19
2.2.2.4	Two- and three-dimensional positive electrode materials.....	22
2.2.2.5	Prospective materials for the positive electrode.....	24
2.2.3	Electrolytes for LIBs	26
2.2.3.1	About the degradation of state-of-the-art electrolytes.....	29
2.2.3.2	Negative electrode/electrolyte interface and its fading mechanisms.....	31
2.2.3.3	Positive electrode/electrolyte interface, causes for capacity fading and Mn ²⁺ -dissolution	34
2.2.4	Separators for liquid electrolyte LIBs	36
2.2.5	Strategies for increasing the energy density of LIBs and summary of their functional principle	37
3	EXPERIMENTAL.....	39
3.1	Synthesis and characterization of phospho-olivines LiMPO₄ (M= Fe, Mn Co).....	39
3.1.1	Solid state synthesis of LiFe _{0.5} Mn _{0.5} PO ₄	39
3.1.2	General procedure for microwave-solvothermal synthesis of LiFePO ₄ , LiMnPO ₄ and LiFe _x Mn _{1-x} PO ₄ and doping thereof.....	39
3.1.3	Towards high voltage positive electrode materials.....	41
3.1.4	Measurement methods and setups for positive electrode materials	42
3.2	Thermal aging of a state-of-the-art LIB electrolyte.....	45
3.2.1	General procedure.....	45
3.2.2	Measurement methods and setups for electrolyte aging	46
4	RESULTS AND DISCUSSION.....	49

4.1	Synthesis and characterization of next generation cathodes for LIBs	49
4.1.1	Solid state synthesis versus solvothermal microwave assisted synthesis.....	49
4.1.2	Solvothermal microwave assisted synthesis	52
4.1.2.1	Tuning of the synthesis process.....	52
4.1.2.2	Structural chemistry and electrochemical behavior of $\text{LiFe}_x\text{Mn}_{1-x}\text{PO}_4/\text{C}$ ($x= 0, 0.1, \dots 1$)	56
4.1.2.3	Preparation details with focus on the solid solution formation determining step.....	64
4.1.2.4	Isovalent doping of equimolar $\text{LiFeMnPO}_4/\text{C}$	68
4.1.2.5	Towards high voltage positive electrode materials $\text{LiFe}_x\text{Mn}_y\text{Co}_{1-x-y}\text{PO}_4$	73
4.1.3	Conclusion and outlook	79
4.2	Aging behavior of a state-of-the-art LIB electrolyte	82
4.2.1	Aging caused by packaging materials	83
4.2.1.1	Glassy surface	83
4.2.1.2	Polymer surface	85
4.2.2	Aging caused by protic impurities	86
4.2.2.1	Deionized water	86
4.2.2.2	Undried positive electrode material (LFP)	89
4.2.3	Aging caused by silicon species	90
4.2.3.1	n-SiO ₂ powder (Dried and undried)	90
4.2.3.2	n-Si powder	94
4.2.4	Electrochemical behavior of aged electrolytes	95
4.2.4.1	Pouch cells with industrially manufactured electrodes.....	95
4.2.4.2	Electrochemical performance of LFMP/C half cells containing the aged electrolytes	99
4.2.5	Conclusion and Outlook.....	101
5	APPENDIX.....	103
5.1	List of Chemicals.....	103
5.2	List of Programs for CC experiments	104
5.3	References	105
5.4	Parts of publication of the doctoral thesis	113

List of Abbreviations

BEV	Battery electric vehicle
BSE	Back scattered electrons
CC	Galvanostatic cycling
CCCV	Constant current constant voltage cycling
CV	Cyclic voltammetry
δ	Chemical shift / ppm
ΔG	Gibbs free energy / J mol ⁻¹
DEC	Diethylene carbonate
DMC	Dimethyl carbonate
E	Potential / V
E^0	Standard Potential / V
EC	Ethylene carbonate
EDX	Energy dispersive X-ray analysis
EI	Electron ionization
EDL	Electrical double layer
GC-MS	Gas-chromatography mass-spectrometry
GITT	Galvanostatic intermittent titration technique
HF	Hydrofluoric acid
HS-GC-MS	Headspace gas-chromatography mass-spectrometry
ICP-OES	Inductively coupled plasma optical emission spectrometry
ICSD	Inorganic crystal structure database
J	Coupling constant / Hz
LCP	Lithium cobalt phosphate, LiCoPO ₄
LFP	Lithium iron phosphate, LiFePO ₄
LFMP	Lithium iron manganese phosphate, LiFe _x Mn _{1-x} PO ₄
LFMCP	Lithium iron manganese cobalt phosphate, LiFe _x Mn _y Co _{1-x-y} PO ₄

LIB	Lithium-ion secondary battery
LMO	LiMn_2O_4
LMP	Lithium manganese phosphate, LiMnPO_4
m	Multiplicity
M	Molarity / mol L^{-1}
MW	Microwave
NCA	$\text{LiNi}_{0.8}\text{Co}_{0.15}\text{Al}_{0.05}\text{O}_2$
NHE	Normal hydrogen electrode
NMC	$\text{LiNi}_{1/3}\text{Mn}_{1/3}\text{Co}_{1/3}\text{O}_2$
NMP	N-Methyl-2-pyrrolidone
NMR	Nuclear magnetic resonance
n-Si	Silicon nano-particles
n-SiO ₂	Silicon dioxide nano-particles
OCV	Open circuit voltage / V
PEO	Polyethylene oxide
ppm	Parts per million
PVDF	Polyvinylidene fluoride
RF	Alkyl fluorides
rpm	Rounds per minute
SE	Secondary electrons
SEI	Solid electrolyte interphase
SEM	Scanning electron microscopy
SOC	State of charge / %
TC	Tungsten carbide
TEG	Tetraethylene glycol
UV-Vis	Ultraviolet-visible
XRD	X-ray powder diffraction

1 Introduction

As delicacy wielded in French cuisine, frog legs were often fried until crisp, seasoned and served on a plate with a slice of lemon. Provided that an electrochemist observes the citron as well as the frog legs with his profound expertise, he would definitely talk shop about Luigi Galvani and Alessandro Volta, metals, electrolytes and the electrochemical cell. Whereas it is possible that Parthians and Egyptians already applied electroplating long before Christ, the first recorded proof accrued in 1791 [1][2]: Luigi Galvani realized that frog legs showed movement once they got in touch with two different metals. Only his interpretation was misleading, since he attributed this movement to ‘*animal electricity*’.

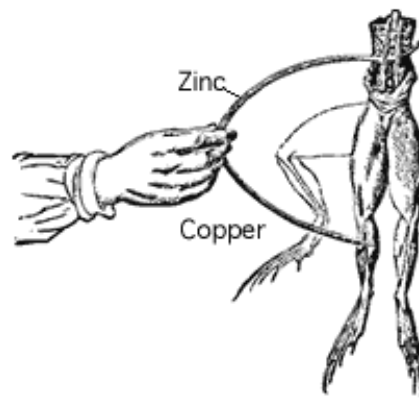


Figure 1: Graphic representation of Galvani's frog leg experiment [2].

Alessandro Volta instead found out that the movement of the leg was caused by the flow of electrical current and developed the voltaic pile in 1800 [1][3]. This first battery consisted of stacked zinc and copper electrodes, which were linked externally through a wire and separated by salt solution soaked cardboard slices. Growing interest in the galvanic processes led to the development of the first device that produced electricity uniformly. This so-called Daniell Element was developed in 1836. In 1859 the lead-acid battery, which is used until today, was invented by Gaston Planté, followed by a lot of different cell chemistries. Just to mention a few of them, Leclanché cells, nickel-cadmium batteries Ni-Cd, alkaline batteries and nickel metal hydride Ni-MH batteries were explored. All of them used an aqueous electrolyte and thus theoretic stability was limited up to $1.23 V_{\text{NHE}}$ [4] due to the decomposition of water. This limit might be exceeded by e.g. the formation of a corrosion film of lead within the lead-acid battery [5]. During the 20th century, the lead-acid and the nickel-cadmium battery became the most widespread applications [6]. Nevertheless, the steady demand of an increase in energy density and the application of high voltage electrode materials force the battery community to the development of electrolytes other than aqueous ones.

Thereafter, the demand of portable electronic devices was steadily increasing. Moreover, utmost interest evoked in the replacement of internal-combustion engines by electrically driven vehicles due to environmental concerns. For this application, new technologies with higher energy and power densities were needed. The breakthrough of the lithium-ion secondary battery LIB ($\text{Li}_x\text{C}_6/\text{non-aqueous liquid electrolyte}/\text{Li}_{1-x}\text{CoO}_2$) in 1991 by Sony Corporation [7] puts other technologies steadily out of the market due to its favorable high gravimetric and volumetric energy density. Since then a lot of research activities have focused on the advancement of the LIB. The capacity of the first 18650¹

¹ Meaning that the casing of the cell has a diameter of 18 mm and a length of 65 mm.

LIB cell could be improved from 0.9 Ah to 2.6 Ah till 2012 [8]. Nowadays, this cell format is able to reach a capacity of 3.35 Ah [9]. Figure 2 gives an overview of the power and energy densities of different energy storage systems. It is evident that full performance battery electric vehicles (FPBEV) can only be realized by the application of LIBs. Full hybrid electric vehicles (HEV) can either be driven by Ni-Cd or Ni-MH, whereas plug-in hybrid electric vehicles (PHEV) need the energy supply from at least Ni-MH.

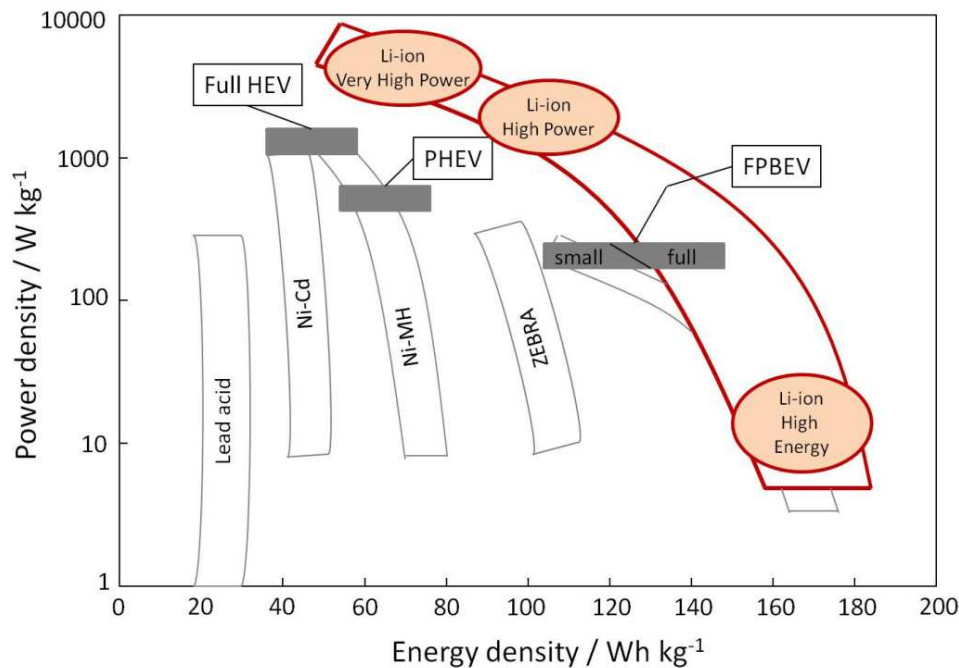


Figure 2: Ragone Plot. Redrawn and modified from [10].

As suggested by the international energy agency’s (IEA) world energy outlook 2014 [11], the energy requirements will increase by 37 % until 2040. To diminish the global warming and decrease the carbon emissions through replacing combustion engines by battery electric vehicles (BEV), the total environmental impact of the LIB in BEVs (cf. eq. 1) needs to be considered [12] [13].

$$I_{LIB} = \sum_{Components} Chemical\ composition + \sum_{Components} Synthesis\ process + \sum_{Components} Implementation\ in\ the\ system + \sum_{Components} Recycling \tag{eq. 1}$$

I Total environmental impact of the LIB

Other important factors influencing the commercialization of LIBs in BEVs are their lifetime, costs and energy density [14]. The publication „The electrification of the Vehicle and the Urban Transport System” [15] from EUCAR, summarizes important prerequisites for the use of LIBs in BEVs until 2020 (cf. Table 1).

Table 1: Comparison of the prerequisites of LIBs for the application in BEV.

	2015	2020
Energy density / Wh kg⁻¹	150	200
Lifetime	-	15 years or 5000 deep charge/discharge cycles
Costs / € kWh⁻¹	300	150
Driving range / km	150 / 250*	200 / 300*

*Under ideal conditions

Within this thesis the focus is on decreasing the energy input and costs during production of positive electrode materials for LIBs. Therefore, an energy saving synthesis method is shown for next generation positive electrode materials. Microwave-solvothermal synthesis is used to obtain doped and undoped $\text{LiFe}_x\text{Mn}_{1-x}\text{PO}_4$ (with $x = 0, 0.1, 0.2, \dots 1.0$). Carbon coating of the samples leads to a superior electrochemical performance. The ideal value for x is determined as 0.5 molar equivalents. It turned out that solid solution formation between Fe and Mn within the phospho-olivine crystal lattice greatly depends on the preparation method. A detailed XRD study on synthesized phospho-olivine powders is demonstrated. To further enhance the energy density of next generation positive electrode materials, partial substitution of Fe occurs not only with Mn, but also with Co.

Since these next generation positive electrode materials generally possess a higher operating voltage compared to the state-of-the-art cathodes, it is crucial that the electrochemical stability window of the electrolyte ensures a safe and long cycle life performance of the LIB. Latter greatly depends on the condition and composition of the electrolyte. Further, the utilization of manganese in next generation positive electrode materials might lead to a higher energy density of the LIB since the redox potential of $\text{Mn}^{2+}/\text{Mn}^{3+}$ is higher compared to $\text{Fe}^{2+}/\text{Fe}^{3+}$. Anyway, the substitution of iron with manganese can trigger additional aging effects, caused by well-known dissolution of Mn^{2+} -ions into the electrolyte. Further enhancement is possible by traces of HF, which could be contained in the electrolyte as adsorbed species on the conductive salt LiPF_6 or develop through infiltration of water by insufficient drying of active materials. All these effects are enhanced at elevated temperatures and therefore, the application of LIBs is limited to a certain temperature range.

To examine the thermal degradation of state-of-the-art electrolytes used in LIBs, existing methods are first evaluated and further developed. Another scope of this work is to present a method that ensures that the environmental impact on thermal electrolyte aging such as e.g. housing materials is avoided. Therefore, this method allows the identification of key factors, which influence the thermal degradation of state-of-the-art electrolytes used in LIBs. The thermal degradation products in the electrolyte are presented to achieve profound understanding for an enhancement of the cycle life and safety of the LIB. Further, the influence of thermal aging on the electrochemical performance of the LIB is shown by the assembly of battery test cells.

2 Theoretical Background

2.1 The galvanic cell

The basic principle of every electrochemical cell is the donation and acceptance of electrons, termed as oxidation and reduction, respectively. These redox-reactions occur either in electrolytic or in galvanic cells². The main difference between these cell types is that redox-reactions happen spontaneously for galvanic cells (ΔG is negative), whereas electrolysis needs the supply of electrical energy (ΔG is positive) [16].

The conversion of chemical energy in electrical energy in galvanic cells leads to the generation of a current. To gain higher capacity or higher voltage from these cells, they are connected parallel and in series, respectively. The connection of cells is referred to as battery. Galvanic cells are divided into three different cell types [16][17]:

- ◆ *Primary cells:* This cell type can only be discharged once. The electrochemical reaction is irreversible and hence they are not rechargeable. Alkaline manganese dioxide batteries and zinc carbon batteries are two examples with a non-rechargeable mechanism.
A special case of primary cells are reverse cells, wherein one part is not active when the cells are assembled. Usually, the electrolyte is separated from the other cell parts. The battery becomes active as soon as the electrolyte is released by e.g. heat.
- ◆ *Secondary cells:* After discharge, the cells are charged by an external electrical force. The electrical potential applied to the cell needs to be at least as high as the standard potential ΔE^0 of the entire cell to achieve the initial situation. Since the electrochemical reaction is reversible, these cells are termed as rechargeable. Secondary cells are e.g. lithium-ion batteries or nickel-metal hydride batteries.
- ◆ *Fuel cells:* Whereas primary and secondary cells are closed systems, fuel cells need a steady supply of fuel such as e.g. hydrogen and oxygen.

Generally, galvanic cells consist of three parts: the positive electrode, the negative electrode and the electrolyte [1][17]. The electrode, where reduction occurs during discharge, is further called positive electrode or cathode. The counterpart (negative electrode or anode) is the electrode, which is oxidized during discharge. Even if the oxidation and reduction reactions are reversed upon charging, and therefore the term cathode and anode should be swapped, most literature about LIBs still uses cathode for the positive and anode for the negative electrode. Therefore, this terminology is adopted within this thesis. The electrolyte is ionically conductive and electronically insulating. Therefore, its task is to deliver ions between the positive and negative material upon charge and discharge,

² Herein, the term „cell” is used as the smallest unit of a battery.

whereas electrons move through the external circuit. The operation mode for a rechargeable battery is shown based on a lead-acid cell chemistry (cf. chapter 2.1.1). This cell is chosen since its application lasts until today as a connection in series of six cells to constitute the 12 V automotive battery. Anode, cathode and electrolyte for a lithium-ion battery will be discussed more precisely in chapter 2.2.2 and 2.2.3.

2.1.1 About the lead-acid battery, electrochemical series of metals and Nernst equation

The first secondary battery was invented in 1859 [1] by Raymond Gaston Planté and was further modified by Camille Alphonse Faure in 1881. This lead-acid battery is composed of lead as negative electrode, lead dioxide as positive electrode and sulfuric acid as electrolyte.

According to Figure 3, lead is oxidized to lead sulfate and lead dioxide is reduced to lead sulfate during the discharging of the lead-acid battery. Electrons move through the external circuit from the anode to the cathode. The charging of the battery takes place if an external load is applied and hence the reaction is reversed.

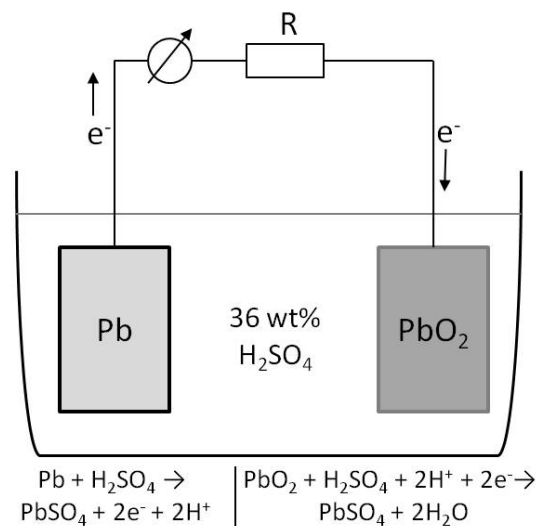
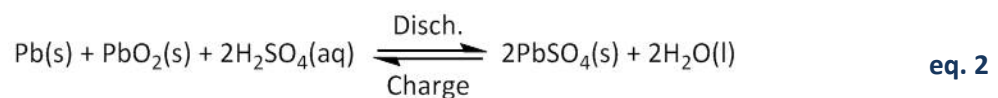
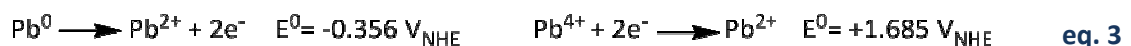


Figure 3: Schematic illustration of the discharge mode of a lead-acid battery. Redrawn from [18].

The overall reactions for discharge and charge are:



Regarding following equations,



Pb^0 and Pb^{4+} are the main participants of the charge-transfer reaction. Their standard potential E^0 for the oxidation reaction is $-0.356 \text{ V}_{\text{NHE}}$ and $+1.685 \text{ V}_{\text{NHE}}$ for Pb^0 and Pb^{4+} , respectively. Since it is

impossible to directly measure standard electrode potentials of a single half cell, a reference electrode system needs to be applied. Most commonly, the normal hydrogen electrode (NHE) is used for this purpose and its potential is set as zero. Table 2 lists the standard potential of some metals measured against NHE under standard conditions. By means of the electrochemical series of metals, it is predictable, which metal will be oxidized and which one will be reduced in a galvanic cell. Zn, for example, has a more negative E^0 compared to Cu. Therefore, Zn is oxidized more easily and reduces Cu.

The standard potential at equilibrium condition ΔE^0_{Cell} of the lead-acid cell can be calculated by following equation:

$$\Delta E^0_{\text{Cell}} = E^0_{\text{Cathode}} - E^0_{\text{Anode}} = 1.685 - (-0.356) = \underline{\underline{2.04V}} \quad \text{eq. 4}$$

Table 2: Electrochemical series of metals against NHE at 298 K, 101.325 kPa and an activity of the components of 1 [16] [18].

Half cell	Electrode reaction	E^0 / V_{NHE}
Li/Li ⁺	Li ⁺ + e ⁻ ⇌ Li	-3.045
K/K ⁺	K ⁺ + e ⁻ ⇌ K	-2.924
Na/Na ⁺	Na ⁺ + e ⁻ ⇌ Na	-2.711
Mg/Mg ²⁺	Mg ²⁺ + 2e ⁻ ⇌ Mg	-2.38
Al/Al ³⁺	Al ³⁺ + 3e ⁻ ⇌ Al	-1.706
Zn/Zn ²⁺	Zn ²⁺ + 2e ⁻ ⇌ Zn	-0.763
Fe/Fe ²⁺	Fe ²⁺ + 2e ⁻ ⇌ Fe	-0.409
Ni/Ni ²⁺	Ni ²⁺ + 2e ⁻ ⇌ Ni	-0.23
Pb/Pb ²⁺	Pb ²⁺ + 2e ⁻ ⇌ Pb	-0.126
Pt/H ₂ H ⁺ aqu.	2H ⁺ + 2e ⁻ ⇌ H ₂	0
Cu/Cu ²⁺	Cu ²⁺ + 2e ⁻ ⇌ Cu	+0.340
Ag/Ag ⁺	Ag ⁺ + e ⁻ ⇌ Ag	+0.7996
Au/Au ⁺	Au ⁺ + e ⁻ ⇌ Au	+1.42

Considering Table 2, it is conspicuous that E^0 for Pb⁰ in the lead-acid battery (cf. eq. 3) differs from E^0 included within this table. The high concentration of H₂SO₄ shows a non-ideal behavior and it is difficult to use previously mentioned standard conditions for the equilibrium of this cell chemistry. Further, there is a concentration dependence of the sulfuric acid on the state of charge of the battery. Therefore, activity of sulfuric acid differs due to the alteration of the specific gravity of the electrolyte [19]. The relationship between activities of the cell components, standard electrode potential E^0 and temperature T is given by the Nernst equation:

$$E = E^0 + 2.303 \times \frac{R \times T}{z \times F} \times \log \frac{a_{Ox}}{a_{Red}} \quad \text{eq. 5}$$

E Potential / V
*E*⁰ Standard potential / V
R Universal gas constant / 8.3145 J K⁻¹ mol⁻¹
T Temperature /K
z Number of electrons exchanged
F Faraday constant / 96485 C mol⁻¹
*a*_{Ox} or *a*_{Red} Activities of oxidized or reduced species

By using eq. 5 it is possible to calculate the potential of the lead-acid battery at different acid concentrations. Therefore, the potential can be calculated for other conditions than standard conditions.

2.1.2 Thermodynamic and kinetic basics

The potential of galvanic cells can either be measured directly or calculated with the aid of thermodynamic data. Within this chapter some thermodynamic basics of galvanic cells are treated [16][17][18][20][21]. The Gibbs-Helmholtz equation plays a key role in thermodynamics that describes the equilibrium of a chemical reaction and its preferential reaction process.

$$\Delta G = \Delta H - T \times \Delta S \quad \text{eq. 6}$$

ΔG Gibbs free energy or rather utilizable electric energy / J mol⁻¹
ΔH Reaction enthalpy / J mol⁻¹
T × ΔS Product of temperature and entropy / J

A change in the Gibbs free energy is the driving force for the release of electrons into an external circuit upon discharging of a galvanic cell. If equilibrium conditions, thus an infinitesimal current and the same concentration of oxidation and reduction species occur inside the cell, eq. 6 can be defined for the standard free energy ΔG^0 :

$$\Delta G^0 = -z \times F \times E^0 \quad \text{eq. 7}$$

*ΔG*⁰ Standard Gibbs free energy or rather utilizable electric energy / J mol⁻¹
z Number of electrons exchanged
F Faraday constant / 96485 C mol⁻¹
*E*⁰ Standard potential / V

Therefore, eq. 7 describes the maximum utilizable electrical energy of a galvanic cell under standard conditions.

Since electrodes and electrolyte are in direct contact within the galvanic cell, an equilibrium proceeds at the phase boundaries. Therefore, the anions within the electrolyte interact with the positively charged electrode and vice versa. Consequential, an electrical double layer (EDL) develops at the electrode-electrolyte interface. The chemical potential μ_i differs at the phase boundary for the electrode and the electrolyte and is further influenced by the potential of the EDL ϕ_i . The electrochemical potential inside the cell μ_i^* is unique for its constituents i and is defined according to eq. 8.

$$\mu_i^* = \mu_i + z_i \times F \times \phi_i \quad \text{eq. 8}$$

μ_i^* Electrochemical potential inside the cell of component i / $J \text{ mol}^{-1}$
 μ_i Chemical potential of component i / $J \text{ mol}^{-1}$
 z Number of electrons exchanged
 F Faraday constant / 96485 C mol^{-1}
 ϕ_i Potential of the EDL / V

Whereby μ_i is constituted by

$$\mu_i = \mu_i^0 + R \times T \times \ln a_i \quad \text{eq. 9}$$

μ_i Chemical potential of component i / $J \text{ mol}^{-1}$
 μ_i^0 Chemical potential of component i at standard conditions / $J \text{ mol}^{-1}$
 R Universal gas constant / $8.3145 \text{ J K}^{-1} \text{ mol}^{-1}$
 T Temperature / K
 a Activity of species i

and directly linked to the Gibbs free energy via the stoichiometric factor ν_i by eq. 10.

$$\mu_i = \frac{\partial G}{\partial \nu_i} \quad \text{eq. 10}$$

μ_i Chemical potential of component i / $J \text{ mol}^{-1}$
 ΔG Gibbs free energy or rather utilizable electric energy / $J \text{ mol}^{-1}$
 ν_i Stoichiometric factor of component i

If equilibrium conditions exist within the galvanic cell, a difference between the potential of the electrode and the electrolyte, the so-called Galvanipotential $\Delta\phi$, develops. As already mentioned in chapter 2.1.1, the direct determination of the Galvanipotential of one phase is impossible. The rationale for this is simple: Every time a device is applied to determine the potential of e.g. the electrode, a new EDL accompanied by the generation of another Galvanipotential is created and hence only a potential difference is recorded.

The current i of a galvanic cell is composed of an anodic i_A and a cathodic i_C part. At equilibrium conditions of the cell, the current i_0 (A) or the current density j_0 ($A\ cm^{-2}$) of the anode and the cathode are equal.

$$j_0 = |j_C| = j_A \quad \text{eq. 11}$$

j_0 Current density / $A\ cm^{-2}$
 j_C Current density of the cathode / $A\ cm^{-2}$
 j_A Current density of the anode / $A\ cm^{-2}$

Under non-equilibrium conditions, when current flows, a shift of the potential compared to its theoretical value can be registered. The difference in theoretical and experimentally determined potentials for the galvanic cell is caused by the impact of an overpotential η .

$$E_{real} = \Delta E^0 - \sum |\eta| \quad \text{eq. 12}$$

E_{real} Experimentally determined potential / V
 ΔE^0 Difference in standard potential / V
 η Overpotential / V

The term „overpotential” implies different kinds of polarization (cf. Figure 4 (b)). The three main contributions to the overpotential are charge transfer polarization, concentration polarization and ohmic polarization. Since the reaction and crystallization overpotentials show a minor influence on the decrease of the cells potential they are not treated within this thesis.

- ◆ *Charge transfer polarization:* The reason for charge transfer or activation polarizations is the limited speed of the redox reactions at the phase boundary. It depends on the cell components and the kind of EDL.
- ◆ *Concentration polarization:* At high current densities, the mass transport of the reactants to the electrode/electrolyte interface diminishes. Concentration polarization originates since active species for the redox processes are not available anymore.
- ◆ *Ohmic polarization:* On load of the galvanic cell, a resistance of individual cell components emerges that is typical for the cell components used and is called IR drop. The IR drop is dependent on ionic, electronic and contact resistances of the cell.

Figure 4 (a) clearly shows the difference of the calculated, ideal curve compared to the experimentally determined curve 1 according to eq. 12. Curve 2 results either if the cell possesses a higher resistance or if a higher discharge rate is used. Therefore, polarization effects are only minor if

the cell is cycled with a very low current density and if the inner resistance of the cell is as low as possible.

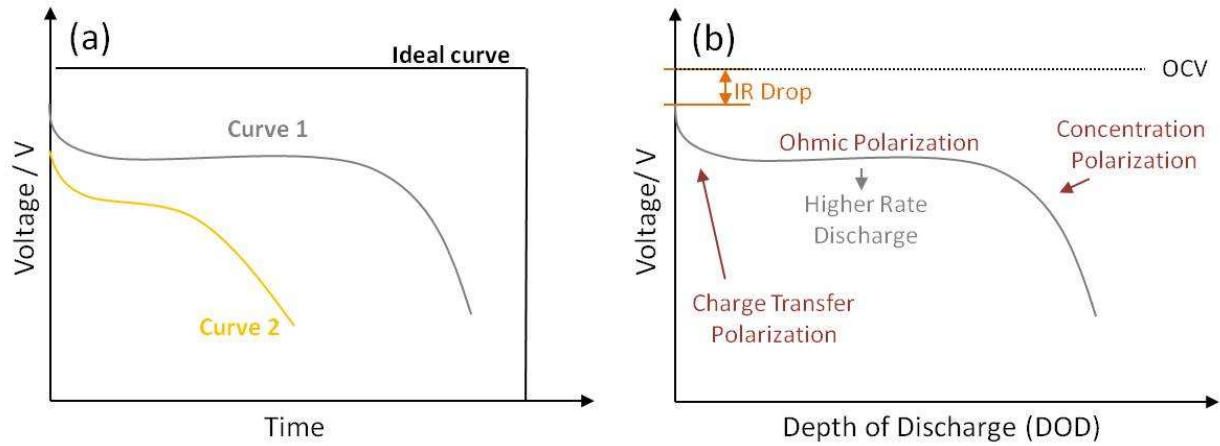


Figure 4: (a) Voltage against time plot. The ideal voltage curve and two real curves influenced by the overpotential are shown. Redrawn from [16]. (b) Characteristic discharge behavior of a battery showing the influences of η . Redrawn from [20] and [22].

To sum up, one could define eq. 12 more precisely:

$$E_{real} = \Delta E^0 - [(\eta_{ct})_a + (\eta_c)_a] - [(\eta_{ct})_c + (\eta_c)_c] - i \times R_i = i \times R \tag{eq. 13}$$

- E_{real} Experimentally determined potential / V
- ΔE^0 Difference in standard potential / V
- η_{ct} and η_c Charge transfer polarization and concentration polarization
- a and c Anodic and cathodic part
- i Operating current on cell load / A
- R_i and R Internal resistance and total resistance of the cell / Ω

During discharge of the cell, electrons are withdrawn from the anode moving into an external circuit. Faraday realized that there is a dependence of the electronic current i on the mass of substance m that is oxidized, referred to as Faraday's 1st law.

$$m = const. Q = const. i \times t \tag{eq. 14}$$

- m Mass of the substance / g
- Q Electric charge / As or C
- i Current / A
- t Time / s

According to eq. 14, the theoretical capacity ($As\ g^{-1}$) of a material can be calculated by eq. 15:

$$\frac{Q}{m} = \frac{z \times F}{M} \quad \text{eq. 15}$$

Q Electric charge / As or C
 m Mass of the substance / g
 z Number of electrons exchanged
 F Faraday constant / $96485\ C\ mol^{-1}$
 M Molar mass/ $g\ mol^{-1}$

The Faraday constant of eq. 15 is defined as the electric charge of one mole n of monovalent ions and is the product of the Avogadro constant N_A and the elementary charge e .

$$F = \frac{Q}{n} = N_A \times e \quad \text{eq. 16}$$

F Faraday constant / $96485\ C\ mol^{-1}$
 Q Electric charge / As or C
 n Mol / mol
 N_A Avogadro constant / $6.022 \times 10^{23}\ mol^{-1}$
 e Elementary charge / $1.602 \times 10^{-19}\ C$

Another important fact is that if the same amount of charge is involved during the redox-reactions at different electrodes, one mole of monovalent ions is discharged by one mole of electrons. If bivalent ions occur during the reaction, 2 moles of electrons are needed to discharge them. This fact is summarized by Faradays 2nd law:

$$\frac{m_A}{m_B} = \frac{M_A \times |z_B|}{M_B \times |z_A|} \quad \text{eq. 17}$$

$m_{A,B}$ Active mass of component A or B / g
 $M_{A,B}$ Molar mass of component A or B / $g\ mol^{-1}$
 $z_{A,B}$ Number of electrons exchanged for component A or B

2.1.3 Glossary

This subchapter gives an overview of the most important battery characteristics used within this thesis. The battery features are explained according to [16], [17] and [23].

- ◆ **OCV and nominal voltage:** The obtained voltage under no load conditions and the typical operating voltage of a cell are called OCV [V] and nominal voltage [V], respectively. They depend on temperature, concentration and transport limitations.

- ◆ *Capacity*: The theoretical capacity is based on Faradays law according to eq. 15 and is typical for the size and the chemistry of the cell. The amount of charge per unit weight is called specific capacity [Ah kg^{-1}]. The more charge carriers that are involved in the redox reactions and the lower the weight of the material, the higher the capacity.
- ◆ *Energy density*: This term implies the energy contained in a material or a device. It is the product of cell voltage and capacity. The energy density refers to unit volume [Wh L^{-1}], whereas the specific energy density states the energy per unit weight [Wh kg^{-1}].
- ◆ *Power density*: The power density is the product of current and operating voltage. It depends on the materials used and the cell design. The units are either [W L^{-1}] or [W kg^{-1}], for the power referred to unit volume and unit weight, respectively.
- ◆ *nC and C-rate*: nC defines the time for a complete charge or complete discharge of a battery or a cell, whereby n consists of 60 over n minutes. It is also a measure of the current. A C-rate of 1 signifies that the battery is charged or discharged within 1 hour (n=60 minutes). The unit of the C-rate is [A].
- ◆ *CC experiments*: The current within these experiments is kept constant regarding one charge/discharge cycle.
- ◆ *CCCV experiments*: After the CC charge, it is common to insert a trickle charge with constant voltage. Within this thesis, this trickle charge is performed for one hour at the highest voltage vs. Li/Li⁺ for each material.
- ◆ *Efficiency*: It means either the coulombic efficiency or the energy efficiency of a cell or battery. Whenever talking about efficiency within this thesis, coulombic efficiency is meant.

$$\eta_{\text{Coulombic}} = \frac{Q_{\text{Discharge}}}{Q_{\text{Charge}}} \times 100 \quad \text{eq. 18}$$

$\eta_{\text{Coulombic}}$ Coulombic efficiency / %

$Q_{\text{Discharge/charge}}$ Amount of charge that leaves/enters a battery or cell during cycling / Ah

- ◆ *Shelf and cycle life*: The shelf life of a battery or cell provides the deterioration of itself upon storage. The shelf life is influenced by the cell design, storage temperature, electrochemical system and the state-of-charge of the battery or cell. Therefore, ideal conditions should be chosen to minimize the self-discharge rate. Instead of the shelf life, the cycle life states the number of cycles of a battery or cell, usually until 80 % of its nominal capacity is achieved.
- ◆ *Electrolyte window*: The electrolyte window E_g signifies the voltage range within which the electrolyte is stable (no oxidation or reduction occurs). The borders of the electrolyte window are the lowest unoccupied molecular orbital (LUMO) and the highest occupied molecular orbital (HOMO) of the liquid electrolyte.

2.2 Lithium-ion battery

2.2.1 Brief historical development

The rapid market growth of portable electronic devices in the 1980s [24] forced the global battery market to the development of technologies with a lighter weight, a decrease in size and an increase of their capacity. The incorporation of metallic lithium in the battery seemed favorable due to the following reasons [25]:

- ◆ *Weight reduction*: Among all metals, lithium is the lightest one (6.94 g mol^{-1}).
- ◆ *Size reduction*: Metallic lithium possesses a low density of 0.53 g mL^{-1} .
- ◆ *Higher energy density*: Metallic lithium owns the most negative standard potential against NHE (cf. Table 2).

Primary lithium batteries were already applied in the 1960s and 1970s [26]. These primary cells consisted of lithium as negative electrode material and e.g. SO_2 or MnO_2 as positive electrode material. The invention of a secondary battery that contained metallic lithium as anode material was complex since it led to dendrite formation and capacity fading with progressive recharging. Around the 1980s, three fundamental points for the secondary LIB technology were published. Firstly, Peled showed that the development of an interface on the negative electrode material is crucial for the operation of alkali metals in non-aqueous electrolytes [27]. He demonstrated the necessity of controlling certain parameters to influence the SEI formation. Secondly, Mizushima et al. [28] reported about a new positive electrode material LiCoO_2 with an ordered rock salt structure and promising electrochemical characteristics. Thirdly, many researchers [29][30][31] focused on the substitution of metallic lithium by a second intercalation electrode³. The application of two intercalation electrodes that reversibly insert/deinsert lithium in its ionic form is termed „rocking-chair” technology [32]. Based on former inventions, utmost interest in the commercialization of secondary LIBs was attracted with the introduction of a safe cell chemistry, the graphite/ LiCoO_2 rocking-chair battery [7]. This rechargeable lithium-ion cell showed a two to three times higher gravimetric energy density compared to Ni-Cd batteries. Together with its potential above 3.6 V [33], a high energy density secondary lithium-ion battery was invented.

Since 1991, most research activities focus on the improvement of the LIB performance due to highly desirable implementation of the LIBs in stationary and automotive applications. This chapter gives an overview of some state-of-the-art components as well as next generation LIB components. Further, the formation of electrode/electrolyte interfaces and causes for capacity fading are described. At the end of the chapter, the functional principle of the LIB is summarized.

³ Intercalation electrodes reversibly take up/release lithium-ions without any conversion reaction of the material itself.

2.2.2 Active materials for LIBs

The positive and negative active materials are the part of the LIB, where the maximum achievable chemical energy, which is converted in electrical energy, is stored. In contrast to e.g. Ni-Cd batteries, many different LIB intercalation electrodes exist (cf. Figure 5). Therefore, the choice of the proper active materials depends on their target application. As already mentioned in chapter 2.1.2, the specific energy density is influenced by the average operating voltage of the LIB and the specific capacity of its contained active materials. To achieve a high value thereof, a sufficient amount of lithium-ions must be available within the cell and the voltage gap between the positive and the negative electrode should be as large as possible. Considering Figure 5 it is obvious, that the higher the capacity of the implemented negative electrode material the more material input of positive electrode is necessary. Since negative electrode materials have been thoroughly enough researched, ongoing R&D focuses on the development of new high voltage positive electrode materials.

The review article by Nitta and Yushin [34] summarizes electrode parameters for the right choice of active materials. To mention a few, delithiation capacities, capacity loadings (mAh cm^{-2}), rate performance, coulombic efficiency, affordability and safety of the materials need to be considered before application. Particular attention has also to be paid on the accurate particle size of the active materials and conductive coatings thereof. Hence, a decrease in lithium-ion diffusion lengths, an increase in electric conductivity and an improvement of electronic transport might be achieved by careful tuning of the particles [35].

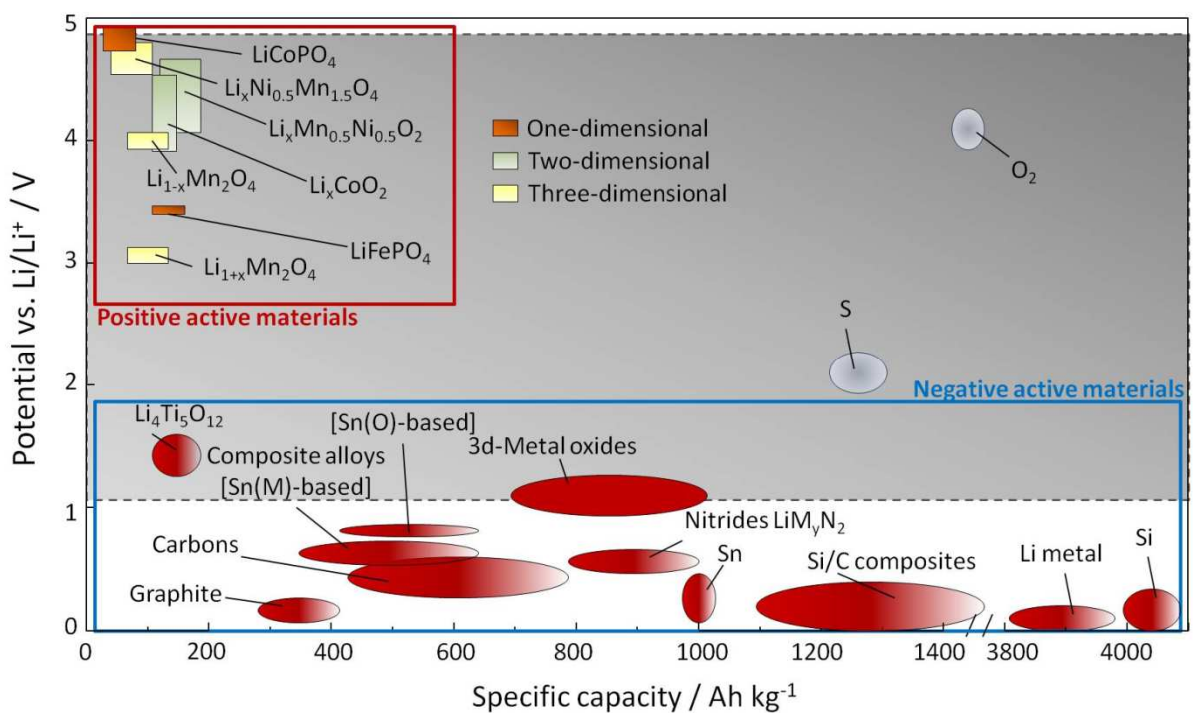


Figure 5: Potential versus capacity plot of common positive and negative electrode active materials based on [33], [36] and [37]. The grey area shows the electrochemical stability window of 1 M LiPF_6 in EC/DEC (1:1).

Within this chapter, a summary of well-known active materials is given. Firstly, several negative electrode materials are described and the recent progress concerning the development of others than carbonaceous materials is shown. Secondly, the main focus on positive electrode materials is on olivine-phosphates, since major work of this thesis is performed on the development of phospho-olivines. At the end of this section, also two-dimensional and three-dimensional positive electrode materials are presented, whereby recent developments in new positive electrode materials are mentioned.

2.2.2.1 Carbonaceous materials as negative electrode materials

Since 1991 [7], carbonaceous substances have become the common material for the anode in LIBs due to their superior safety, long-term cycling performance and high coulombic efficiencies compared to metallic lithium. Since then, a continual increase of these anodes in LIBs occurred, varying only in terms of the type of carbons used. Figure 6 illustrates the market development [38]. In 1995, most of the anodes were composed of mesophase graphite or hard carbon. Due to cost minimization, natural graphite appeared as material of first choice in 2010. Regardless its complex purification, the main drawback of instability against non-aqueous organic electrolytes is solved by modification techniques such as coating of the natural graphite with e.g. a carbon layer.

In general, there are two groups of carbonaceous materials used in LIBs, namely graphitic and non-graphitic carbons. Graphitic carbons exhibit a layered structure of graphene sheets and show some defects therein. Their voltage profile appears to be flat. Non-graphitic (disordered) carbons can be further subdivided into soft and hard carbons. Whereas in soft carbons the disorder of the graphene sheets can be removed by a reasonable temperature treatment, no graphitization of hard carbons occurs below 2850 °C. Another difference is the achievable capacity: Since soft carbons only insert less than one lithium per six carbon atoms ($x \sim 0.5-0.8$ in Li_xC_6), their capacity is low. By contrast, hard carbons reach high capacity values because more lithium can be stored ($x=1.2-5$ in Li_xC_6), whereas their precise location remains unclear. Zheng et al. [39] show that the capacity of hard carbons depends on the synthesis temperature. Hard carbons are synthesized at low temperatures (<1000 °C) and present a sloping voltage profile [40][41][42][43].

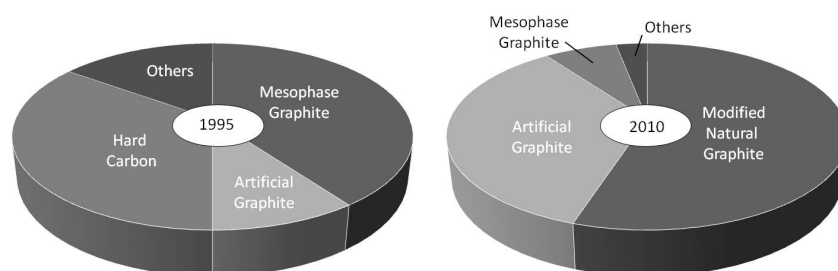


Figure 6: Major materials of the anode market. Redrawn from [38]. In 1995, 450 t of anodes were produced, whereas in 2010 the amount raised to 27.000 t.

The intercalation/deintercalation of lithium-ions and thus the caused voltage behavior and reversible capacity depend on the crystallinity and morphology of the graphitic and non-graphitic carbons [43][44]. Herein, the insertion/deinsertion mechanism of lithium-ions is described for graphitic carbons.

The stacking order of the graphene sheets is A-B and A-B-C for hexagonal and rhombohedral graphite, respectively [43]. Since the transformation energy between the two crystal systems is low, both stacking orders are always contained. To facilitate the explanation of the charging/discharging of graphite, only hexagonal graphite is treated. Hexagonal graphite belongs to the $P6_3/mmc$ space group and consists of graphene layers with sp^2 hybridized carbons [45]. Van der Waals forces weakly bond the graphene sheets. Lithium insertion happens according to eq. 25 during charging of the LIB. As illustrated in Figure 7 (i), this process only occurs at the prismatic surface or at the edge/defect sides of the basal plane surfaces [43][46]. Therefore, lithium intercalation behaviors are depending on the different ratios of prismatic to basal plane surfaces and on the particle sizes of the negative active material. Upon the insertion of lithium into the graphite lattice, the stacking order of the graphene sheets shifts from A-B-A to A-A-A. Structural defects may prevent this sliding and thus full lithiation is inhibited. Further, the distance between two graphene layers is increased from 0.3354 nm to 0.370 nm, meaning a volume expansion of 10.3 % [43].

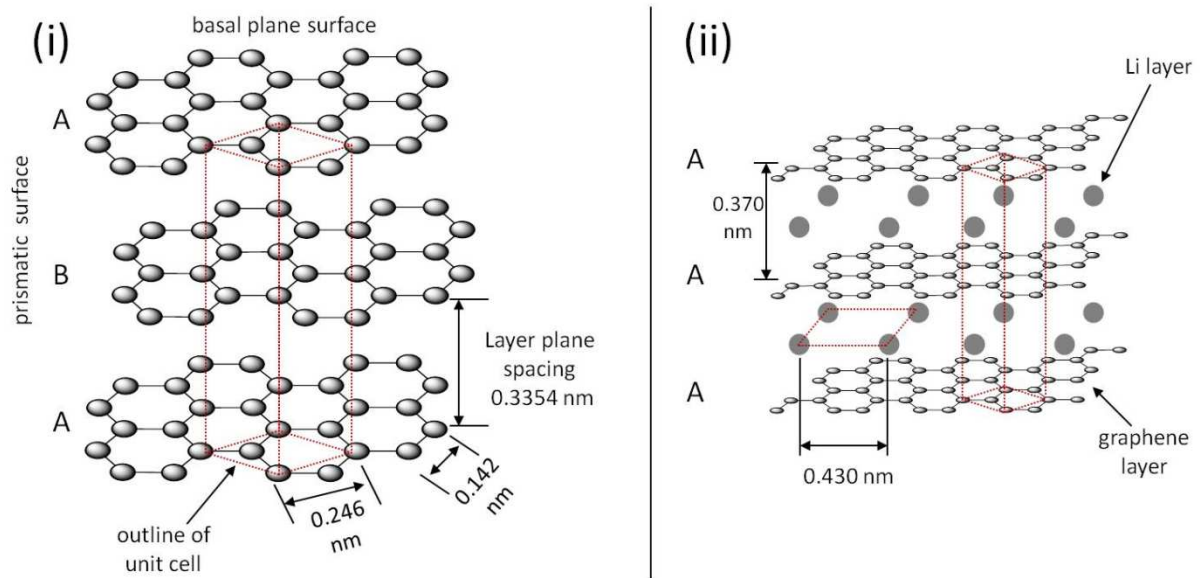


Figure 7: Crystal structure of hexagonal graphite (i) and of graphite with fully intercalated lithium-ions (ii), showing a stacking order of the graphene layers of A-B-A and A-A-A, respectively. Redrawn and modified from [43].

Figure 8 shows that the intercalation of lithium into graphite occurs stepwise at different voltage stages [43][47]. Stage II is divided into II and II L, because lithium inserts diversely, leading to different lithium packing densities in the graphite. A clear distinction between the stages is not possible and therefore some stages coexist at certain voltage regions. Song et al. [48] show by XRD and high resolution transmission electron microscopy measurements that LiC_6 and LiC_{12} coexist in the

lithiated graphite particle. The lithiation state of the graphite is closely related to a color change. Harris et al. [45] publish that LiC_{18} , LiC_{12} and LiC_6 present a dark blue, red and golden color, respectively. They demonstrate that the lithiation starts at the active materials contact to the current collector and progresses towards the surface of the electrode. Complete lithiation of the graphite (LiC_6) results in a theoretical capacity of 372 mAh g^{-1} . Since graphite operates outside the electrochemical stability window of the electrolyte the irreversible capacity loss of the first charge/discharge cycle prevents the achievement of the theoretical value. Therefore, a practical capacity of 80-95 % [43] of its theoretical value can be reached during the first charge/discharge cycle and a protective layer, the SEI, forms on its surface.

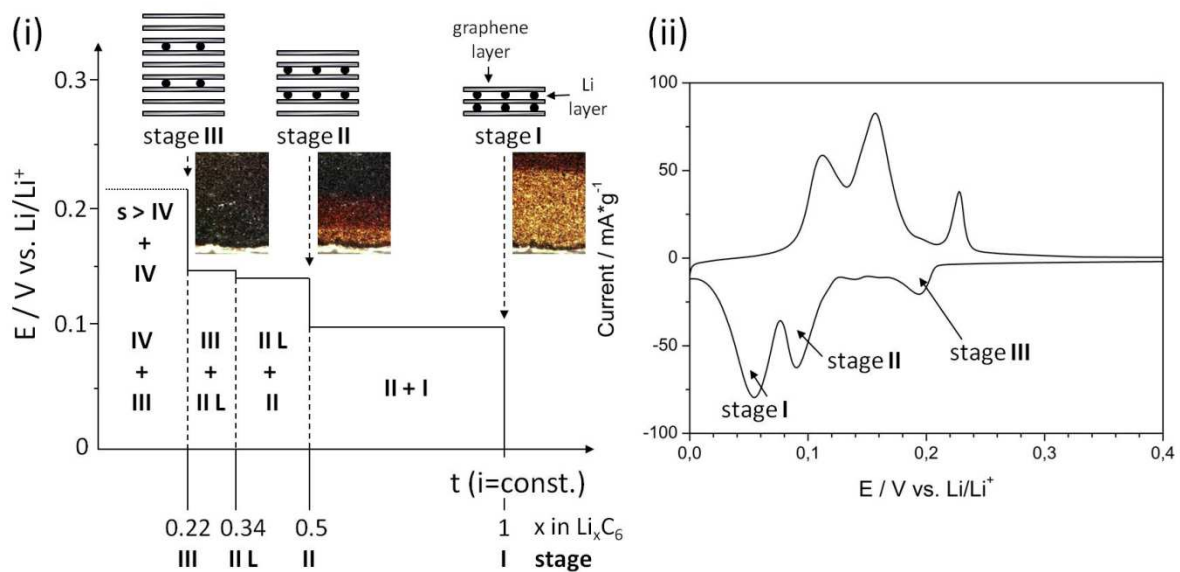
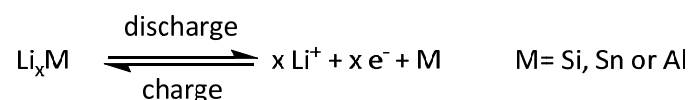


Figure 8: (i) Galvanostatic curve illustrating the stage formation in graphite upon lithium intercalation. Redrawn from [43] and modified by adding optical micrographs taken by in-situ measurements from S. J. Harris et al. [45] upon charging of the graphite. (ii) Corresponding cyclic voltammometric measurement.

Ongoing research on carbonaceous materials focuses on the improvement of the rate capability of graphite [44]. To achieve higher capacities, the application of hard carbons as well as special arrangements of graphene in graphene-based active materials seems attractive [39][49]. Although the specific capacity of graphitic carbons is low compared to lithium alloys, hard carbons and graphene (cf. Figure 5) their substitution as negative electrode material remains challenging due to their excellent cycling behavior and long cycle life.

2.2.2.2 Other feasible negative electrode materials

Lithium alloys. In 1971, Dey [50] realizes that lithium alloys with other metals in 1 M LiClO_4 in propylene carbonate according to eq. 19. This alloying occurs if the other metal is adequately polarized by the electrolyte [43]. Some metals that form alloys with lithium are Si, Sn and Al.

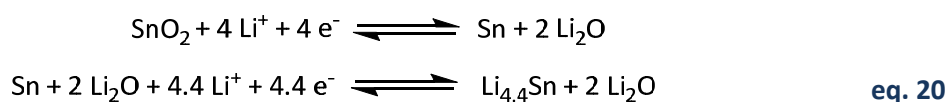


Considering the potential vs. capacity plot (cf. Figure 5), the main advantage of lithium alloys is their superior theoretical capacity compared to carbonaceous materials. Anyway, huge volume changes (cf. Table 3) of these materials have impeded their application as negative electrode material so far. Many research activities focus on the improvement of increasing the coulombic efficiency of the 1st charge/discharge cycle and cycle life. Some strategies are: Downsizing of the particles, formation of intermetallics, application of the materials as thin film, controlling of the operating voltage and embedment of the lithium alloys in matrix materials [43][51][52][53]. The latter strategy seems really promising since Obrovac et al. [54] show that the volumetric energy density of lithium alloys is either increased by an increased degree of lithiation or if the volume expansion is fixed, the active material can be diluted with an inactive phase.

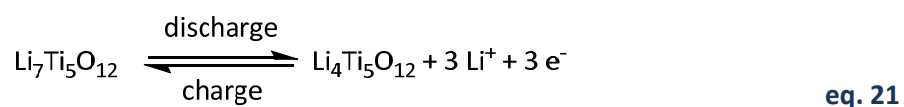
Table 3: Comparison of the volume change upon lithium uptake of graphite, metal alloys, metal oxides and spinel-type anode materials. Values taken from [51], [55] and [56].

Lithiated species	Volume increase / %	Lithiated species	Volume increase / %
LiC ₆	10	Li _{4,4} Sn (from Sn)	676
LiAl	96	Li _{4,4} Sn (from SnO ₂)	200
Li ₄ Si	320	Li ₇ Ti ₅ O ₁₂	1

Transition metal oxides. They are another interesting group for high capacity negative electrode materials. As opposed to lithium alloys and intercalation electrodes, a conversion reaction occurs in most metal oxides. Li₂O serves as electrochemically inactive buffer matrix that significantly improves cycling stability [52][57]. Generally, the conversion reaction can be illustrated according to eq. 20.



Spinel-type negative electrode materials. Recently, Li₄Ti₅O₁₂ (LTO) has gained a lot of interest for application in EVs due to safety reasons since the Ti⁴⁺/Ti³⁺ redox reaction occurs at 1.5 V vs. Li/Li⁺ [58]. Upon charging from 2.5 to 1 V vs. Li/Li⁺, LTO takes up three lithium-ions (cf. eq. 21) and undergoes a structural change from the spinel to the rock salt type.



The discharging down to 0.01 V vs. Li/Li⁺ can even increase the lithium uptake to a number of five lithium-ions and thereby enhance its specific capacity. The negligible volume change upon lithium insertion is favorable in terms of long-term cycling performance. Particle tuning by e.g. doping or carbon surface modification leads to materials that sustain high C-rates and therefore, fast rechargeable battery systems [59][60].

2.2.2.3 One-dimensional positive electrode materials

Phospho-olivines. LiMPO_4 ($M = \text{Fe}, \text{Mn}, \text{Co}, \text{Ni}$) are first discovered as positive electrode materials by Padhi et al. in 1997 [61]. Within their work, they show that LiFePO_4 can reversibly take up ~ 0.6 Li per formula unit at a redox potential of ~ 3.5 V vs. Li/Li^+ . Ever since, phospho-olivines have aroused interest due to their affordability, eco-friendliness and safety reasons. The latter is caused by their stable crystal lattice (cf. Figure 9 (i)). The crystal lattice consists of a polyanion framework that is composed of PO_4 -tetrahedra which corner- and edge share MO_6 octahedra in a three-dimensional way. The LiO_6 octahedra are edge-shared parallel to the b-axis [61][62]. Among the three possible lithium pathways, the movement of the lithium-ions at ambient temperature occurs along the energetically favored [010] channels of the crystal along the b-axis [63][64]. Since their motion proceeds in a one-dimensional way, these materials are very sensitive to any defects or impurities within the crystal structure.

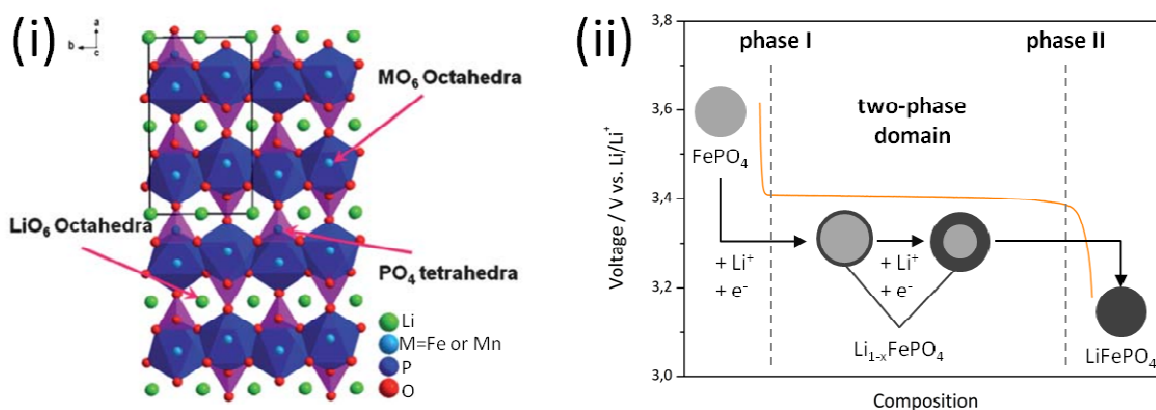


Figure 9: (i) Crystal structure of phospho-olivines LiMPO_4 ($M = \text{Fe}, \text{Mn}$) [65] and (ii) scheme of the two-phase mechanism of lithium insertion into FePO_4 represented via shrinking core model. Redrawn and modified from [63] and [66].

Figure 9 (ii) shows that the insertion/deinsertion of lithium-ions into the phospho-olivine structure occurs following a two-phase mechanism. According to the shrinking core model, a lithium-rich and lithium-poor phase develops among the insertion/deinsertion of lithium-ions into the lattice. The lithium-rich shell covers the lithium-poor core and expands as the lithiation of FePO_4 proceeds [63] [66]. More recent studies on the charge/discharge mechanism of LiFePO_4 by XRD and HR-TEM reveal that nanoparticles are either composed of pure lithium-rich or pure lithium-poor phases. Since the shrinking core model cannot give a description for these new observations, Delmas et al. [67] investigate the domino-cascade model. Therefore, they show that due to the low ionic and electronic conductivity of LiFePO_4 , lithium-ion deinsertion more likely occurs close to the initial nucleation site (cf. Figure 10). Whether or not the insertion/deinsertion of lithium-ions in phospho-olivines proceeds according to the core-shell or domino-cascade model is still under debate.

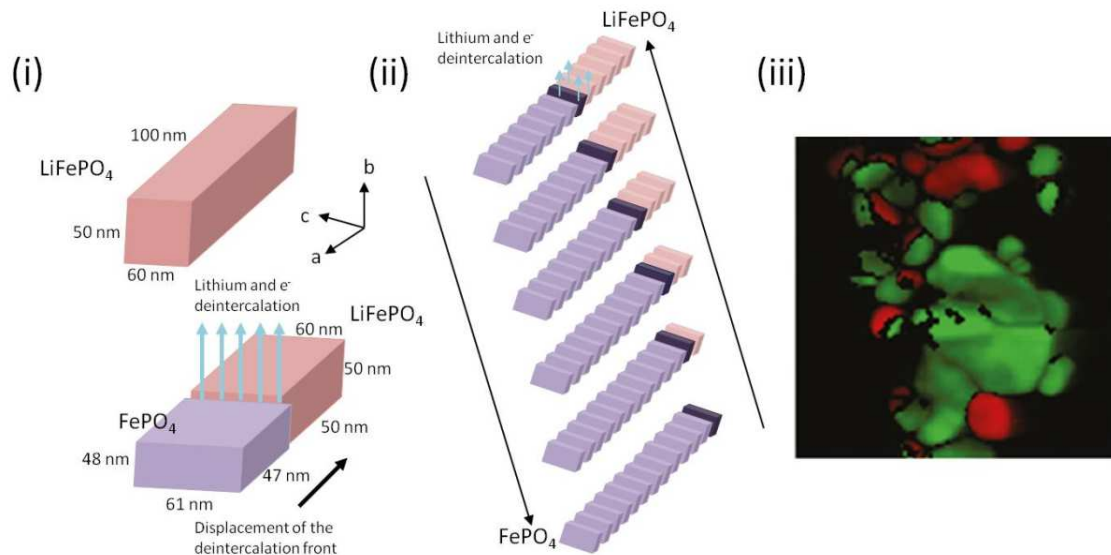


Figure 10: Scheme of the domino-cascade model with (i) showing the strains occurring during the charging of a battery in LFP and (ii) the charging and discharging of LFP. Redrawn from [67]. (iii) Precision electron diffraction (PED) phase map recorded by Brunetti et al. [68] of either fully lithiated (red) or fully delithiated (green) LFP particles.

The major drawbacks of phospho-olivine positive electrode materials are their low ionic and electronic conductivity. These drawbacks have been overcome for LiFePO_4 by the synthesis of a nanocomposite material covered with a conductive carbon layer. At a C-rate of 0.5, 93 % of its theoretical capacity (170 mAh g^{-1}) can be achieved [62]. Nevertheless, the carbon content within the material needs to be carefully adjusted since increasing the carbon content occurs at the expense of the gravimetric energy density and the tap density of the material [69]. Delacourt et al. [70] demonstrate that a precise control of the size of LiFePO_4 should be performed in favor of the energy density of the material.

Moreover, cationic or anionic doping of LiFePO_4 with certain elements remarkably improves its electronic conductivity from $10^{-9-10} \text{ S cm}^{-1}$ [66] to $10^{-1-3} \text{ S cm}^{-1}$ [65] since it might reduce the anti-site defects of the crystal lattice. Whereas calculations [71] show that doping is only favorable for isovalent ions, both isovalent and aliovalent doping are found to improve the transformation kinetics and expand the lithium-ion diffusion channels [72]. The doping of LiFePO_4 with 1 mol % Zn [73] reduces the shrinking upon lithium extraction and therefore improves its kinetics. Ou et al. [74] show that M1 site doping with magnesium does not lead to a remarkable improvement of specific capacity values. On the contrary, Huang et al. [75] exhibit that M2 site doping with Mg^{2+} increases the ionic and electronic conductivity. They also show that co-doped $\text{LiFe}_{0.92}\text{Mg}_{0.08}(\text{PO}_4)_{0.99}\text{F}_{0.03}/\text{C}$ demonstrates the best electrochemical performance since the anion doping further enhances the rate performance of the material.

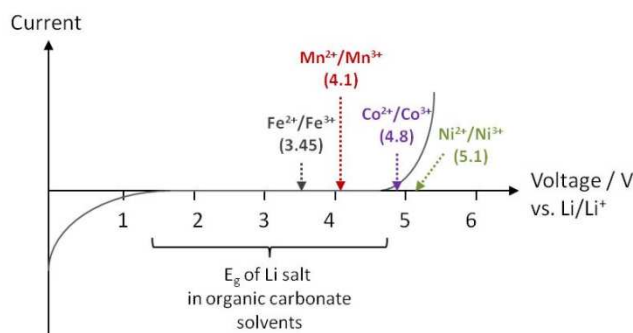


Figure 11: Electrochemical stability window of common lithium salts in organic solvents and corresponding redox potentials of phospho-olivines. Redrawn and modified from [76].

Beside comparable theoretical capacity values of phospho-olivines LiMPO_4 ($M = \text{Fe, Mn, Co, Ni}$), their redox potential increases as follows: $\text{Fe} < \text{Mn} < \text{Co} < \text{Ni}$. Theoretically, the gravimetric energy density could be raised from 578 Wh kg^{-1} for LiFePO_4 to 802 Wh kg^{-1} for LiCoPO_4 [77]. Anyway, the application of LiCoPO_4 and LiNiPO_4 is restricted not only by the lack of a suitable electrolyte but also due to even worse electronic conductivity compared to LiFePO_4 . Figure 11 illustrates that the redox reaction for $\text{Co}^{2+}/\text{Co}^{3+}$ of LiCoPO_4 occurs at the extreme limit of the electrolyte stability. Ni is oxidized and reduced at a potential beyond the electrochemical stability window of common electrolyte systems. Therefore, they are unattended within this thesis.

The reasons for inferior electrochemical behavior of LiMnPO_4 compared to LiFePO_4 are shown by Delacourt et al. [78]. Section 2.1.2 already mentions the overpotential, which is integral for the experimentally determined voltage behavior of the LIB. Within their research about LiMPO_4 ($M = \text{Fe}$ or Mn) they show that the charge transfer polarization at low current densities is negligible. Further, their CC experiments lead to the conclusion that the transport properties of the ions as well as electrons are decisive for the poor electrochemical performance of LiMnPO_4 . Nevertheless, careful tuning of the particle size and morphology of LiMnPO_4 leads to an acceptable electrochemical performance. A specific discharge capacity of 119 mAh g^{-1} at 0.1 C for LiMnPO_4 is achieved by Guo and coworkers [79] by applying a precipitation synthesis method. Further, Pan et al. [80] synthesize LiMnPO_4 via a hydrothermal route with an even higher specific discharge capacity of 147.6 mAh g^{-1} at 0.1 C and elevated temperature.

The formation of solid solutions of different metal ions turned out to be favorable with regard to electrochemical performance and a mutual influence of the redox couple positions occurs. Therefore, solid solutions of phospho-olivine positive electrode materials seem very promising for next generation cathode materials. Muraliganth and Manthiram [81] attribute the shift in redox potentials to the insertion of counter cations into the crystal structure. In theory, the position of the oxidation and reduction reaction depends both on the electronegativity and the ionic radii of the cations. The two phenomena have a converse effect on the peak positions and usually one of them is

predominant. For $\text{LiFe}_x\text{Mn}_{1-x}\text{PO}_4$ solid solutions, the influence of the ionic radii of iron and manganese predominates since their electronegativity is quite similar. As a matter of fact, a higher iron content in $\text{LiFe}_x\text{Mn}_{1-x}\text{PO}_4/\text{C}$ increases the covalence of the Mn-O bonds and decreases the redox potential of $\text{Mn}^{2+}/\text{Mn}^{3+}$. The decrease in the Mn-O-Mn band gap leads to better electrochemical performance [82]. However, if Fe or Mn is substituted by the more electronegative Co^{2+} , the covalence of the Fe-O and Mn-O bond length decreases due to the inductive effect. Therefore, the redox potentials for $\text{Fe}^{2+}/\text{Fe}^{3+}$ and $\text{Mn}^{2+}/\text{Mn}^{3+}$ are increased, whereas the voltage of the redox reaction $\text{Co}^{2+}/\text{Co}^{3+}$ is decreased.

The ideal values for the solid solution $\text{LiFe}_x\text{Mn}_{1-x}\text{PO}_4$ are noted in the review by Zaghbi et al. [63] as $0.5 \leq x \leq 0.8$. Anyway, new synthesis methods show that a decrease of x to 0.2 leads to a good electrochemical performance accompanied by an increase in energy density [83][84][85]. Even solid solutions with an iron content as low as 0.1 for x [86] show an improved electrochemical behavior compared to bare LiMnPO_4 . Another interesting aspect is examined by Paoletta et al. [87]. In contrast to many other research studies, they find that platelet-shaped nanocrystals of $\text{LiFe}_{0.5}\text{Mn}_{0.5}\text{PO}_4$ without any post-thermal treatment after their synthesis show only one oxidation and reduction peak upon cyclic voltammetric measurements. They attribute this single phase transition to the uniform distribution of the cations within the crystal lattice.

In addition, further research activities focus on the development of solid solutions with cobalt. The formation of e.g. $\text{LiFe}_x\text{Co}_{1-x}\text{PO}_4$ seems beneficial, since the redox potential of Co will appropriate to the electrochemical stability window of the electrolyte by increasing the iron content. The incorporation of Fe and Co in the crystal lattice improves the electrochemical characteristics compared to bare LiCoPO_4 . Anyway, the experimentally determined gravimetric energy density is still worse than LiFePO_4 [77][88]. Recently, a very good discharge capacity of 160 mAh g^{-1} at 0.1 C is achieved for carbon coated $\text{LiFe}_{1/3}\text{Mn}_{1/3}\text{Co}_{1/3}\text{PO}_4$ [89]. The insertion of three different metals into the phospho-olivine is beneficial in terms of less capacity fading due to electrolyte instability and superior electrochemical performance compared to LiCoPO_4 .

2.2.2.4 Two- and three-dimensional positive electrode materials

Lithium transition metal oxides. This class LiMO_2 ($M = \text{Co}, \text{Ni}, \text{Mn}$) is a representative of two-dimensional positive electrode materials. Figure 12 demonstrates the crystal structure and corresponding cyclic voltammogram of the most widespread cathode material, LiCoO_2 . The layered structure of LiCoO_2 is composed of CoO_2 and Li layers, which are arranged in alternating [111] octahedral site planes of the crystal [90][91][92]. The structure of LiMO_2 is superior to that of phospho-olivines, since it allows lithium-ions to move in a two-dimensional way and therefore structural defects or impurities are not as detrimental as in one-dimensional positive electrode

materials. Because of severe structural changes [90] of $\text{Li}_{1-x}\text{CoO}_2$ ($x \geq 0.5$) upon charging, only approximately half of its theoretical capacity is attainable.

To overcome the drawbacks of high toxicity and high costs of cobalt, attempts are performed to fully or partly replace it by Ni or Mn. Therefore, many research activities focus on the development of $\text{LiNi}_{0.5}\text{Mn}_{0.5}\text{O}_2$ and $\text{LiNi}_{1/3}\text{Mn}_{1/3}\text{Co}_{1/3}\text{O}_2$ (NMC) [92]. Their meta-stability makes lithium transition metal oxides prone to oxygen loss and electrolyte oxidation followed by a subsequent decay in electrochemical performance. Both disadvantages might be reduced by surface coatings and doping, respectively [64] [91].

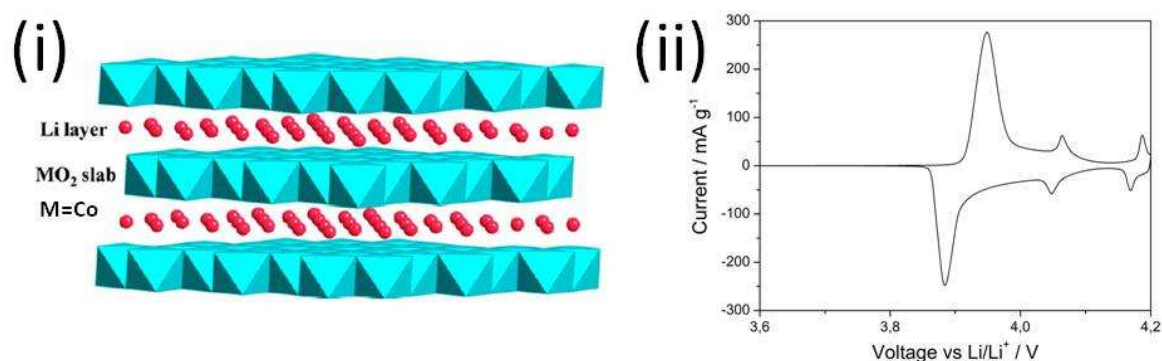


Figure 12: (i) Crystal structure of layered LiCoO_2 [92] and (ii) its corresponding CV provided by Christian Baumann.

Spinel-type compounds. By comparing Figure 12 with Figure 13, it is obvious that two-dimensional lithium transition metal oxides and three-dimensional spinel-type compounds LiM_2O_4 are composed of the same oxygen framework building block [92]. Three quarters of their octahedral sites are occupied by the transition metal M, whereas the lithium-ions occupy the tetrahedral sites. The remaining vacant quarter in the transition metal oxide layer results in a three-dimensional diffusion pathway for lithium-ions. Generally, the spinel framework $[\text{M}_2]\text{O}_4$ is able to insert 4 lithium-ions between a voltage range of 1-4.3 V vs. Li/Li^+ [90], but only the two upper voltage plateaus are of interest. The resulting voltage plateaus depend on the stoichiometry of the spinel and therefore on the position of the lithium-ions in the crystal. As illustrated in Figure 13, the 4 V plateau results from a manganese spinel $\text{Li}_x[\text{Mn}_2]\text{O}_4$ with $0 \leq x \leq 1$ and the lithium-ions are positioned on the tetrahedral 8a sites, respectively [91]. Since the cycling performance at ~ 4 V is superior to that of 3 V due to less severe manganese distortion by the Jahn Teller effect, only the 4 V plateau is used in practice [93]. Hence, the maximum theoretical capacity achievable for LiMn_2O_4 (LMO) is 148 mAh g^{-1} . Anyway, the high rate performance and thermal stability of spinel-type materials is to the best advantage. Therefore, strategies are developed to cope with the Mn dissolution and improve their cycle life. Among these approaches, synthesizing spinels with a higher lithium than manganese content, synthesizing cation deficient materials, doping them with multivalent ions, applying atomic surface layers or blending among themselves seem promising [64][91][94][95][96][97].

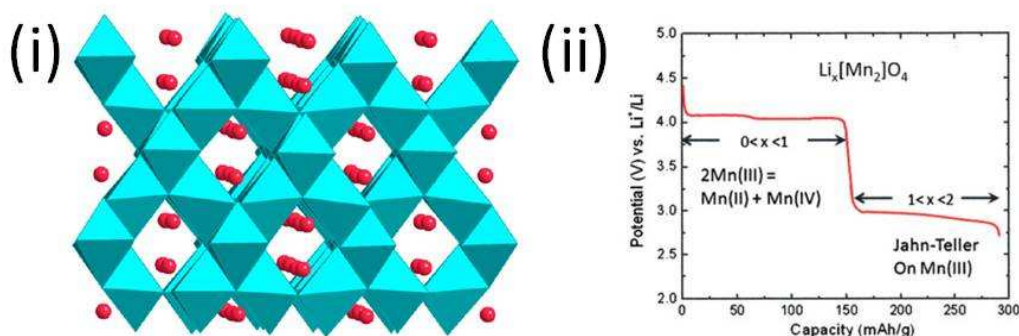


Figure 13: (i) Crystal structure of spinel-type LMO (three-dimensional host material) [92] and (ii) voltage vs. capacity plot of $\text{Li}_x\text{Mn}_2\text{O}_4$ ($0 < x < 2$) [98].

2.2.2.5 Prospective materials for the positive electrode

Regarding positive electrode materials, many research activities focus on polyanionic compounds since they usually exhibit a higher voltage plateau of the redox active metal due to the inductive effect [99]. Therefore, a higher energy density of the material is achievable. These include, inter alia, fluorophosphates $\text{Li}_x\text{MPO}_4\text{F}$ with $0 \leq x \leq 2$ ($M = \text{V}, \text{Fe}$) [92][100], silicates Li_2MSiO_4 ($M = \text{Fe}, \text{Mn}$) [64][92], sulfates LiMSO_4F ($M = \text{Fe}, \text{Mn}$ or mixtures thereof) [99][101] and borates LiMBO_3 ($M = \text{Fe}$) [92]. Among them, the highest $\text{Fe}^{2+}/\text{Fe}^{3+}$ redox potential with 3.9 V vs. Li/Li^+ is found for $\text{LiFe}_{1.6}\text{Mn}_6\text{SO}_4\text{F}$ [101]. Therefore, the formation of solid solutions in consideration of the inductive effect and its impact on redox potential might be useful to achieve a higher energy density.

Regarding Table 4, especially silicates and borates seem very promising as new positive electrode materials due to high theoretical capacity and high theoretical achievable energy density. But up to now, the practical deinsertion of lithium from $\text{Li}_2\text{FeSiO}_4$ is restricted to one lithium-ion per formula unit. Also, materials with the lightest polyanionic borate group need further development to increase their electrochemical performance.

Table 4: Theoretical capacities of prospective cathode materials calculated by using eq. 15.

Material	Theor. cap. / mAh g ⁻¹	Material	Theor. cap. / mAh g ⁻¹
$\text{Li}_2\text{FePO}_4\text{F}$	146 (1 Li ⁺ extracted)	$\text{Li}_2\text{FeSiO}_4$	331 (2 Li ⁺ extracted)
	292 (2 Li ⁺ extracted)	LiFeSO_4F	151
$\text{Li}_2\text{FeSiO}_4$	166 (1 Li ⁺ extracted)	LiFeBO_3	220

Another strategy to increase the energy or power density of positive electrode materials is blending among them. Cathode blends generally diminish the drawbacks of their constituents. Anyway, special care must be taken by using blends, since this procedure might strengthen the weaknesses of their components as well. LiMn_2O_4 (LMO) bears many advantages as promising cathode material like high abundance of manganese, low cost and toxicity as well as high thermal stability. Its main drawback of manganese dissolution can be suppressed by blending and therefore the cycle life of the LIB

improves. Among them, mixing of LMO with either $\text{LiNi}_{1/3}\text{Mn}_{1/3}\text{Co}_{1/3}\text{O}_2$ (NMC) or $\text{LiNi}_{0.8}\text{Co}_{0.15}\text{Al}_{0.05}\text{O}_2$ (NCA) is advantageous [102][103]. Whereas the mixture of LMO and NMC improves the capacity retention of the LIB, the blend of LMO and NCA exhibits higher discharge capacities compared to bare LMO. Nevertheless, the irreversible specific charge during the first charge/discharge cycle is enhanced by blending with NCA.

Another class that has gained a lot of interest is $x\text{Li}_2\text{MnO}_3-(1-x)\text{LiMO}_2$ (M=Mn, Ni, Co) thanks to its unique electrochemical characteristics and high initial capacity of $250\text{-}280\text{ mAh g}^{-1}$. Its major drawback of high irreversible capacity values in the initial charge/discharge cycle can be improved by applying coatings such as LiNiPO_4 [104]. Therefore, this blend seems promising for automotive applications.

2.2.3 Electrolytes for LIBs

The replacement of metallic lithium by graphitic materials as anode does not only lead to losses in the voltage range of the LIB, but also to severe problems if cycling occurs with electrolytes based on propylene carbonate (PC). This is because PC co-intercalates with the Li-ions into the graphite and subsequently graphite exfoliation takes place [105]. A detailed study on binary electrolyte mixtures in 1994 [106] reveals that a solution of LiPF_6 in EC:DMC shows superior cycling behavior of the 4 V LIB since electrolyte oxidation (broad electrochemical stability window E_g) and graphite exfoliation is inhibited.

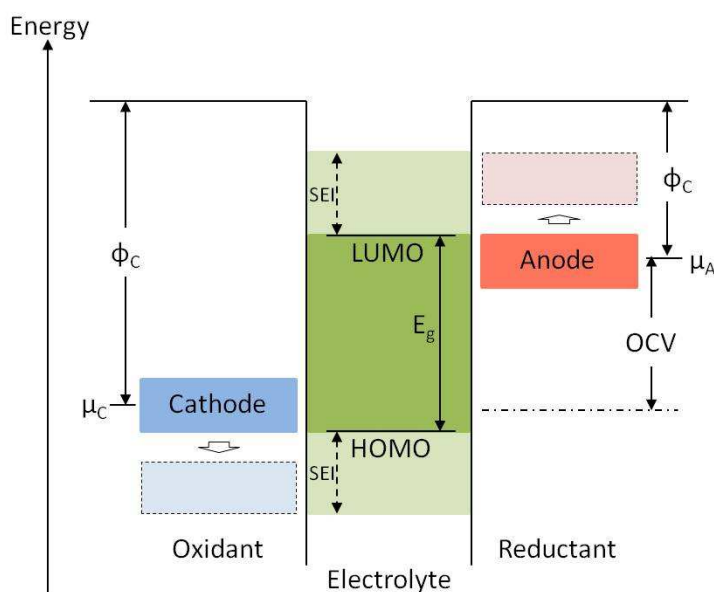


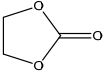
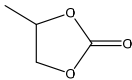
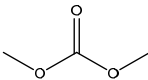
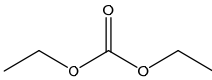
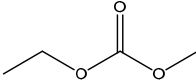
Figure 14: Open-circuit energy diagram of a battery. The scheme is redrawn from [36] with Φ as the work function and μ as the electrochemical potential of the cathode and the anode. E_g represents the electrochemical stability window of the electrolyte.

As illustrated in Figure 14, the E_g of an electrolyte comprises the region wherein it is stable against the reduction and oxidation of the anode and the cathode, respectively. Therefore, the choice of the proper electrolyte system seems inevitable. A critical contemplation of published electrochemical stability windows is necessary because most E_g s of electrolytes are determined by using ideal, nonporous electrodes such as Pt or glassy carbon [107]. Most applied electrodes feature a porous structure and hence, the behavior of oxidation and reduction of the electrolyte may differ leading to a decrease in its E_g .

Generally, the most widespread liquid electrolytes in today's LIBs are based on LiPF_6 in a mixture of two or more carbonate solvents. 1 M LiPF_6 in a binary mixture of EC:DMC is favorable owing to its high conductivity, sufficient passivation of the current collector, efficient SEI forming ability and high stability against reduction by the anode [76]. Considering high voltage applications of LIBs, results from recent research have shown that this binary mixture is even stable up to 5.3 V vs. Li/Li^+ against

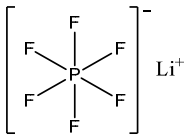
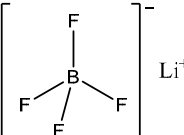
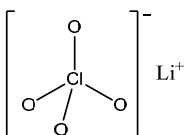
Li/LiNi_{0.45}Cr_{0.05}Mn_{1.5}O₄. Therefore, the E_g of the electrolytes generally greatly depend on the kind of cathode material used [108].

Table 5: Physical properties of common organic carbonates used as electrolyte solvents taken from the review article of non-aqueous liquid electrolytes at 25 °C [109]. Deviations in temperature are shown in brackets.

Solvent	Structure	$\epsilon / \text{F m}^{-1}$ (25 °C)	η / cP (25 °C)
EC		89.78	1.90 (40 °C)
PC		64.92	2.53
DMC		3.107	0.59 (25 °C)
DEC		2.805	0.75
EMC		2.958	0.65

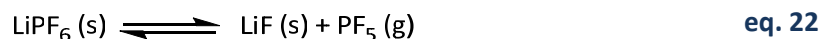
The two most important characteristics for the right choice of solvents with regard to the conductive salt are their dielectric constant ϵ and viscosity η . Considering Table 5, the application of at least binary mixtures of carbonates is absolutely necessary. Whereas e.g. EC ensures sufficient dissolution of the conductive salt and SEI formation, a linear carbonate such as DMC is required to lower the viscosity and thereby simplifies the transportation of lithium-ions [109].

Table 6: Conductive salts (state-of-the-art and recently investigated) for LIBs and their advantages/disadvantages in comparison to LiPF₆ [105][109][110][111][112].

Salt	Structure	Advantages	Disadvantages
LiPF ₆		High ionic conductivity Good dissociation in carbonates Al current collector passivation Stable SEI formation	Sensitive to moisture and elevated temperature
LiBF ₄		Low toxicity High safety	Lower ionic conductivity
LiClO ₄		High ionic conductivity High anodic stability	Stronger oxidative behavior

Salt	Structure	Advantages	Disadvantages
LiFSI		High ionic conductivity Lower F content	Al current collector corrosion Higher heat generation among decomposition
LiDMSI		Superior thermal stability	Inferior electrochemical stability
LiFOP		Higher thermal stability Higher hydrolysis stability	Instability of SEI
LiBOB		Improved high temperature performance Al current collector passivation Applicable with PC	Worse low temperature performance

Table 6 summarizes the advantages/disadvantages of some state-of-the-art and recently studied conductive salts. Regarding their solubility and average ion mobility in organic carbonate solvents, LiPF₆ exhibits the best compromise between them [109]. The two main drawbacks of LiPF₆ are its hydrolysis sensitivity of the P-F bonds as well as the reactivity of the lewis acid PF₅ with protic impurities and ether linkages of the organic carbonates.



At elevated temperature the endothermic equilibrium (eq. 22) is strongly favoring the formation of gaseous PF₅ and therefore, thermal degradation of the electrolyte is remarkably enhanced [113]. Even if these drawbacks can be avoided by the application of other salts, currently no other salt outperforms LiPF₆. Nevertheless, large scale applications of LIBs based on aprotic solvents and LiPF₆ might result in severe safety problems due to thermal runaway risks. To increase their safety, a replacement of liquid electrolytes by either solid ones or ionic liquids might be advantageous. Figure 15 illustrates the conductivities of different electrolyte classes. Whereas liquid electrolytes have a conductivity of approximately 10⁻² S cm⁻¹ at room temperature, most solid electrolytes can only compete with them at elevated temperatures up to 80 °C [114][115]. Other drawbacks of solid electrolytes might be their inferior chemical stability as well as high cost. Anyway, great promise for application is offered by the ceramic Li₁₀GeP₂S₁₂ and polymer PVDF/hexafluoropropylene/lithium salt since they exhibit similar conductivities as liquid electrolytes [114][116]. Owing to their non-volatility and non-flammability, ionic liquids gain attention as another novel class of electrolytes. But their usually high viscosity and thus, low ionic conductivity inhibit a replacement of liquid organic

electrolytes [116][117]. Therefore, the thermal behavior and surface film formation ability on electrodes are only described for aprotic, liquid electrolytes.

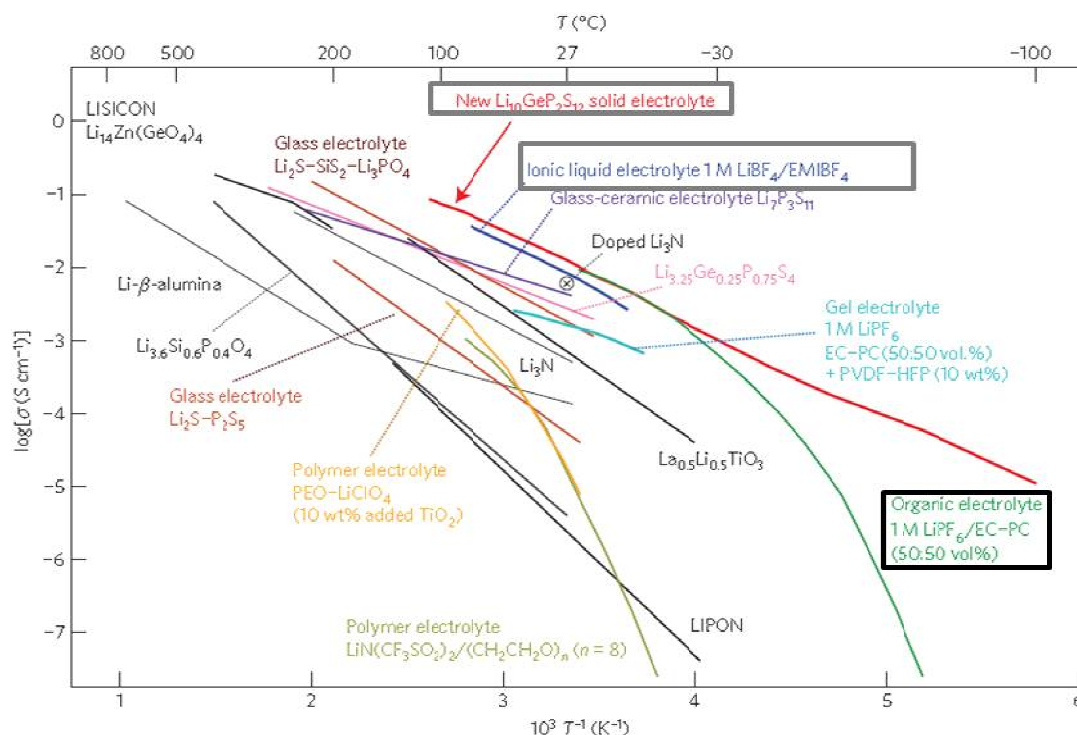


Figure 15: Comparison of the conductivities σ of different electrolytes (solid, glass, polymer, organic, ionic liquids, gel) [114]. The organic electrolyte, $\text{Li}_{10}\text{GeP}_2\text{S}_{12}$ and the ionic liquid are highlighted and exhibit highest conductivities.

2.2.3.1 About the degradation of state-of-the-art electrolytes

State-of-the-art electrolytes suffer from electrochemical aging, calendar aging, cycle aging and thermal aging [113][118][119]. The electrochemical aging, caused by e.g. SEI formation or exfoliation of graphite, leads to an impedance rise of the cell and may cause capacity fading. Calendar aging is mainly influenced by the storage conditions of the LIB. No less important is the thermal aging of the electrolyte, since it happens even without any contact to the electrodes and is accelerated at higher temperatures [120]. Thermal analysis methods indicate that the thermal stability of LiPF_6 is clearly decreased in the presence of protic impurities due to formation of PF_5 and $\text{O}=\text{PF}_3$ [121][122][123]. To understand the importance of the formation of the latter several working groups focus on the thermal degradation of electrolytes at elevated temperature [119][124][125][126]. Figure 16 displays the proposed autocatalytic cycle by Campion et al., which is still confirmed by other results of different research groups. They suggest that the formation of $\text{O}=\text{PF}_3$ is critical for the electrolyte, since it further decomposes alkylated carbonates. As shown by their NMR measurements, fluorophosphoric acid ($\text{O}=\text{PF}(\text{OH})_2$), difluorophosphoric acid ($\text{O}=\text{PF}_2(\text{OH})$), dialkyl fluorophosphates ($\text{O}=\text{PF}(\text{OR})_2$), alkyl difluorophosphates ($\text{O}=\text{PF}_2(\text{OR})$), alkyl fluorides (RF) and oligoethylene oxides ($-\text{OCH}_2\text{CH}_2-$) are the main thermal decomposition products of electrolytes based on LiPF_6 . GC-MS analysis further detects carbon dioxide (CO_2), alkylated ethers (R_2O), ethylene ($\text{H}_2\text{C}=\text{CH}_2$) and

oligoethylene oxides (-OCH₂CH₂-) as decomposition products. The formation of the oligoethylene oxides may derive from acid-catalyzed ring opening polymerization reaction of EC by PF₅ [127].

Among the linear carbonates, DEC is found to be most susceptible to thermal degradation since the nucleophilic attack more likely occurs on an ethyl than on a methyl group [119][122]. Also the impact of protic impurities on thermal degradation is studied by spiking certain samples with water. In that respect, Kawamura et al. [128] state that an increase in temperature leads to increased hydrolysis of LiPF₆. Terborg et al. [129] show that the influence of water on thermal degradation of electrolytes is less severe than an increase in temperature.

Whereas the two former publications support the formation of alkylated fluorophosphates, only the hydrolysis of LiPF₆ without any indication of carbonate decomposition is observed by Yang et al. [123]. They show that the addition of water to the electrolyte solely leads to an increase in HF formation when the electrolyte is aged in high density polypropylene bottles. In consideration of different housing materials for thermal degradation of electrolytes, it is significant that many decomposition products only are found, if the electrolyte is in contact with glassware as performed in [119][122][125][126] [127][130][131].

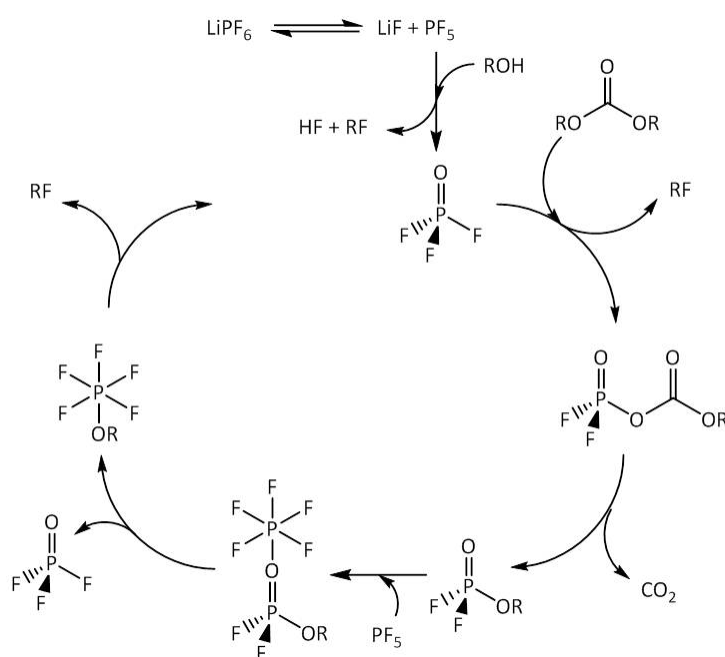


Figure 16: Proposed thermal degradation pathway for aprotic liquid electrolytes using LiPF₆ as conductive salt. Redrawn from [119].

Lux et al. [130] follow the HF formation during thermal decomposition by measuring the etching depth of silicon wafers via spectroscopic ellipsometry. They demonstrate that HF formation is divided into different stages and assume that the presence of SiO₂ might accelerate its formation. Their proposed catalytic cycle containing SiO₂ is shown in Figure 17.

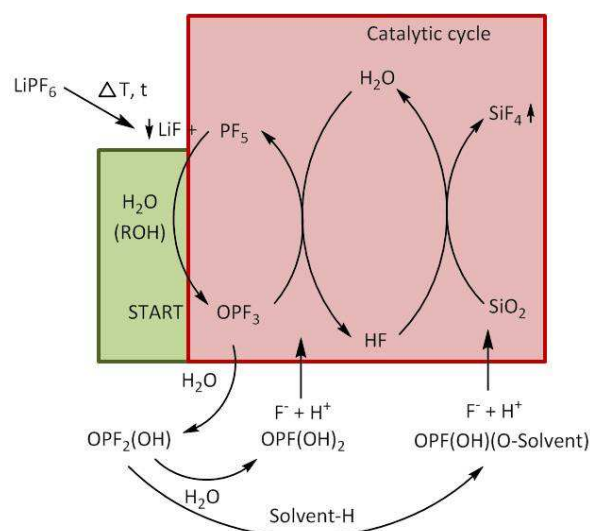


Figure 17: Hydrolysis of the conductive salt and subsequent reaction of generated HF with SiO₂ proposed by Lux et al. [130].

Heider et al. [132] show that stainless steel or aluminum containers should be favored compared to plastics since the diffusion of water is avoided. Thermal aging of electrolytes, sealed in glassware, does not resemble the environment of a commercial lithium-ion battery and seems inappropriate since it is far from real application. Therefore, the housing material for the electrolyte during storage or thermal aging might be crucial to trace back the origin of the calendar and cycle life of a LIB and should be chosen close to packaging materials applied in real applications.

2.2.3.2 Negative electrode/electrolyte interface and its fading mechanisms

The thermodynamic instability of electrodes regarding the E_g of state-of-the-art electrolytes makes the development of interfaces between the electrode and the electrolyte unavoidable. Shortly after Peled shows that an interface develops when an alkali or alkaline earth metal is in contact with non-aqueous electrolyte [27], he terms this passivating layer formed on a lithium anode solid electrolyte interphase (SEI) [133]. This passivation layer also exists on graphite since the energy of graphite lies beyond the E_g of state-of-the-art electrolytes (cf. Figure 14). The SEI formation during the 1st charge/discharge cycle consumes electrolyte and mobile lithium-ions and hence leads to irreversible capacity losses. These losses are accepted due to a prolonged cycle life of the battery and hence, further electrolyte decomposition on the negative electrode is mostly avoided. An ideal SEI allows Li^+ ions to pass through, whereas it is impermeable to electrons and solvated species.

The common used carbonate solvent PC sufficiently passivates the lithium anode, whereas graphitic active materials are not cyclable with PC. However, EC [134] is observed to be effectively reduced during the first charge of graphite and ensures reversible cycling performance. Hence, almost all non-aqueous liquid electrolytes mostly contain EC in combination with at least one low viscous, linear carbonate. The onset of SEI formation during the 1st charge and its constituents greatly depend

on the battery components (e.g. electrolyte composition), electrochemical conditions (e.g. potential window) and physical conditions (e.g. cycling temperature) [135]. Nevertheless, the most widely adopted onset for the SEI formation is 0.8 V vs. Li/Li⁺. The reduction of salt anions and carbonate solvents leads to the formation of inorganic and organic species, respectively. The SEI close to the graphitic surface is mainly composed of inorganic species, whereas the outer layer consists primarily of organic species. Table 7 summarizes some organic and inorganic reduction products for two different electrolyte systems. The use of DMC leads to the formation of PEO, which can, to some extent, positively influence the flexibility and elasticity of the SEI. Peled et al. [136] show that a difference of the SEI composition not only exists in its construction, but also between the basal and cross-section of graphite. Organic species are found as main constituents of the basal plane, whereas a high lithium-ion conductivity is necessary for the composition of the SEI on the cross-section. The latter is comprised of mainly inorganic species, which is favorable since hereby, lithium-ion diffusion channels are not blocked by non-conductive polymers.

Table 7: Dependence of the composition of the SEI on the electrolyte used [134][137][138].

Electrolyte	SEI composition
LiPF ₆ in EC:DEC	(CH ₂ OCO ₂ Li) ₂ , Li ₂ CO ₃ , ROCO ₂ Li, LiF, CH ₃ CH ₂ OLi, ROCOOR, C ₂ H ₅ OCO ₂ Li, Li ₂ O
LiPF ₆ in EC:DMC	(CH ₂ OCO ₂ Li) ₂ , Li ₂ CO ₃ , ROCO ₂ Li, LiF, CH ₃ OCO ₂ Li, LiOH, PEO

During prolonged cycling, a partial degradation due to mechanical stresses and following repair of the SEI leads to an increased thickening and interfacial resistance thereof with time [133][139]. To avoid that the performance of the LIB worsens, it is absolutely necessary to tune the composition and the characteristics of the SEI by the choice of the appropriate constituents. Further, additives or surface modifications on the graphite directly influence the composition of the SEI [138]. To sum up, a good SEI should have the following prerequisites [133][135]:

- ◆ Maximum lithium-ion conductivity, no electron conductivity
- ◆ Fast formation kinetics as well as uniform morphology and composition
- ◆ Compact and hole free layer to avoid further electrolyte reduction
- ◆ A high content of inorganics such as Li₂CO₃ which are stable to electrolyte dissolution
- ◆ Adequate LiF content to avoid a huge resistivity of the film
- ◆ A certain content of polymeric species to combat mechanical stresses

Vinylene carbonate (VC) is of particular interest as additive, since the vinyl group polymerizes reductively on the surface of lithiated graphite [109]. As a result, the formed SEI is rather composed of polymeric lithium alkyl carbonate groups, which render more flexibility and cohesion to the layer

[109][140]. Therefore, the addition of a few percent of VC reduces the irreversible capacity of the initial cycles, improves the thermal stability of the SEI and thereby enhances the cycle life performance of the LIB at ambient and especially at elevated temperatures [109][140][141].

Capacity fading of LIBs mainly originates from the degradation of the electrode/electrolyte interface, whereby a change in the active material or composite electrode may also evoke a capacity decay [142]. Regarding the graphite/electrolyte interface, several reasons may provoke capacity fading. Some degradation causes are shown in Figure 18. The build-up of an ineffective SEI leads not only to co-intercalation of solvents and lithium-ions, but also lithium may be trapped within the SEI. Dendrite formation and subsequent short circuits mainly occur at locations within the SEI, where the conductivity is highest or electrons are tunneled/dissolved [133]. Another problem arises with the thickening upon cycling of the LIB, since excessive polymer content might block lithium-ion migration [136]. Further, water introduced from the electrolyte solvents or the cathode material may decompose LiPF_6 and might lead to the distortion of the SEI layer [138]. If graphite is cycled with manganese spinel, the incorporation of Mn^{2+} in the SEI also might have a negative impact on electrochemical performance [143].

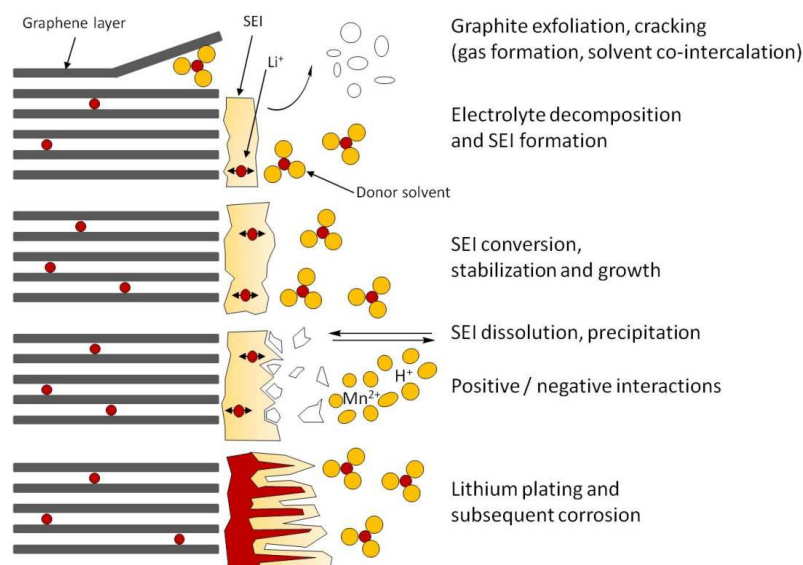


Figure 18: Build-up and degradation of the SEI on graphite. Redrawn from [142].

Anyway, the most severe consequences of electrode/electrolyte interface breakdown occur at high cell operating temperatures and/or high charge rates [138]. Early decomposition of the thin SEI layers already occurs around $110\text{ }^\circ\text{C}$ and ensuing aggressive surface reactions bear a huge thermal runaway risk of the LIB [144][145]. Therefore, regarding non-aqueous LIBs the absolute necessity of an effective SEI on the graphite anode is mandatory for their application in large scale applications such as BEV.

2.2.3.3 Positive electrode/electrolyte interface, causes for capacity fading and Mn^{2+} -dissolution

Until now, the composition of the SEI on the anode is well established. Less attention is paid to the positive electrode/electrolyte interface. Nevertheless, cathodes as well as anodes exhibit an impedance rise upon cycling, indicating the formation of passivating surface films on both.

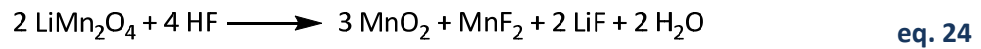
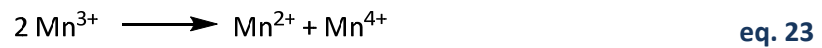
Before cell assembly, bare positive electrodes are covered with a thin Li_2CO_3 layer [146]. Considering Figure 14, the application of cathode materials with a higher operating voltage leads to the oxidation of non-aqueous electrolytes. Hence, similar passivation phenomena can be followed on positive electrode materials after charging/discharging of the LIB as for graphite. Generally, all cathode materials are covered by surface films, which might be comprised of following oxidation products: LiF , Li_2CO_3 , MF_2 , $Li_xPO_yF_z$, lithium alkyl carbonates, metal alkyl carbonates, metal carbonate and/or polycarbonates [147][148]. PEO is only observed on layered cathodes such as $LiCoO_2$ [146]. As for the graphitic SEI, surface films on the cathode depend on the battery constituents as well as on physical and electrochemical conditions. Therefore, the addition of additives such as fluoroethylene carbonate changes the morphology and the composition of the surface layer on e.g. $LiFePO_4$, which leads to a surface film with lowered impedance at low temperatures [149].

Capacity fading evoked by positive electrodes might be caused by the following three reasons [142][150]:

- ◆ Structural changes of the cathode material during cycling
- ◆ Chemical dissolution of transition metals into the electrolyte or decomposition reactions
- ◆ Surface film modifications

A possibility to prevent transition metal dissolution is to apply coatings to the materials. MgO and carbon coating seem effective for $LiCoO_2$ and $LiFePO_4$, respectively [148]. Considering the thermal runaway, a problematic effect of the reaction between cathodes and the electrolyte is the development of toxic, fluoro-organic products [144]. Further, structural instabilities make some positive electrode materials prone to oxygen release [145].

Special attention among positive electrode materials is warranted to manganese spinel. This material suffers from thermodynamic instability and electrolyte oxidation, when charged. Moreover, in a discharged state, manganese spinel undergoes structural changes due to disproportionation reactions (cf. eq. 23) as well as decomposition reactions (cf. eq. 24) with HF from the electrolyte [143][147][150].



As illustrated in Figure 19, both phenomena result in the dissolution of Mn^{2+} -ions into the electrolyte. Dissolved manganese ions could migrate to the negative electrode active material and deposit on its surface. Whenever graphite is cycled with manganese spinel electrodes (both without surface modifications and electrolyte additives), a capacity decay is noticed with time. Tsunekawa et al. [151] show that capacity fading of lithiated graphite occurs if both, manganese quantity and water content in the electrolyte are high. Even if they show that there exists a good correlation between the capacity fade and the manganese content, no absolute proof is provided that the manganese deposition within and on the SEI is the main reason for the capacity decay. Xiao et al. [143] conclude from their experiments on manganese dissolution that the capacity decay as well as polarization of the cell might be evoked by the incorporation of metallic manganese nanoclusters, which thickens the SEI. Anyway, there seems to be a correlation between manganese ions and capacity decay within the LIB.

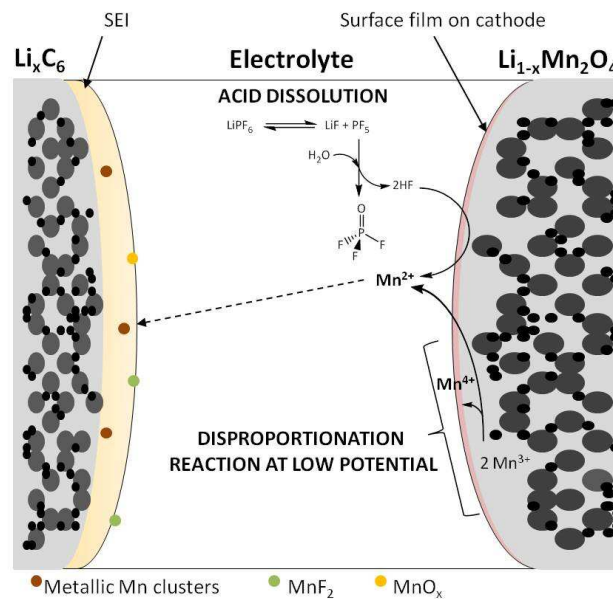


Figure 19: Scheme of Mn^{2+} dissolution from spinel $\text{Li}_{1-x}\text{Mn}_2\text{O}_4$ and subsequent migration and incorporation in the SEI of the graphite.

2.2.4 Separators for liquid electrolyte LIBs

Generally, a separator is a porous membrane that is positioned between the two electrodes of the LIB. Therefore, it inhibits electrical contact between the electrodes and short circuits of the cell, whereas it provides sufficient lithium-ion transport [152]. Three different classes of separators are applied in liquid electrolyte LIBs [153]:

- ◆ Microporous polymer membranes
- ◆ Non-woven fabric mats
- ◆ Inorganic composite membranes

The first class is the most widely used separator in LIBs. By virtue of their shutdown characteristics at elevated temperatures, especially bi-layers or tri-layers of polyethylene (PE) and polypropylene (PP) are preferably used. During closure of the pore structure by melting of PE, PP remains the integrity of the membrane and the thermal runaway of the LIB can be avoided [153]. These membranes mostly possess a low thickness ($\sim 25 \mu\text{m}$) and a pore size of more than $50\text{-}100 \text{ \AA}$ [152][153].

Due to their labyrinth like structure, dendritic deposition of lithium-ions is avoided in non-wovens. Nevertheless, the difficulty of fabricating thin films and simultaneously preventing short circuits of the cell cannot be achieved [153]. Hence, they attracted only little attention in the application for LIBs.

The third class of separators is called inorganic composite membranes. Particularly composites of non-woven polymeric and ceramic materials such as Separion[®] seem promising for large scale applications of LIBs. Their implementation increases the safety of LIBs through two different mechanisms: Firstly, the polyolefin part exhibits shutdown properties and secondly, the ceramic amount shows zero dimensional shrinkage at elevated temperature [153]. But no less important is its exceptional wettability property and thus, reduced electrical resistance of the separator. Therefore, this separator can be even applied for electrolytes with a high content of cyclic carbonates as well as ionic-liquid based electrolytes [153][154].

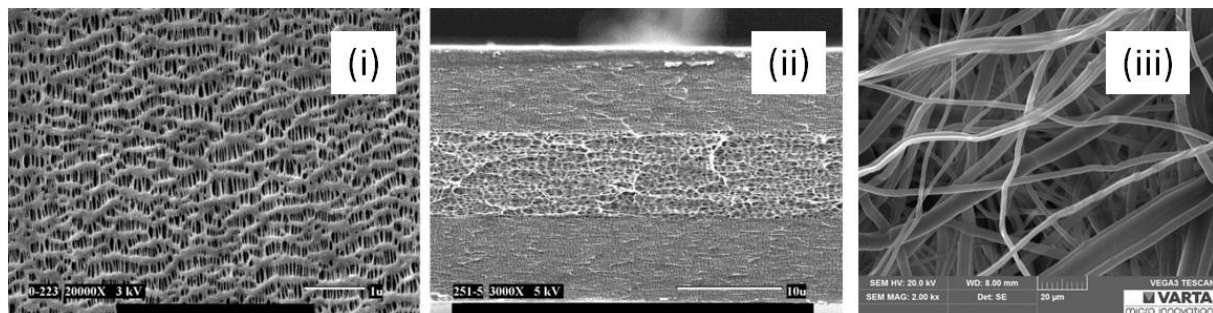


Figure 20: Surface (i) and cross section (ii) of a tri-layer polyolefin separator. [152] Surface of the non-woven Freudenberg FS 2190 separator (iii).

2.2.5 Strategies for increasing the energy density of LIBs and summary of their functional principle

The application of rechargeable LIBs in the automotive sector needs the supply of high energy density cell stacks for BEV to extend the driving range. State-of-the-art LIBs actually achieve values around 150 Wh kg^{-1} [155]. An advancement of currently used intercalation electrodes can result in a doubling of the latter. The exploration of new active materials or electrolytes is challenging since battery developers always need to consider the whole cell [36].

New systems that are based on conversion reactions such as lithium-sulfur or lithium-air batteries might even increase the energy density fivefold [155] compared to today's applied LIBs (cf. Figure 5). Even though their high capacities are greatly superior, drawbacks such as limited cycle life due to the application of lithium as negative electrode material, irreversible changes in the sulfur-carbon composite electrode or the development of suitable electrolytes for lithium-air batteries require huge efforts in research activities [156][155][76]. Another access to maximize the specific energy density of a cell is the cell design [157]. Srinivasan and Newman [158] proposed a model for a natural graphite/LiPF₆ in EC:DEC /LiFePO₄ battery. They showed that a proper design of porosity and thickness of the cathode increases its specific energy density. Figure 21 illustrates the weight distribution of an average cell design. The positive electrode has the main weight contribution. If the weight ratio of positive electrode to negative electrode is altered so that their capacity ratio is minimized, a higher specific energy of the cell is the result. Nevertheless, the possibility of lithium plating on the negative electrode increases. Therefore, the orientation of the cell design towards its application is indispensable. A proper capacity ratio between anode and cathode as well as an appropriate amount of electrolyte is necessary to meet safety aspects and to ensure the lithium-ion transport, respectively. Generally, cell stack components are assembled in cylindrical, coin, prismatic or in a thin and flat battery configuration [33]. As illustrated in Figure 21, the three main cell stack components of a rechargeable LIB are the positive electrode, the negative electrode and the electrolyte.

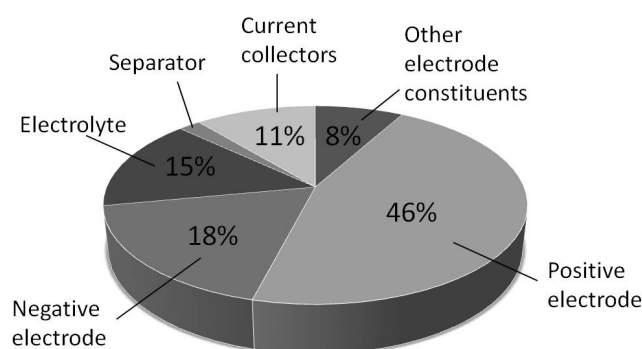


Figure 21: Weight distribution of cell stack components (averaged). Redrawn and modified from [23]

Both electrodes primarily consist of active material, but electrode constituents such as binders (e.g. PVdF, Na-CMC) and conductive agents (e.g. carbon black) are needed for electrode fabrication. The current collector of the positive and negative electrode is usually aluminum and copper, respectively. The electrode design may differ. Whereas an optimum service life and high capacities at low C-rates upon discharging are achieved by high mass loadings, high rate performance electrodes are fabricated by considering the enlargement of reaction surfaces [16].

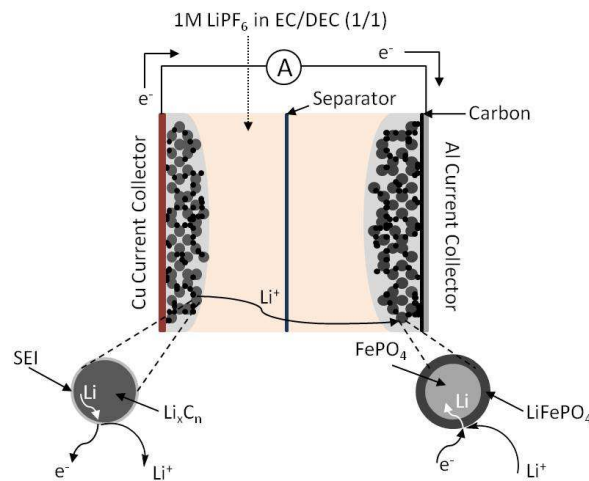
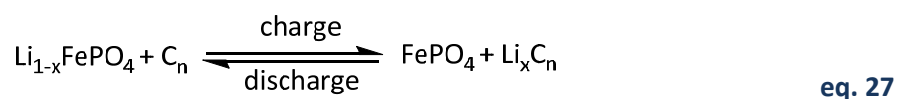
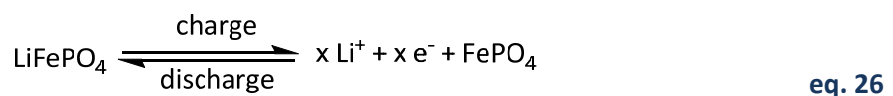
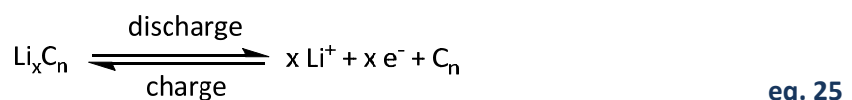


Figure 22: Functional principle of the discharging process of a LIB consisting of graphite and LiFePO_4 . The discharging of the positive electrode is shown for the shrinking core model of LiFePO_4 . Modified and redrawn from [158].

To avoid the contact between the positive and the negative electrode and hence to prevent short circuits, a separator that is soaked with non-aqueous electrolyte (e.g. 1 M LiPF_6 in EC/DEC; 1/1 per weight) is used. Since LIBs are normally assembled in their discharged state [33], the LIB needs to be charged first. As most state-of-the-art LIBs use graphite as negative electrode material, irreversible losses occur due to the reduction of the electrolyte and related SEI formation (approx. 80 % [40] charge recovery within the 1st cycle). Figure 22 illustrates the discharging of a LIB that uses graphite and LFP as negative and positive electrode material, respectively. Upon discharging, graphite is oxidized and LFP is reduced. During charging, the reactions are reversed. The reactions that occur for the two intercalation electrodes are summarized in eq. 25 and eq. 26:



3 Experimental

In general, all of the measurements were performed under reproducibility conditions (two to three fold determinations) with validated methods considering requested measurement range, accuracy and precision. The assembly of test cells was carried out in an argon-filled glove box ($\text{H}_2\text{O} < 1$ ppm, $\text{O}_2 < 1$ ppm).

3.1 Synthesis and characterization of phospho-olivines LiMPO_4 (M= Fe, Mn Co)

3.1.1 Solid state synthesis of $\text{LiFe}_{0.5}\text{Mn}_{0.5}\text{PO}_4$

The solid state synthesis was performed according to Chen and Dahn [159], whereas the ball milling step of the powders was performed for 6 hours in acetone at 300 rpm. Therefore, appropriate amounts of $\text{NH}_4\text{H}_2\text{PO}_4$, Li_2CO_3 , $\text{FeC}_2\text{O}_4 \cdot 2\text{H}_2\text{O}$ and $\text{MnC}_2\text{O}_4 \cdot 2\text{H}_2\text{O}$ were mixed together and after evaporation of the acetone, the samples were pressed to a pellet with a pressure of 2 metric tons. The values for the heat treatment were taken following the publication of Chung et al. [160]. The samples were heated under inert atmosphere to 350 °C for 10 hours to eliminate volatile reaction products. Afterwards, the pellets were reground with 20 wt% Super P in the ball mill (Fritsch Pulverisette 7). The resulting powders were again pressed into a pellet and solid state synthesis was performed under inert atmosphere at 700 °C for 24 hours. Further slurry preparation was carried out according to Table 10.

3.1.2 General procedure for microwave-solvothermal synthesis of LiFePO_4 , LiMnPO_4 and $\text{LiFe}_x\text{Mn}_{1-x}\text{PO}_4$ and doping thereof

Due to the variety of different samples, LiFePO_4 , LiMnPO_4 and exactly defined contents of $\text{LiFe}_x\text{Mn}_{1-x}\text{PO}_4$ are further denoted according Table 8. The synthesis procedure was similar to that proposed by Murugan et al. [161].

For the preparation of sample A to sample K, $\text{Fe}(\text{CH}_3\text{COO})_2$ and/or $\text{Mn}(\text{CH}_3\text{COO})_2 \cdot 4\text{H}_2\text{O}$ in tetraethylene glycol was/were dissolved in tetraethylene glycol (TEG) for 4 ½ to 5 hours. Then, H_3PO_4 and a solution of $\text{LiOH} \cdot \text{H}_2\text{O}$ in TEG was added to the latter and the pH was then adjusted to the proper value. The ratios of lithium, phosphate and iron/manganese were equimolar. The final concentration of the reaction mixture was 0.14 mol L^{-1} . The synthesis of the homogenous mixture occurred in a quartz vessel, which was carefully sealed by a Teflon[®]-coated silicone septum. An Anton Paar Monowave 300 microwave oven was operated at 600 W and temperature and pressure were controlled on-line during reaction (cf. Figure 23).

Table 8: Summary of the sample denominations used within the experimental as well as within the results and discussion part of this thesis.

	x	y	Sample denomination
LiFe_xMn_{1-x}PO₄/C	1.0	-	A
	0.9	-	B
	0.8	-	C
	0.7	-	D
	0.6	-	E
	0.5	-	F
	0.4	-	G
	0.3	-	H
	0.2	-	I
	0.1	-	J
	0.0	-	K
	0.5 ^a	-	L
	0.5 ^b	-	M
LiFe_xMn_xMg_{1-2x}PO₄/C	0.490	-	N
	0.485	-	O
	0.480	-	P
	0.475	-	Q
	0.470	-	R
LiFe_xMn_yCo_{1-x-y}PO₄/C	1/3	1/3	S
	0.5	0.25	T
	0.4	0.4	U

^a Mechanically mixed LiFePO₄ and LiMnPO₄ together in the ball mill with sucrose.

^b Mixing of LiFePO₄ with sucrose and LiMnPO₄ with sucrose separately in a ball mill and subsequently mixing of the two products by using an agate mortar before the oven.

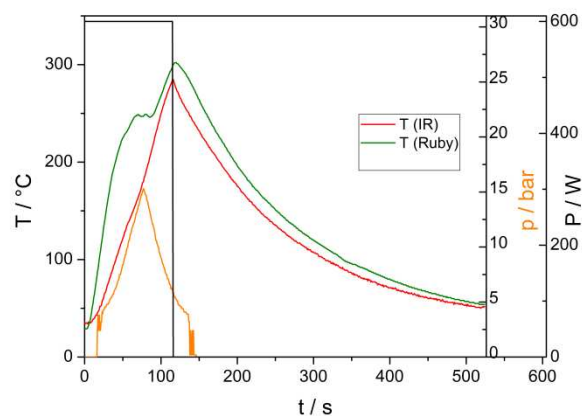


Figure 23: Typical profile of the microwave solvothermal synthesis.

Resulting products were filtrated, washed with acetone and dried over night at 60 °C. All prepared samples were thoroughly mixed with 20 wt% sucrose in N-Methyl-2-pyrrolidon (NMP) for 1 hour at 300 rpm in a ball mill (Fritsch Pulverisette 7). The weight ratio of solids to NMP was 1:3.5. Moreover, the mixture of equivalent amounts of Fe and Mn was prepared by mechanical mixing of the required amount of sample A, sample K and sucrose together in the ball mill (sample L). Another mixture with an equimolar content of Fe and Mn was prepared by separate ball mill mixing of sample A or sample K with sucrose and afterwards mingled manually by using an agate mortar (sample M). Samples A-M were annealed at 700 °C for 10 hours under inert atmosphere to obtain carbon coated species.

For the preparation of Mg-substituted $\text{LiFe}_x\text{Mn}_x\text{Mg}_{1-2x}\text{PO}_4$ ($x= 0.47-0.49$ in 0.005 eq.-steps) $\text{Mg}(\text{CH}_3\text{COO})_2 \cdot 4\text{H}_2\text{O}$ was added to a solution of $\text{Fe}(\text{CH}_3\text{COO})_2$ and $\text{Mn}(\text{CH}_3\text{COO})_2 \cdot 4\text{H}_2\text{O}$. Microwave-solvothermal synthesis was performed as for samples A-K.

3.1.3 Towards high voltage positive electrode materials

Solid solutions of $\text{LiFe}_x\text{Mn}_y\text{Co}_{1-x-y}\text{PO}_4/\text{C}$ were formed by direct microwave solvothermal synthesis of $\text{Fe}(\text{CH}_3\text{COO})_2$, $\text{Mn}(\text{CH}_3\text{COO})_2 \cdot 4\text{H}_2\text{O}$ and $\text{Co}(\text{CH}_3\text{COO})_2 \cdot 4\text{H}_2\text{O}$. Table 9 gives a summary of the synthesized products, whereby x and y state the equivalents of Fe and Mn within the structure.

Table 9: Summary of the synthesized $\text{LiFe}_x\text{Mn}_y\text{Co}_{1-x-y}\text{PO}_4/\text{C}$ for both preparation methods

	x	y
$\text{LiFe}_x\text{Mn}_y\text{Co}_{1-x-y}\text{PO}_4/\text{C}$	0	0
	1/3	1/3
	0.5	0.25
	0.4	0.4

Carbon coating with sucrose and the post-annealing step were performed as mentioned in section 3.1.2.

3.1.4 Measurement methods and setups for positive electrode materials

All samples described in chapter 3.1.1-3.1.3 were characterized before slurry preparation. The main focus was on the determination and verification of the crystal structure of all synthesized samples. Phospho-olivine electrodes were prepared according to Table 10.

After casting the slurry with a film thickness of 30 μm on a 30 μm thick aluminum foil by doctor-blade technique, the electrode sheets were dried overnight in a vacuum oven at 80 $^{\circ}\text{C}$. The total composite electrode had a final mass load of 1.8 to 3.0 mg cm^{-2} .

Table 10: Slurry composition of synthesized phospho-olivine electrodes

	Component	Composition / wt%
Active material	Phospho-olivine	80
Conductive agent	Super P TM Li	12
Binder	PVDF Kynar [®] 761	8
Solvent	NMP*	-

*Amount depending on the viscosity of the slurry.

◆ XRD analysis

XRD patterns of all synthesized materials were recorded on a Bruker D8 Advance diffractometer by using Cu-K α radiation between 10-80 $^{\circ}$ 2 θ range (scan rate: 0.02 $^{\circ}$ s $^{-1}$). X'Pert High Score Plus (PANalytical) was used for Rietveld analysis. Therefore, reference diffractograms from the Inorganic Crystal Structure Database (ICSD) were applied. The refinement occurred until the measured and calculated profiles matched best. Following ICSD reference data was used: #92198 for LiFePO $_4$ /C, #1672252 for LiMnPO $_4$ /C and #54825-54829 for doped and undoped LiFe $_x$ Mn $_{1-x}$ PO $_4$ /C. The ICSD reference data #54826 was used to analyze the XRD diagrams of LiFe $_x$ Mn $_y$ Co $_{1-x-y}$ /C. Therefore, the diffractograms were semi-quantitatively analyzed by refining the flatting of the background, the scaling factor, atomic coordinates and the zero shift. Then, Co was added as atom and the exact occupancy of each transition metal was adjusted. Another semi-quantitative refinement occurred until the final lattice parameters were obtained.

◆ SEM and EDX analysis

The morphology of the powders was analyzed by Tescan Vega3 scanning electron microscope equipped with an Oxford Instruments INCAx-act EDX detector for determination of the elemental composition. To enhance the conductivity of the samples, a thin gold layer was applied to their surface through sputter coating.

Slope cuts of casted electrode films (samples F, L and P) on aluminum foil were prepared by a Gatan Iilion™ Broad Ion Beam Argon Milling System. Cross-sections of the samples were analyzed by BSE-SEM and EDX spectroscopy.⁴

◆ Cell assembly, CV and CC measurements

Cell assembly occurred in a Swagelok®-T-cell with metallic lithium as counter and reference electrode (cf. Figure 24). A polypropylene non-woven separator (Freudenberg FS2190) was used for separation of the two electrodes. It was soaked with non-aqueous electrolyte consisting of 1 M LiPF₆ in EC:DEC (37.6:62.4, w/w, Purolite®).

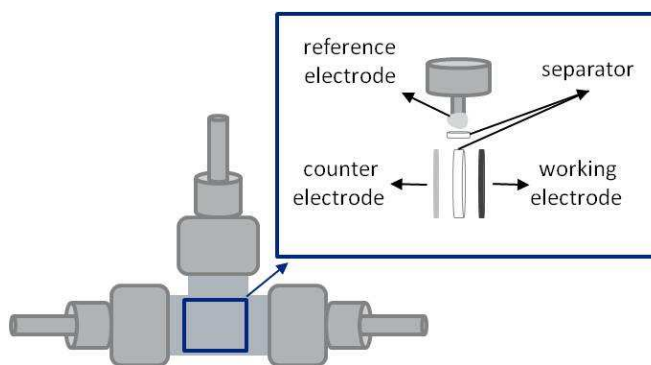


Figure 24: Schematic illustration of a Swagelok®-T-cell

CV measurements were recorded on a battery test station (Bio-Logic MPG-2) with a scan rate of $30 \mu\text{V s}^{-1}$ and repeated twice to prove reproducibility. The Swagelok®-T-cells were subsequently cycled on a battery tester (MACCOR Series 4000). Unless otherwise stated, cells were fully charged/discharged with 0.1 C for 50 times with a constant voltage step for 1 hour after each cycle (CCCV). The voltage range was 3.2-3.8 V, 3.2-4.4 V and 3.2-4.7 V vs. Li/Li⁺ for LFP, LFMP and LMP, respectively. The voltage range for LFMCP was 3.0-4.9 V vs. Li/Li⁺ and 3.5-5.1 V vs. Li/Li⁺ for LCP. This cycling was followed by a rate capability test with 0.1 C, 0.5 C, 1 C and 0.1 C for 5 cycles each. 1 C refers to the theoretical capacity of each material (approx. 170 mAh g^{-1}). Considering that 80 wt% of active material was contained in the final mass load of the composite electrode, the electrodes were charged/discharged with 0.28-0.46 mA.

◆ ICP-OES

ICP-OES measurements⁵ were performed to detect the manganese that was deposited on the lithium metal counter electrode. After cycling, the counter electrodes were dissolved in 2 mL high purity water, 1 mL HCl and 5 mL HNO₃ by using a commercial microwave-assisted sample digestion system (Multiwave 3000). Temperature and pressure was no more than 240 °C and 40 bar, respectively.

⁴ Performed by the Austrian Centre for Electron Microscopy and Nanoanalysis FELMI-ZFE, Graz.

⁵ Performed by the Institute for Analytical Chemistry and Food Chemistry, Graz, University of Technology.

Quantification of manganese occurred by external calibration on a CIROS Vision ICP-OES with scandium as internal standard. The Mn (II) 257.661 nm emission line was used.

◆ *GITT*

GITT measurements were performed in Swagelok®-T-half cells of the samples C, I and K. The formation step of the cells occurred at 0.1 C between a voltage range of 3.2 to 4.4 V vs. Li/Li⁺. The cells were charged at 0.05 C for 40 minutes followed by a recorded relaxation of the voltage for two hours. As soon as 4.4 V were achieved, the discharge of the half cell to a voltage of 3.2 V occurred according to the aforementioned parameters (cf. chapter 5.2, Table 36). The current density was between 0.23 and 0.26 mA cm⁻² for LFMP.

◆ *Four point resistivity measurement*

The electrical conductivity of samples A, C, F, I and K was determined by four point resistivity measurements on a battery test station (Bio-Logic VMP3). Therefore, a slurry according to Table 10 was prepared for each material and casted on Mylar® foil by doctor-blade technique with a film thickness of 150 μm. The width of the dried samples was 1 cm, film thickness was determined by micrometer screw. The distance between two points was chosen to be 2.5 cm, 5 cm, 7.5 cm and 10 cm. Four point resistivity measurements occurred in galvanostatic mode with a current of 100 μA.

◆ *Particle sizing*

A particle size measuring instrument (Fritsch Analysette 22 NanoTec Plus) was used to determine the particle size distribution of the samples. Therefore, ~0.010 g Na₄O₇P₂*10H₂O was dissolved in ~10 mL deionized water and 0.1-0.2 g of sample and ~10 μL of Dusazin 901 were added. The suspension was dispersed in an ultrasonic bath at ambient temperature for five minutes (Fisher Scientific FB15063) and measured within a measurement range of 0.08-2000 μm.

3.2 Thermal aging of a state-of-the-art LIB electrolyte

3.2.1 General procedure

An electrolyte solution containing 1 M LiPF_6 in EC:DEC (40:60, w/w) was prepared in an argon-filled glove box and stirred for 15 hours. DEC and EC were distilled for further purification and dried by molecular sieve before use. Battery grade LiPF_6 was used as received. 10 mL of electrolyte was transferred into a multi-layer aluminum foil bag (pouch bag, 7.5 × 15 cm, cf. Figure 25) and carefully sealed under argon atmosphere. Contained water was determined by coulometric Karl Fischer titration and is summarized in Table 11. The influence of protic impurities and silicon species on the thermal aging in pouch bags was examined.

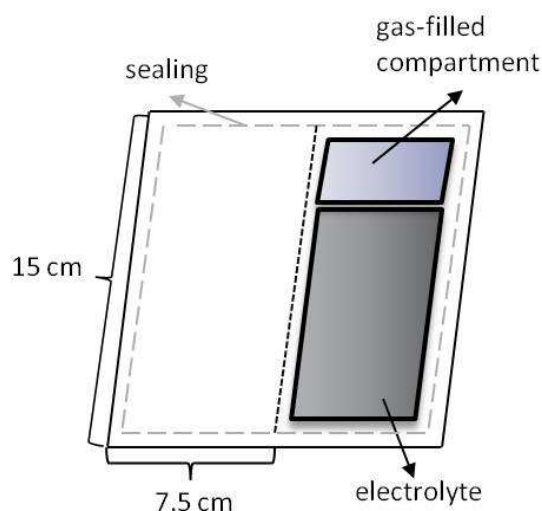


Figure 25: Schematic illustration of the measurement setup used for electrolyte aging.

Therefore, several pouch bags were stored at ambient and elevated temperature (60 °C). From all pouch bags subsamples were analyzed after 15 hours (termed as „fresh electrolyte”), 2 days (60°C), 7 days (60°C) and 28 days (ambient temperature and 60°C) according to section 3.2.2. CC charge/discharge experiments were only carried out for the electrolytes aged at 60 °C for 28 days.

Table 11: Added protic impurities and silicon species and their approximate water content

Electrolyte	Added species	Water content / ppm
1 M LiPF_6 in EC:DEC	75 μL deionized water	1000
1 M LiPF_6 in EC:DEC	0.053 g undried LiFePO_4	1400
1 M LiPF_6 in EC:DEC	0.015 g undried n- SiO_2 powder	10 300
1 M LiPF_6 in EC:DEC	0.015 g dried n- SiO_2 powder	400
1 M LiPF_6 in EC:DEC	0.015 g undried n-Si powder	2000

To show the influence of glass surface on thermal degradation, additional electrolyte samples were filled in glass vials (Supelco®) and sealed. Further samples were flame-sealed under reduced pressure in Duran® NMR-tubes.

3.2.2 Measurement methods and setups for electrolyte aging

◆ *Acid-base titration*

The total acid concentration of the electrolyte samples was determined by acid-base titration reaction using water-free sodium carbonate Na_2CO_3 and highly purified water (Milli-Q, Millipore). Therefore, approximately 1 g of electrolyte was diluted in ~100 mL Milli-Q water and titrated quickly with 0.002 M Na_2CO_3 -solution.

◆ *Coulometric Karl Fischer titration*

To determine the water content of liquid and solid samples, a Mitsubishi Moisture Meter Model CA-100 and a Mitsubishi Water Vaporizer Model VA-100 coupled to the CA-100 was applied. Approximately 1 g of liquid sample was directly injected into the CA-100. Solid samples were measured at an oven temperature of 300 °C and under argon carrier gas flow of approximately 250 mL min^{-1} . A delay time of two minutes was chosen and the measurement of the solid samples was carried out until a stable value of 0.1 $\mu\text{g s}^{-1}$ was reached.

◆ *NMR-spectroscopy*

Homo- and heteronuclear NMR-spectroscopy was performed on a Varian Mercury 300 MHz spectrometer. Samples aged in pouch bags were transferred in screw-mountable NMR-tubes. Flame-sealed Duran® NMR-tubes were measured without further treatment. To avoid the contamination with deuterated solvents, external lock signal was provided by a C_6D_6 filled glass capillary. ^1H - and ^{13}C -NMR spectra were referenced to the solvent residual signal, ^{19}F -NMR spectra to trichlorofluoromethane CCl_3F and ^{31}P -NMR resonances to phosphoric acid H_3PO_4 . Tetramethylsilane $\text{C}_4\text{H}_{12}\text{Si}$ was used as reference in ^{29}Si -NMR spectra. Spin lattice relaxation time (T_1) was determined via inversion recovery experiment. If only one decomposition product occurred within the decomposition region of the ^{19}F -NMR spectra, acquisition of quantitative ^{19}F -NMR spectra was performed. Therefore, the time between two scans (d1) was adjusted to be tenfold T_1 .

◆ *GC-MS and HS-GC-MS measurements*

All GC-MS spectra were recorded on an Agilent Technologies 7890 GC coupled with a mass selective detector 5975. Helium was used as carrier gas (constant flow rate: 1 mL min^{-1}). A HP-5MS capillary column (30 m x 0.32 mm x 0.25 μm) was applied for separation. The gas filled compartment of the pouch bags was analyzed by manual injection (Hamilton samplelock™ syringe, 2 mL gas volume per sample, split ratio of 1:500) into the split/splitless injector. The compounds were separated between

40 to 180 °C (rate 10 °C min⁻¹). To be able to detect certain decomposition products which might react with the GC column, a metal separation column (Ultra alloy[®] EGA tube, Frontier-Laboratories LTD.) with a length of 2.5 m and an inner diameter of 0.12 mm was applied. The gas filled compartment of certain pouch bags was analyzed by manual injection (Hamilton samplelock[™] syringe, 1 mL gas volume per sample, split ratio of 1:200). All compounds that evolve between 40 to 300 °C are detected by the mass spectrometer.

Dichloromethane (CH₂Cl₂) was chosen as diluent for the liquid electrolyte samples. Liquid electrolyte samples were injected via autosampler (split ratio of 1:100) and measured with a heating rate of 7 °C min⁻¹ from 38 to 45 °C, 10 °C min⁻¹ between 45 and 70 °C, and 20 °C min⁻¹ from 70 to 200 °C. The mass spectrometer operated in electron ionization (EI) mode with an electron energy of 70 eV.

◆ UV-Vis spectroscopy

Changes in color of the aged electrolytes were monitored by an UV-1800 UV-VIS spectrophotometer (Shimadzu Corp.) within a wavelength range from 800 to 200 nm.

◆ Cell assembly and CC experiments

Industrially manufactured electrodes were used for the assembly of pouch bicells (cf. Figure 26). LiFePO₄/C was chosen as positive electrode material (bilaterally coated, 5 × 3.1 cm, total mass load: 16.5 g cm⁻²), graphite as negative electrode material (butterfly-electrode, each 5.1 × 3.2 cm, total mass load: 7.0 g cm⁻²) and two microporous polymer films consisting of PP/PE/PP as separators (5.5 × 3.5 cm each). The composition of

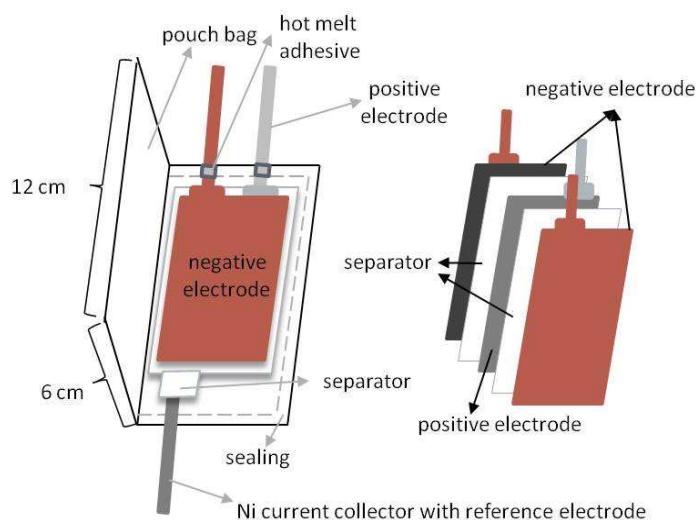


Figure 26: Schematic illustration of a pouch bicell.

the electrodes is summarized in Table 12. Lithium metal was assembled as reference electrode.

Table 12: Composition of the industrially manufactured electrodes.

Cathode	Composition / wt%	Anode	Composition / wt%
LiFePO ₄ /C	88	Graphite	91
Conductive agent	6	Conductive agent	6
PVDF	6	Binder	3

The separators were soaked with 0.6 mL of the fresh as well as aged electrolytes according to Table 13. MACCOR Series 4000 battery tester was applied for CC experiments. The formation of the pouch bicells occurred according to VARTA standard formation procedure for LFP electrodes. After the formation, the bicells were charged/discharged for 200 times between 2.4 and 3.6 V vs. Li/Li⁺ at a C-rate of 1 C which corresponds to 60 mA.

Table 13: Added electrolytes (1 M LiPF₆ in EC:DEC, 40:60, w/w).

Time	Temperature	Note
-	-	Fresh electrolyte
28 days	60 °C	In contact with polymer surface
28 days	60 °C	In contact with glassy surface
28 days	60 °C	+75 µL deionized water
28 days	60 °C	+0.015 g undried n-SiO ₂ powder

To examine the influence of aged electrolytes on the cell performance of LFMP solid solutions, Swagelok®-T-cells are assembled and cycled for active material C and active material K as mentioned in section 3.2.1.

4 Results and Discussion

4.1 Synthesis and characterization of next generation cathodes for LIBs

Since 1991, $\text{Li}_{1-x}\text{CoO}_2$ has become the most widely used positive electrode material in the LIB technology. Nevertheless, not only the high cost and toxicity of the transition metal cobalt but rather the significant risk of thermal runaways, enhanced through possible oxygen release, entails problems regarding customer applications. The absolute necessity for ensured safety among LIB application in portable devices and automotive batteries forces researchers to the exploration of new, safer battery chemistries. Therefore, phospho-olivines such as e.g. LiFePO_4 represent a promising positive electrode active material. In recent years, drawbacks such as their low electronic conductivity could be eliminated through carbon coatings or doping. Hence, phospho-olivines have become competitive with layered transition metal oxides and currently, some automobile manufacturers already use them for the construction of BEV. Anyway, to extend the driving range of BEVs, cells that provide higher energy densities are needed.

Within this chapter, the focus is on the synthesis of solid solutions like $\text{LiFe}_x\text{Mn}_{1-x}\text{PO}_4/\text{C}$ and, to a minor extent, $\text{LiFe}_x\text{Mn}_y\text{Co}_{1-x-y}\text{PO}_4/\text{C}$ to increase the oxidation potential that is supplied by the positive electrode material. Initially, to show the superiority of the microwave solvothermal synthesis over solid state synthesis methods, $\text{LiFe}_{0.5}\text{Mn}_{0.5}\text{PO}_4/\text{C}$ is compared to an electrode prepared by solid state synthesis method. Thereafter, the adjustment and optimization of some process parameters is shown. The electrochemical performances of $\text{LiFe}_x\text{Mn}_{1-x}\text{PO}_4/\text{C}$ ($x = 0, 0.1, 0.2, \dots, 1$ in 0.1 eq. steps) are discussed and the solid solution forming process is examined along every step of the material preparation process. Finally, high voltage electrode solid solutions $\text{LiFe}_x\text{Mn}_y\text{Co}_{1-x-y}\text{PO}_4/\text{C}$ are discussed.

4.1.1 Solid state synthesis versus solvothermal microwave assisted synthesis

Herein, the advantages of solvothermal microwave assisted synthesis of phospho-olivines are discussed and a comparison of them to the solid state synthesis method is made. Since the powders for solid state synthesis were prepared by mixing the precursor with Super P in a ball mill, a similar preparation procedure was also performed for the microwave synthesized powders. Basically, the microwave synthesized samples are prepared according to chapter 3.1.1, whereas the ball milling step occurred with 20 wt% Super P rather than sucrose. The two samples synthesized by solid state method did only differ in their educt concentrations and are further on named according to Table 14. The associated sample, which was synthesized by the solvothermal microwave method, is further on called MW.

Table 14: Precursor concentrations and sample denominations for the powders synthesized by solid state method.

Sample	Li ₂ CO ₃ / eq.	Fe ₂ O ₄ *2H ₂ O / eq.	MnC ₂ O ₄ *2H ₂ O / eq.	NH ₄ H ₂ PO ₄ / eq.
SS-1	0.6	0.5	0.5	1
SS-2	0.5	0.5	0.5	1

Structural characterization. The XRD diagrams (cf. Figure 27) of the received powders show some impurities for SS-1. Whereas the XRD patterns of sample MW and SS-2 do not contain any impurities, the pattern of SS-1 includes some reflexes of magnetite Fe₃O₄. Moreover, by comparison of the diffraction pattern to literature (cf. [162][163]), there are parts of some peaks that might correspond to heterosite species Fe_xMn_{1-x}PO₄. The excess of lithium carbonate when synthesizing sample SS-1 leads to comparable peak positions in the diffractograms. The stoichiometric sample SS-2 shows a slight shift to higher angles. This might result from internal strain, leading to a shift in d-spacing (e.g. structural defects).

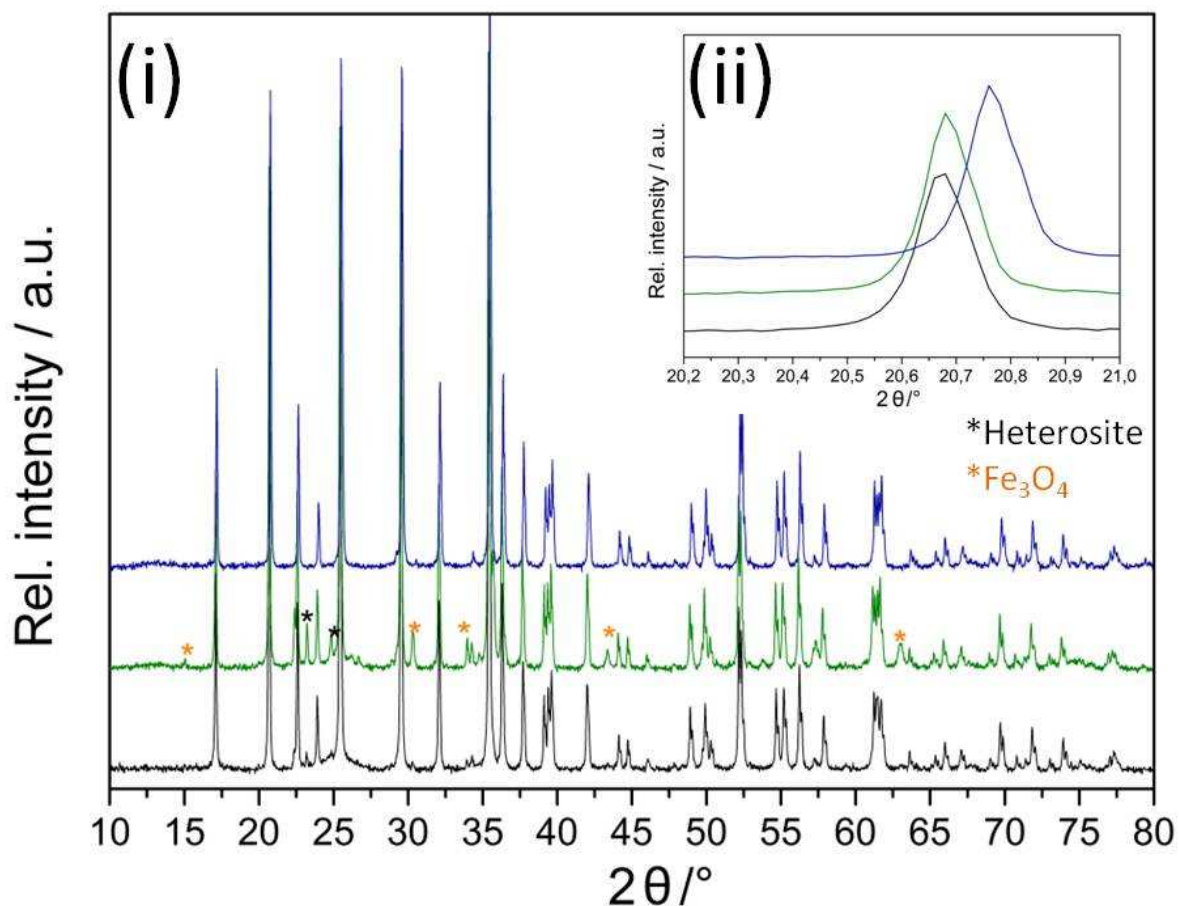


Figure 27: XRD patterns of LiFe_{0.5}Mn_{0.5}PO₄/C prepared by microwave solvothermal method (black) or solid state synthesis SS-1 (green) and SS-2 (blue). (i) Between 10-80° 2θ and (ii) magnified view between 20.2-21.0° 2θ.

Table 15 summarizes the obtained lattice constants after Rietveld refinement. It is obvious that the excess of lithium leads to an increase in lattice parameters. The value of lattice constant *c* is similar for sample MW and sample SS-2. On the other hand the lattice constants *a* and *b* show a slight

difference. For all samples, the nearly identical peak positions, peak intensities and lattice constants confirm that a similar crystal lattice has formed for the phospho-olivine.

Table 15: Summary of the lattice parameters of equimolar LFMP prepared by microwave-solvothermal synthesis and solid state synthesis. The standard deviation is shown in brackets.

Sample	a / Å	b / Å	c / Å	Volume / Å ³
MW	10.3781(1)	6.0506(1)	4.7218(1)	296.50
SS-1	10.3956(2)	6.0600(1)	4.7242(1)	297.61
SS-2	10.3908(1)	6.0550(1)	4.7200(1)	296.96

SEM images show that the morphology of the samples is fairly similar (cf. Figure 28).

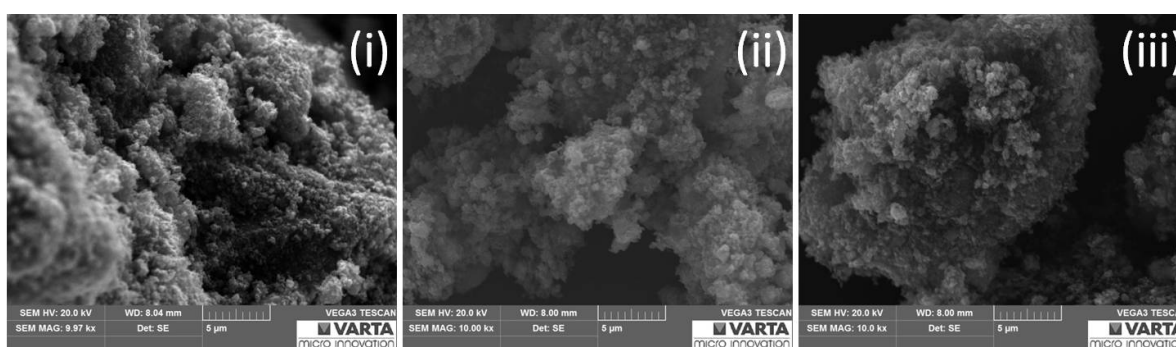


Figure 28: SEM images of (i) MW, (ii) SS-1 and (iii) SS-2 at a magnification of 10 kx.

Electrochemical tests. Regarding their electrochemical behavior, an explicit difference occurs considering sample MW and the two samples SS. The CVs of the samples show that sample MW is superior regarding the delithiation/lithiation capacities as well as efficiencies. Sample SS-1 exhibits severe capacity fading even at the application of low current densities. The reason to that might be the impurities of the sample. Since lithium-ion diffusion only occurs in one dimensionality, these impurities block diffusion channels trapping some lithium-ions potentially. Hence, the exact stoichiometric amount of precursors is imperative to achieve an acceptable electrochemical performance of the sample.

Table 16: Discharge and charge capacities and corresponding coulombic efficiencies of the 2nd cycle of the CV measurements.

Sample	Discharge cap. / mAh g ⁻¹	Charge cap./ mAh g ⁻¹	Efficiency / %
MW	107	108	99.2
SS-1	85	87	97.4
SS-2	93	93	100.0

Figure 29 compares the specific discharge capacity of sample MW only to that of sample SS-2. It is evident that sample MW performs slightly superior to active material SS-2. Whereas electrode MW

reaches an initial discharge capacity of approx. 90 mAh g^{-1} , the discharge capacity of electrode SS-2 is lower by 10 mAh g^{-1} .

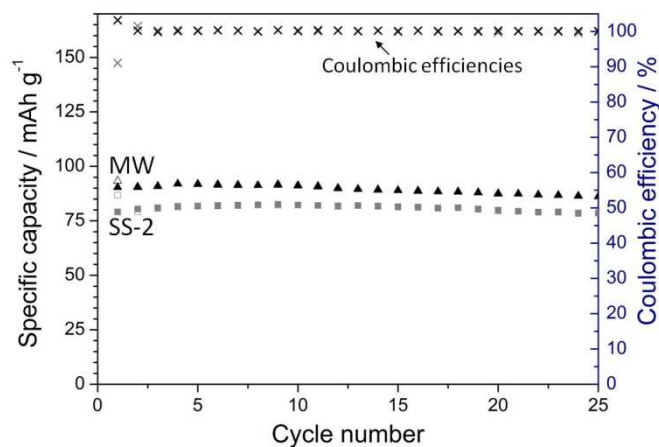


Figure 29: Comparison of the specific discharge capacities and efficiencies of the 1st 25 cycles at 0.1 C and ambient temperature of electrode MW (triangle) and SS-2 (square).

Phospho-olivines synthesized by microwave irradiation are superior regarding electrochemical performance and retaining of preparation time and thus energy compared to solid state synthesized samples. Therefore, a solvothermal microwave assisted synthesis with carefully adjusted process parameters is shown.

4.1.2 Solvothermal microwave assisted synthesis

4.1.2.1 Tuning of the synthesis process

Post-annealing step. Considering Figure 30, it is obvious that a post-thermal treatment after the microwave solvothermal synthesis is necessary to obtain a crystal structure at all and electrochemical activity as a consequence. Since the prespecified operating conditions of Anton Paar Monowave 300 do not allow higher operating temperatures (limited to $300 \text{ }^\circ\text{C}$), the exposure time of microwave irradiation to the sample was limited. The phospho-olivine phase is already formed after the microwave process. The peak positions are in good accordance with ICSD reference spectra, even if their intensities are poor. Anyway, the post-annealing step induces a rearrangement of the atoms in the unit cell, leading to a more crystalline and purer structure with defined pathways for lithium-ion movement. Sucrose decomposes during this step and increases the electronic conductivity of the samples. Therefore, the electrochemical performance improves remarkably and the two redox couples for $\text{Fe}^{2+}/\text{Fe}^{3+}$ and $\text{Mn}^{2+}/\text{Mn}^{3+}$ become clearly visible.

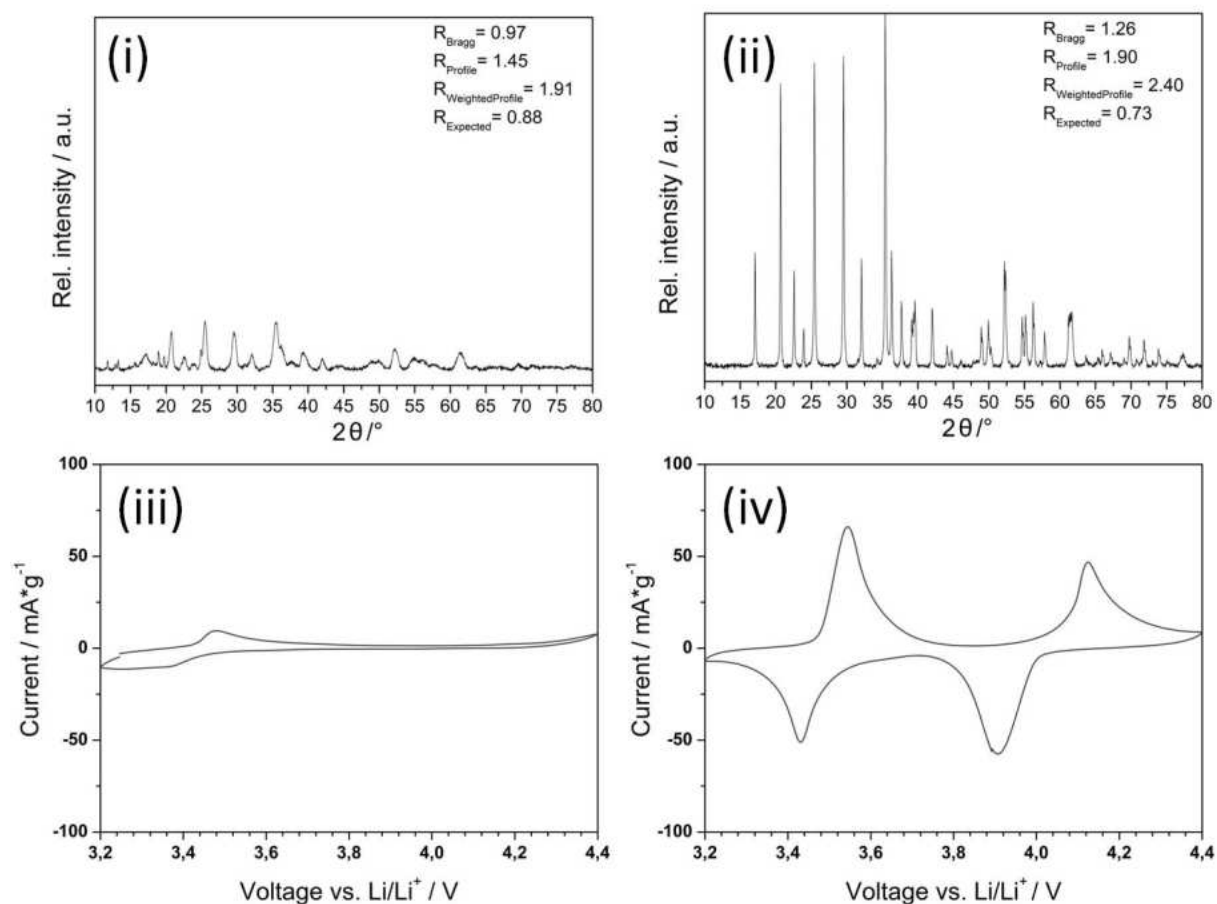


Figure 30: XRD patterns and corresponding 2nd cycle of the CV of $\text{LiFe}_{0.5}\text{Mn}_{0.5}\text{PO}_4$ (i) + (iii) after microwave solvothermal synthesis and (ii) + (iv) after the post-annealing step with sucrose as carbon source.

Carbon content. As mentioned in chapter 4.1.1, the microwave solvothermal synthesis was previously performed according to section 3.1.1, whereas the ball milling step occurred with 20 wt% Super P rather than sucrose. Since the slurry composition is the same (cf. Table 10) and no further decomposition of the Super P occurs during the oven treatment, resulting carbon concentration of the powders is rather high. This carbon content results in a decrease in gravimetric energy density as well as tap density of the sample. As shown in Figure 31, the electrochemical performance of the samples is not good either. LFP and LFMP reach a practical discharge capacity of 120 and 86 mAh g^{-1} , respectively (80 wt% of active material after the post-annealing step within the composite electrode is used for calculation).

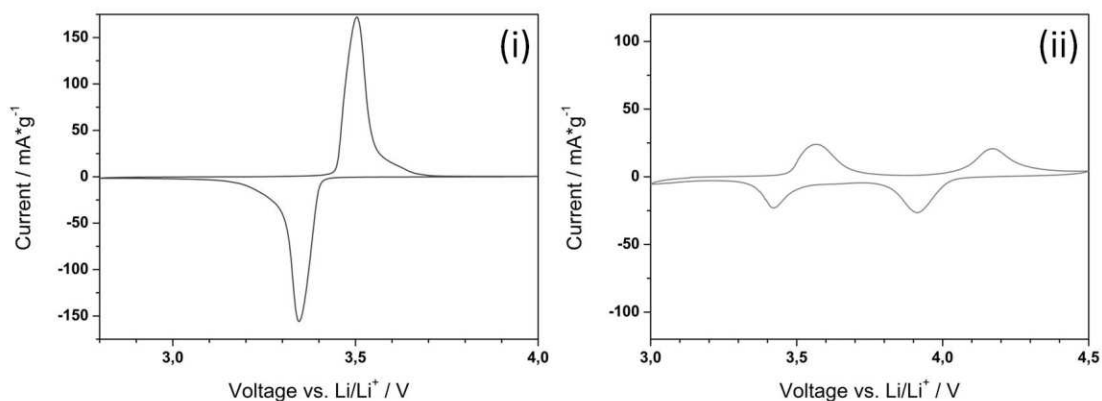


Figure 31: 3rd cycle of the CV of (i) LiFePO_4/C and (ii) $\text{LiFe}_{0.5}\text{Mn}_{0.5}\text{PO}_4/\text{C}$ with Super P as carbon source.

According to literature [161][164][165], carbon coatings from sucrose lead to good electrochemical performances of phospho-olivines. Therefore, instead of adding 20 wt% Super P, 20 wt% sucrose is added to the powders before the ball milling step. This leads to an improvement in the electrochemical performance and quite good capacities with less carbon content in the final composite electrode. Elemental analysis is used to analyze the carbon content of the samples and results in 5-8 wt% per sample. Electrochemical results are shown in chapter 4.1.2.2.

Particle size. Figure 32 clearly illustrates that the synthesized particles after the oven form agglomerates of a few micrometers in size. The 10 kx magnification demonstrates the surface of the agglomerates. It is obvious that the agglomerates consist of nanometer sized particles.

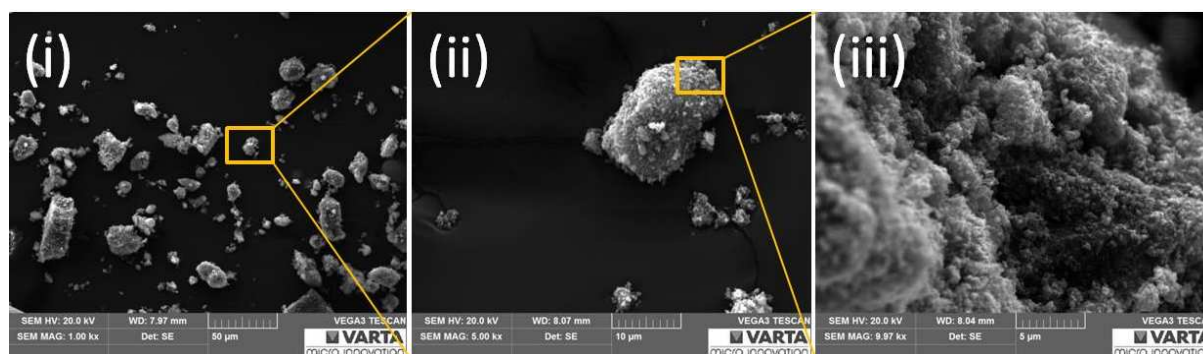


Figure 32: SEM images of $\text{LiFe}_{0.5}\text{Mn}_{0.5}\text{PO}_4/\text{C}$ with (i) 1 kx, (ii) 5 kx and (iii) 10 kx magnification.

It is well known [62][70] that nanometer-sized phospho-olivines perform electrochemically very well. Therefore, ball milling of these powders in NMP is used to downsize these agglomerates. Table 17 summarizes some results obtained by Fritsch Analysette 22 NanoTec Plus. Tensides are added to reduce the surface tension of the samples. Although all samples were dispersed by ultrasonic waves, agglomerates of the nanometer-sized particles still remain. The results, obtained by the application of Fraunhofer theory, are determined as particle volumes ($Q_3(x)$) of the sample. The values reveal that a downsizing of the agglomerates by ball milling is basically possible. Anyway, a dependence of particle size neither on grinding time nor on the size of the grinding balls can be ascertained.

Table 17: Parameters and resulting particle sizes for $\text{LiFe}_{0.5}\text{Mn}_{0.5}\text{PO}_4/\text{C}$ grinded in NMP.

\varnothing TC / mm	Speed / rpm	Time / h	Q3(x) / μm , $\leq 50\%$	Q3(x) / μm , $\leq 90\%$
-	-	-	6.36	26.29
3	900	3.5	3.16	14.42
3	900	4	4.37	10.24
0.6	900	7	1.99	10.44
0.6	900	8	4.35	11.17

Even though particle sizes are diminished by grinding the powders after the oven treatment, Figure 33 shows that the capability of lithium-ion insertion and deinsertion of the material is impossible. Therefore, the grinding procedure annihilates the particles, in particular their carbon coating. Hence, ball milling experiments are solely performed before the post-annealing step. Good electrochemical characteristics are obtained if the powders are mixed with sucrose and NMP for half an hour at 300 rpm in the ball mill only before the oven treatment (cf. Figure 33 (ii)). If another ball milling step occurs after the oven treatment, the ability of reversible insertion/deinsertion of lithium-ions is lost. Henceforth, the ball milling step only occurs before the oven treatment within the standard synthesis procedure of all powders.

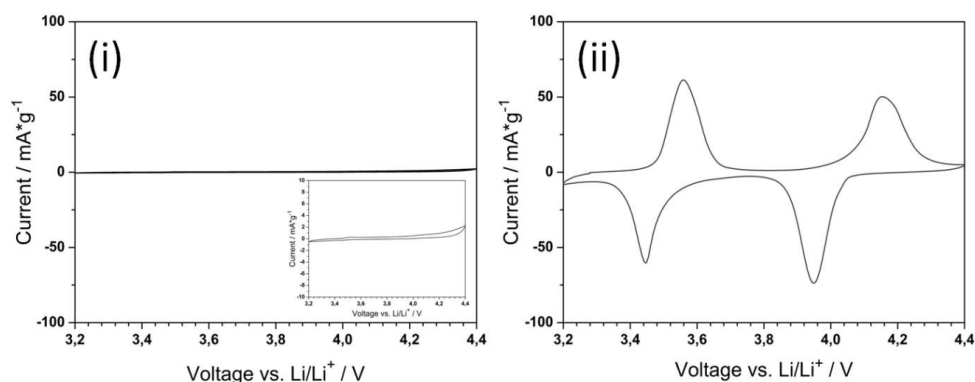


Figure 33: 2nd cycle of the CVs of $\text{LiFe}_{0.5}\text{Mn}_{0.5}\text{PO}_4/\text{C}$. (i) After the oven treatment and subsequent ball milling with a diagram at the bottom that shows a magnified view of the y-axis. (ii) After the oven treatment without further ball milling.

pH adjustment. Especially for iron, the value for the redox potential between Fe^{2+} and Fe^{3+} is dependent on the pH-value [166]. Therefore, it is necessary to adjust the pH during microwave synthesis to obtain phase pure powders without any contaminations of Fe(III) species. Among pH-values in the range of 6 to 9, especially between 6.0 and 7.5, the synthesized powders show superior performance with regard to their electrochemical behavior. Therefore, all materials are prepared by applying this particular pH range.

Concentration adjustment. The dependence of precursor concentrations in tetraethylene glycol (TEG) on electrochemical performance is determined as well. Hence, three different concentrations between 0.10 and 0.14 M are examined. Below 0.10 M TEG does not solve the educts sufficiently

enough. Above a precursor concentration of 0.14 M, a gel-like solution formed when $\text{LiOH}\cdot\text{H}_2\text{O}$ was added. Therefore, the upper concentration limit is set to 0.14 M, since no uniform distribution of iron, manganese, lithium and phosphorus through insufficient magnetic stirring among microwave solvothermal synthesis occurs otherwise. Among them, CV and CC measurements are best when a precursor concentration of 0.14 M is used. Hence, all precursors applied in microwave solvothermal synthesis are 0.14 M regarding their educts dissolved in TEG.

4.1.2.2 Structural chemistry and electrochemical behavior of $\text{LiFe}_x\text{Mn}_{1-x}\text{PO}_4/\text{C}$ ($x = 0, 0.1, \dots, 1$)

Structural characterization. The XRD analysis of the obtained powders by solvothermal microwave synthesis confirms the olivine phase and is indexed as orthorhombic Pmnb space group. As illustrated in Figure 34 (i) and (ii), all olivines exhibit a similar diffraction pattern. Only sample I and sample G show some minor impurities between 30 and 32° . According to the XRD diagrams measured by Andersson et al. [163] and Lee et al. [162], these impurities may correlate with heterosite species $\text{Fe}_x\text{Mn}_{1-x}\text{PO}_4$. Anyway, peak intensities of the powders coincide very well with the ICSD reference XRD patterns (cf. Table 18).

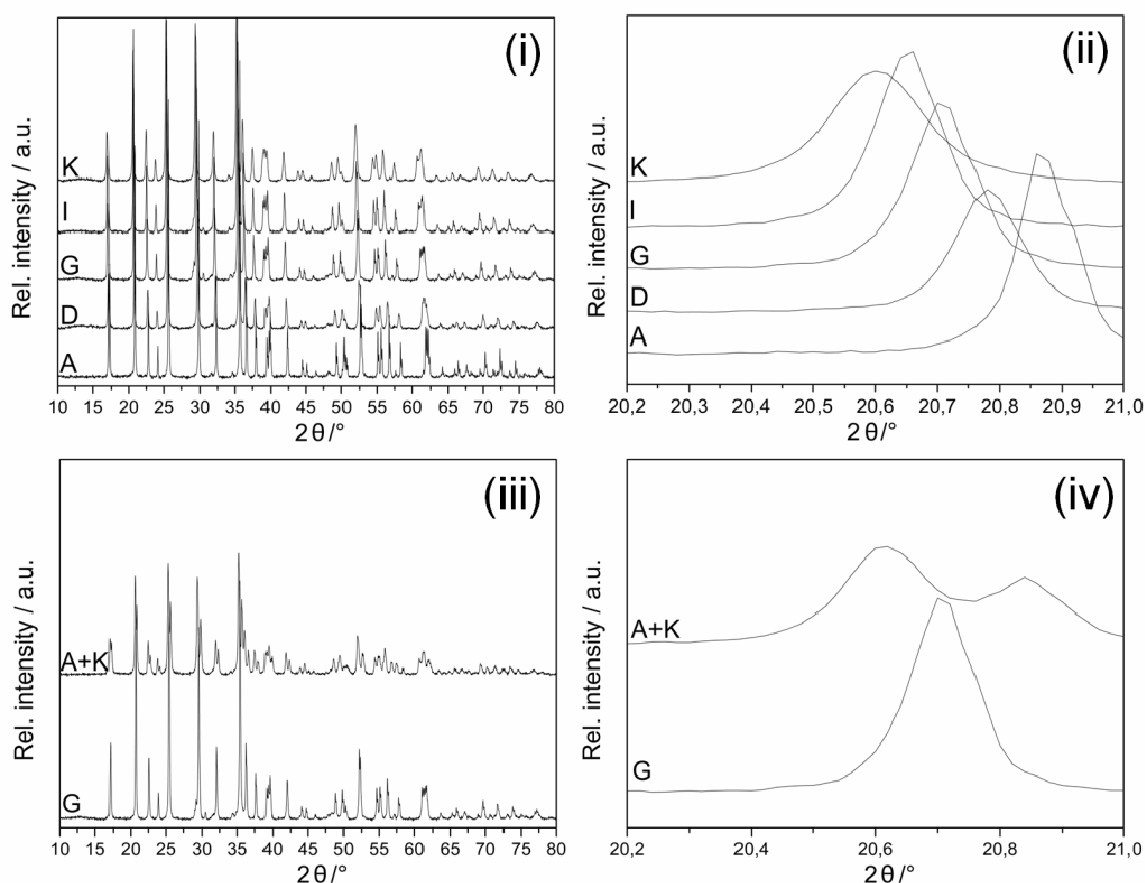


Figure 34: (i) XRD patterns of sample A, sample D, sample G, sample I and sample K. (ii) Magnified view of 20.2 - 21.0° 2θ of the aforementioned species. (iii) Comparison of sample G and of a manual mixture of 0.4 eq. sample A and 0.6 eq. sample K and their (iv) magnified view between 20.2 - 21.0° 2θ .

Table 18: Disagreement indices of the Rietveld refinement for sample A to sample K.

Sample	R _{Profile}	R _{Weighted Profile}	R _{Bragg}	R _{Expected}
A	2.19	3.07	2.61	0.64
B	2.14	2.93	1.63	0.65
C	1.86	2.42	1.12	0.66
D	2.13	2.93	1.66	0.65
E	2.19	2.75	1.11	0.69
F	1.90	2.40	1.26	0.73
G	2.49	3.13	1.26	0.74
H	2.44	3.03	1.10	0.75
I	2.78	3.47	1.33	0.79
J	2.72	3.40	1.44	0.81
K	3.28	4.08	1.69	0.84

The slight shift of peak intensities is influenced by the kind of atoms and their arrangement in the unit cell. A shift in peak position is observed, if the Mn-content in $\text{LiFe}_x\text{Mn}_{1-x}\text{PO}_4/\text{C}$ is increased meaning higher Mn-contents result in a shift to a lower angle and an increase in the atomic lattice (d-spacing) since its ion radius is bigger compared to Fe^{2+} . A linear increase in lattice parameters a, b, c and cell volume occurs. This increase is summarized in Table 19.

Table 19: Lattice parameters (a, b, c and cell volume) for samples A-K. The standard deviation of the lattice constants is shown in brackets.

Sample	a / Å	b / Å	c / Å	Volume / Å ³
A	10.3211(7)	6.0039(4)	4.6941(4)	290.88
B	10.3343(5)	6.0136(3)	4.6997(3)	292.07
C	10.3491(3)	6.0242(2)	4.7047(2)	293.31
D	10.3600(3)	6.0333(2)	4.7125(2)	294.55
E	10.3778(2)	6.0441(1)	4.7149(1)	295.74
F	10.3890(1)	6.0536(1)	4.7191(1)	296.79
G	10.4008(3)	6.0631(1)	4.7256(1)	298.00
H	10.4134(2)	6.0735(1)	4.7309(1)	299.21
I	10.4250(2)	6.0836(1)	4.7369(1)	300.42
J	10.4355(3)	6.0933(2)	4.7442(2)	301.67
K	10.4495(3)	6.1032(2)	4.7485(2)	302.84

To confirm the formation of a solid solution by microwave solvothermal synthesis accompanied by a post-annealing step, the diffraction pattern of microwave synthesized sample G is compared to a manual mixture of 0.4 eq. of sample A with 0.6 eq. of sample K. Figure 34 (iii and iv) definitely

demonstrates the difference between the two preparation methods. Whereas microwave synthesized samples only show one peak at certain peak positions, the manually mixed sample shows a splitting of the peaks due to two different lattice parameters of the active material A and active material K. Therefore, XRD analysis suggests the formation of solid solutions by microwave solvothermal synthesis, in which manganese-ions occupy the interstitial sites of sample A and vice versa.

SEM images demonstrate that as synthesized particles are a few nanometers in size. Moreover, the particles are highly agglomerated (cf. Figure 35) and differ in size and shape. Due to the decomposition of sucrose, particles are well embedded in carbon.

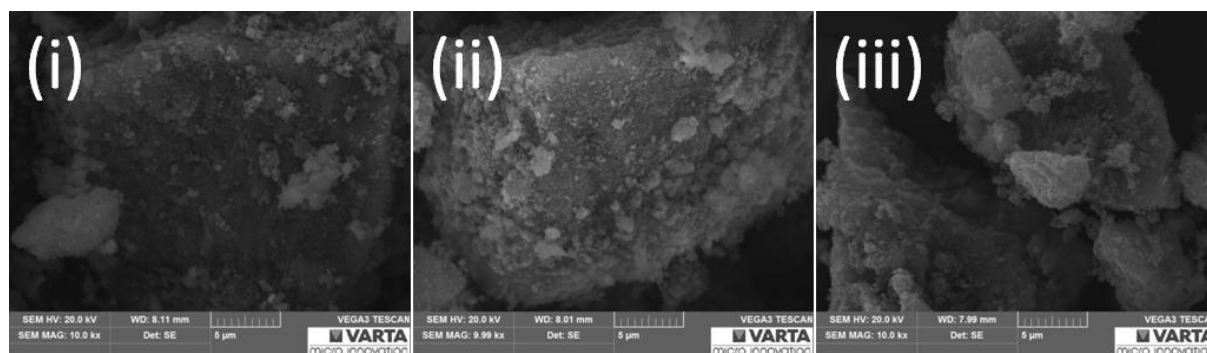


Figure 35: SEM images of (i) sample C, (ii) sample H and (iii) sample K with 10 kx magnification.

Electrochemical tests. As illustrated by Martha et al. [167], in case of active material I, cation segregation occurs in all of the synthesized multi-transition metal phospho-olivines (cf. Figure 36). Two distinct redox couples are observed at ~ 3.4 - 3.5 V vs. Li/Li^+ and ~ 3.9 V vs. Li/Li^+ for the reduction of Fe^{3+} and Mn^{3+} , respectively. The formation of a solid solution between sample A and sample K has an influence on the position of the redox couples (cf. Table 20). The higher the iron content, the lower is the position of the oxidation and reduction potential of $\text{Fe}^{3+}/\text{Fe}^{2+}$ redox couple.

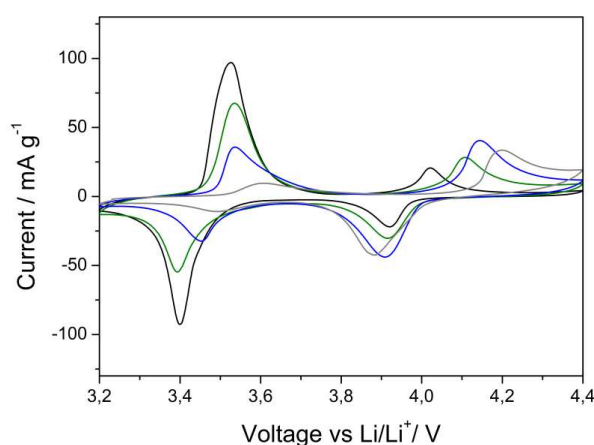


Figure 36: 2nd cycle of the cyclic voltammetric measurements of electrode C (black), electrode E (green), electrode G (blue) and electrode I (grey) at a scan rate of $30 \mu\text{V s}^{-1}$ at 25°C .

Table 20: Maximum oxidation and reduction peaks vs. Li/Li⁺ for the electrodes C, E, G and I.

	Fe ²⁺ →Fe ³⁺ / V	Fe ³⁺ →Fe ²⁺ / V	Mn ²⁺ →Mn ³⁺ / V	Mn ³⁺ →Mn ²⁺ / V
Electrode C	3.53	3.40	4.02	3.92
Electrode E	3.54	3.39	4.11	3.92
Electrode G	3.54	3.45	4.14	3.91
Electrode I	3.61	3.49	4.20	3.88

Generally, LiFePO₄/C exhibits higher electron transfer kinetics and a lower charge transfer resistance compared to LiMnPO₄/C. Therefore, the peak potential separation of the Fe³⁺/Fe²⁺ redox couple is minor compared to that of Mn²⁺/Mn³⁺. An excess of manganese in the lattice induces a shift to higher oxidation potentials of Mn²⁺ and lower reduction potentials of Mn³⁺ in LiFe_xMn_{1-x}PO₄/C. The peak potential separation for the Mn²⁺/Mn³⁺ redox reaction is primarily influenced by the anodic reaction. The obtained results are consistent with Muraliganth et al. [81]. Since the phosphate group is fixed in the olivine structure, the insertion of counter cations definitely causes the shift in redox potentials. In theory, the position of the oxidation and reduction reaction in the CV depends both on the electronegativity and the ionic radii of the cations. The two phenomena have a converse effect on the peak positions. However, since iron and manganese exhibit a similar electronegativity, the influence of the ionic radii of the cations predominates. As a matter of fact, the higher manganese content in LiFe_xMn_{1-x}PO₄/C affects the lattice parameters and Mn-O bond lengths are increased. This decrease in covalence of the latter causes a shift in the redox-potential during lithium insertion/extraction that can be observed in the CVs.

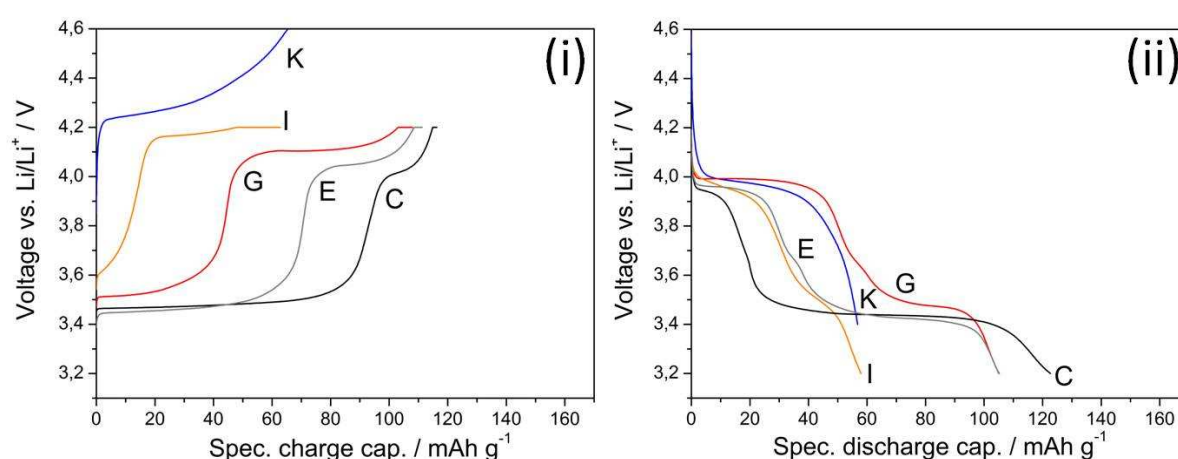


Figure 37: (i) CC charge profiles and (ii) CC discharge profiles of electrode K (blue), electrode I (orange), electrode G (red), electrode E (grey) and electrode C (black) displaying the 1st cycle at 0.1 C and 25 °C for each material.

After cyclic voltammetry, the same cells are treated with the aforementioned CCCV program. Figure 37 shows the resulting CC profiles for the first cycles of electrode C, E, G, I and K. The materials

exhibit a flat voltage profile with one or two plateau regions. The first plateau at around 4.0 V vs. Li/Li⁺ and the second plateau at around 3.5 V vs. Li/Li⁺ belongs to Mn³⁺/Mn²⁺ and Fe³⁺/Fe²⁺ redox couple, respectively. The coexistence of Mn and Fe in the olivine enhances the CC discharge capacity compared to sample K. A general trend of a higher capacity can be supposed when the iron content is increased in the sample. If iron is reduced to 0.2 eq. in the structure, the capacity drops dramatically. The ex-situ carbon coating from sucrose and post-annealing step at 700 °C under inert atmosphere further enhances electronic and ionic conductivity. Microwave synthesized active material C exhibits an initial discharge capacity of 123 mAh g⁻¹ at 0.1 C and 25 °C whereas electrode I shows only 58 mAh g⁻¹.

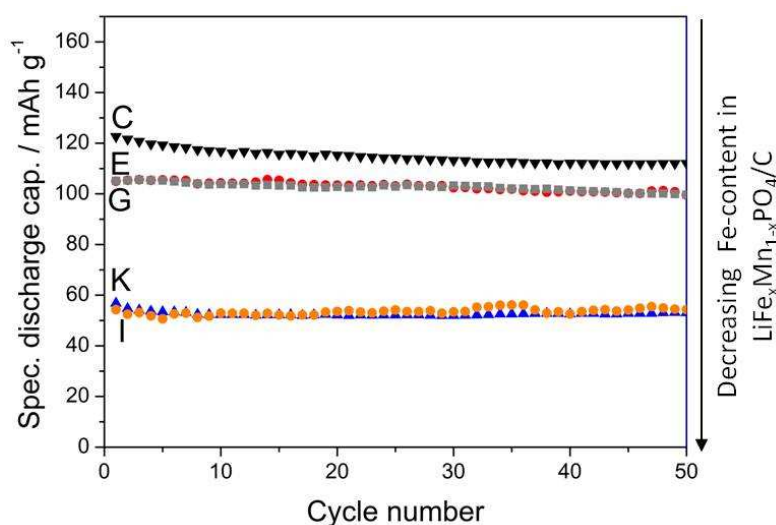


Figure 38: Specific discharge capacity vs. cycle number at 25 °C with a C-rate of 0.1 C of electrode K (blue), electrode I (orange), electrode G (red), electrode E (grey) and electrode C (black).

All samples show good stability upon cycling and only a slight capacity fading with ongoing cycling. The capacity retention after the CCCV program is 91 %, 95 %, 95 %, 100 % and 93 % for electrode C, E, G, I and K, respectively. Sample E and sample G show a similar behavior upon cycling regarding their capacity retention and specific discharge capacities. The experimental specific energy density is highest for sample C and lowest for sample K (cf. Table 21). This result disagrees from the theoretically calculated energy density values since manganese worsens the electronic conductivity of the samples. In contrast to the linear dependence between the theoretical energy density values and the transition metal concentration, no such correlation can be specified for the experimental energy densities. The reason for this might be the different particle sizes of the agglomerates.

Table 21: Energy densities of the active materials corresponding to Figure 38.

	Energy density / Wh kg ⁻¹ Theoretical	Energy density / Wh kg ⁻¹ For the 1 st discharge cycle	Energy density / Wh kg ⁻¹ For the 50 th discharge cycle
Electrode C	609	429	393
Electrode E	631	377	359
Electrode G	653	391	370
Electrode K	675	203	204
Electrode I	697	222	210

After these cycling experiments, the lithium metal electrode is analyzed in terms of manganese dissolution. The final manganese content on the negative electrode is $0.054 \pm 0.04 \text{ mg L}^{-1}$ and $0.72 \pm 0.18 \text{ mg L}^{-1}$ for sample C and sample K, respectively. Hence, the increase of 0.8 eq. of manganese within the solid solution for sample K leads to a 14-fold increase of detectable manganese on the anode. Consequently, the higher the manganese content in the sample, the more severe the manganese dissolution will be. Note that the improper detachment of the separator from the sample might be the reason for the high standard deviation since manganese can be contained within the separator as well. To avoid the sticking of the non-woven fabric mat to the lithium metal, future cell assemblies for manganese quantification purposes should be carried out with a microporous polymer separator (e.g. from Celgard).

The electric conductivity is measured by four point resistivity measurements. A current of $100 \mu\text{A}$ is applied to the metal tips and the corresponding voltage is determined. The electrical resistance and electric conductivity is calculated according to eq. 28 and eq. 29.

$$\delta = \frac{U \times A}{i \times L} \quad \text{eq. 28}$$

$$\sigma = \frac{1}{\delta} \quad \text{eq. 29}$$

δ Specific, electrical resistance / $\Omega \text{ m}$
 U Voltage / V
 A Cross sectional area / m^2
 i Current / A
 L Distance between two measurement points / m
 σ Electrical conductivity / S m^{-1}

Nevertheless, no significant trend in electric conductivity is obvious and all values are of the same order of magnitude.

To gain insight into the lithium-ion diffusivity as well as into the internal resistance of the solid solutions, GITT measurements are recorded for sample C and I. Figure 39 illustrates the measurement principle. The thermodynamic equilibrium of the electrode is disturbed by a short current load until $t_0 + \tau$ is reached. During the raise of the voltage, overpotential phenomena that are characteristic for the electrode occur (cf. chapter 2.1.2). Afterwards, the relaxation back to the thermodynamic equilibrium condition is recorded under no load conditions.

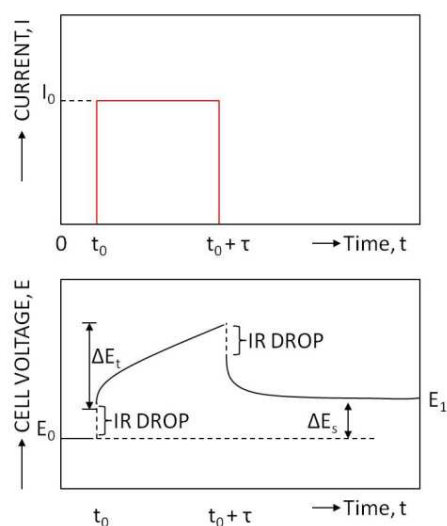


Figure 39: Scheme of GITT measurements. ΔE_t signifies the change of transient voltage whereas ΔE_s describes the total change of steady state voltage after the current pulse. Redrawn from [168].

This relaxation corresponds to the lithium-ion diffusivity rate within the material. As shown in Figure 40, the iron in electrode C relaxes faster than the manganese upon delithiation. Therefore, the kinetics of lithium insertion and deinsertion into the LFP particles proceed at a higher velocity. The GITT of electrode I clearly demonstrates that the higher the delithiation is, the lower the lithium-ion diffusivity of the sample will be. Therefore, a higher electrode resistance occurs if lithium is deinserted from LMP compared to LFP. Further, among lithiation, the resistance increases as the voltage decreases. Considering the shrinking core model, it is evident that the internal resistance grows among insertion of lithium-ions into FePO_4 since lithium-ions need time to diffuse into the core of the particles. Therefore, lithiation of the shell occurs fast whereas the whole nucleation of the particle proceeds slower. In contrast, the cascade model describes the development of lithium-poor and lithium-rich domains among lithiation. Since the material is only able to reinsert a certain amount of lithium-ions, the lithium-ion mobility decreases when both domains have developed. The insertion of a higher concentration of lithium-ions into the lithium-poor domains results in an increase in the internal resistance of the sample.

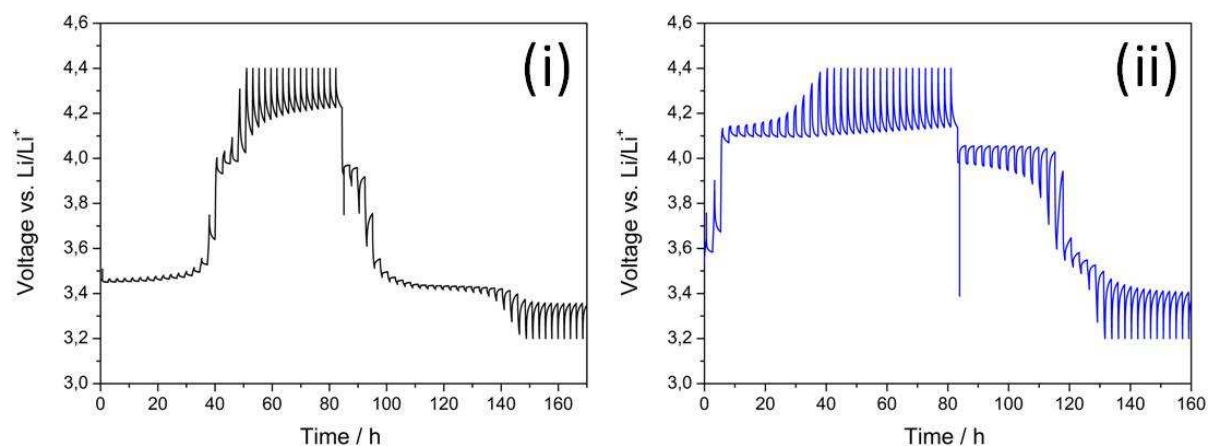


Figure 40: GITT measurement of (i) electrode C and (ii) electrode I.

Figure 41 compares typical relaxation profiles for the $\text{Fe}^{2+}/\text{Fe}^{3+}$ and $\text{Mn}^{2+}/\text{Mn}^{3+}$ redox couple of electrode C. It is obvious that the $\text{Mn}^{2+}/\text{Mn}^{3+}$ redox couple exhibits a higher IR drop and slower relaxation compared to the $\text{Fe}^{2+}/\text{Fe}^{3+}$ redox couple. The IR drop corresponds to a drop in voltage evoked by the resistance of a sample. For GITT measurements, the IR drop is a time-independent constant [168]. Hence, the worse electrochemical performance if the manganese content in the solid solution is high can be explained through the higher internal resistance of the electrode.

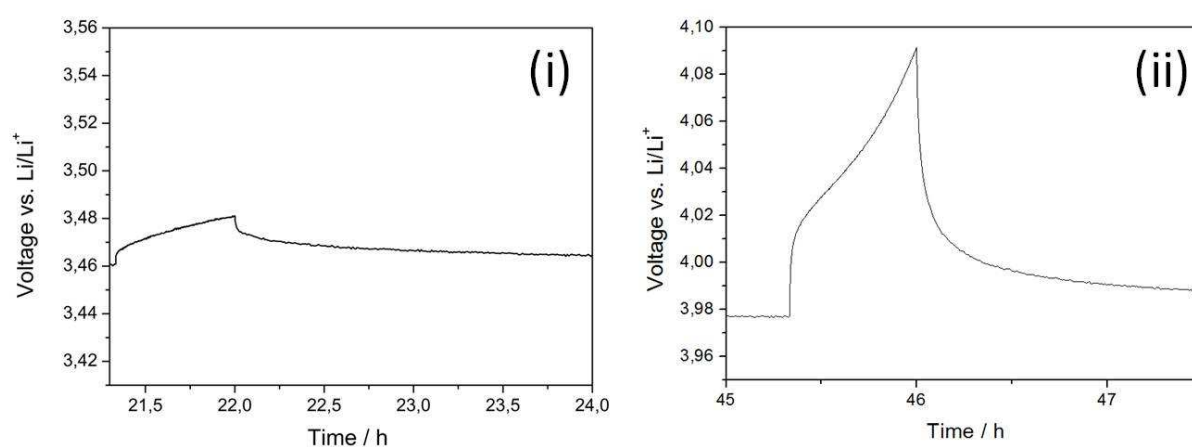


Figure 41: Difference in relaxation for electrode C of (i) $\text{Fe}^{2+}/\text{Fe}^{3+}$ redox couple and (ii) $\text{Mn}^{2+}/\text{Mn}^{3+}$ redox couple.

Anyway, the higher manganese content might lead to an increase in energy density of the sample. For instance, electrode G shows in comparison to electrode E an increase in its gravimetric energy density of 3.1 %. Moreover, electrode F (cf. chapter 4.1.2.3) exhibits a remarkable gravimetric energy density of 512 Wh kg^{-1} referring to the active material compared to sample G, which corresponds to an increase of the energy density by 22.5 %. The equimolar mixture of iron and manganese seems particularly favorable in terms of electrochemical properties. Therefore, sample F is chosen as benchmark for further characterizations and preparation methods, as will be discussed in the next chapter.

4.1.2.3 Preparation details with focus on the solid solution formation determining step

To determine the essential step for the solid solution formation, the equimolar compound $\text{LiFe}_{0.5}\text{Mn}_{0.5}\text{PO}_4/\text{C}$ (sample F) was not only prepared directly in the microwave oven, but also by ball milling or manual mixing procedures. The resulting sample L is prepared by ball mill mixing of the appropriate amount of sample A and K together with sucrose. Sample M is made by separate ball mill mixing of active material A or K with sucrose and afterwards equimolar amounts of active material A and K are mixed in an agate mortar. Finally, sample L and sample M are post-annealed as mentioned before. The difference in the preparation methods for sample F, L and M is illustrated in Figure 42.

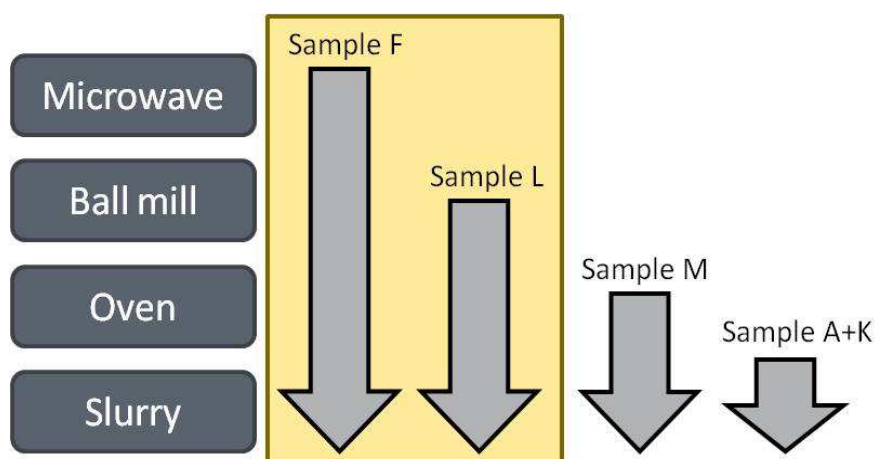


Figure 42: Schematic illustration of the different preparation methods. The framed area signifies that a solid solution is formed for $\text{LiFe}_{0.5}\text{Mn}_{0.5}\text{PO}_4/\text{C}$.

Structural Characterization. As shown in Figure 43, the only difference in crystal structure is a slight shift to lower angles for sample F compared to sample L. The appearance of the peaks is similar for both samples. On the contrary, the peak shape of sample M is clearly distinct from that of sample L and sample F. Since iron and manganese exhibit a similar X-ray diffraction due to their almost same crystal lattice, the signals of the LiFePO_4/C and LiMnPO_4/C are overlapping in the diffraction pattern of sample M. Therefore, in the case of active material L, it is demonstrated that the formation of a solid solution occurs by mechanical mixing of sample A and K together in the ball mill and with the subsequent annealing step at 700 °C.

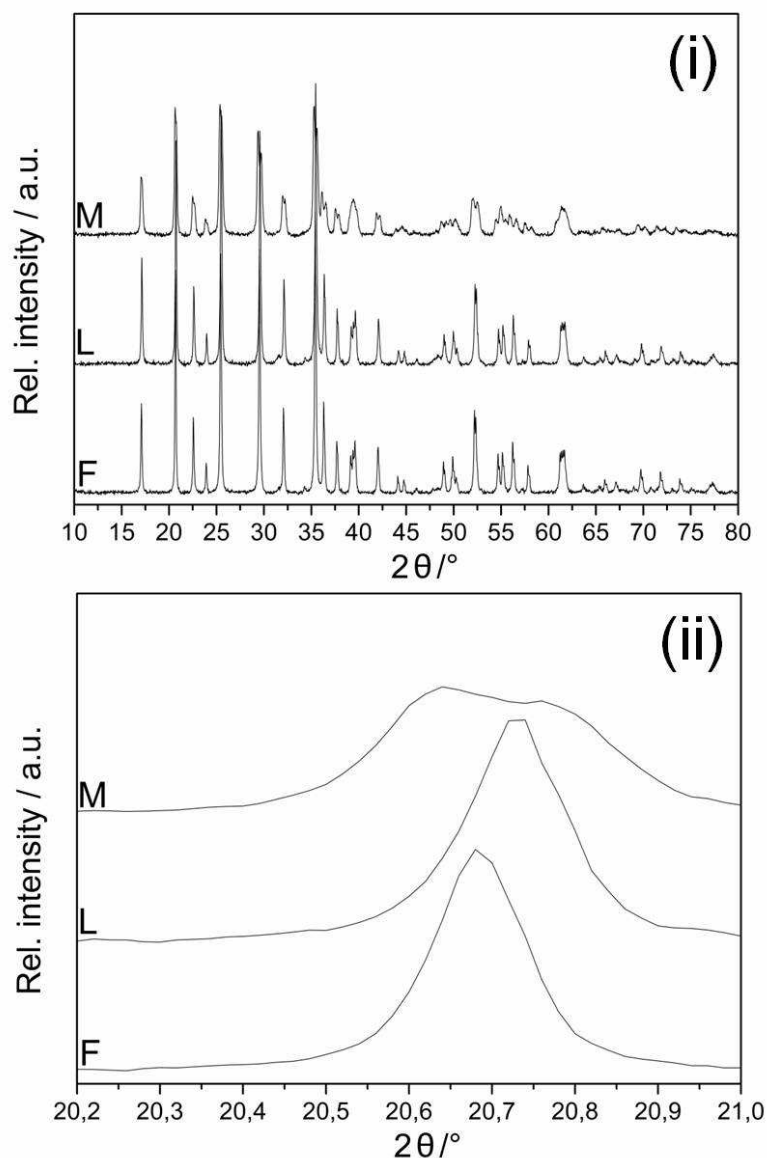


Figure 43: (i) XRD patterns of sample F, sample L and sample M. (ii) Magnified view of 20.2-21.0° 2θ of the aforementioned species.

SEM-BSE images (cf. Figure 44) of the prepared electrodes on aluminum current collectors reveal that casted electrode films are non-uniform regarding the particle size and morphology of the positive electrode material. No difference between both preparation methods is obvious. Nanoscale particles agglomerate to distinct particles up to several microns in size. The edge of the agglomerates is partly covered by denser packed particles. According to XRD analysis and elemental mapping, iron and manganese are evenly distributed among the agglomerates. The active material is well embedded in carbon. Considering the two different preparation methods, neither difference in morphology nor in particle distribution and size is obvious. The red marks in Figure 44 highlight white particles, which correspond to tungsten carbide (TC). That means some abrasion occurs during the ball milling step. Nevertheless, TC remains inert during the electrochemical experiments.

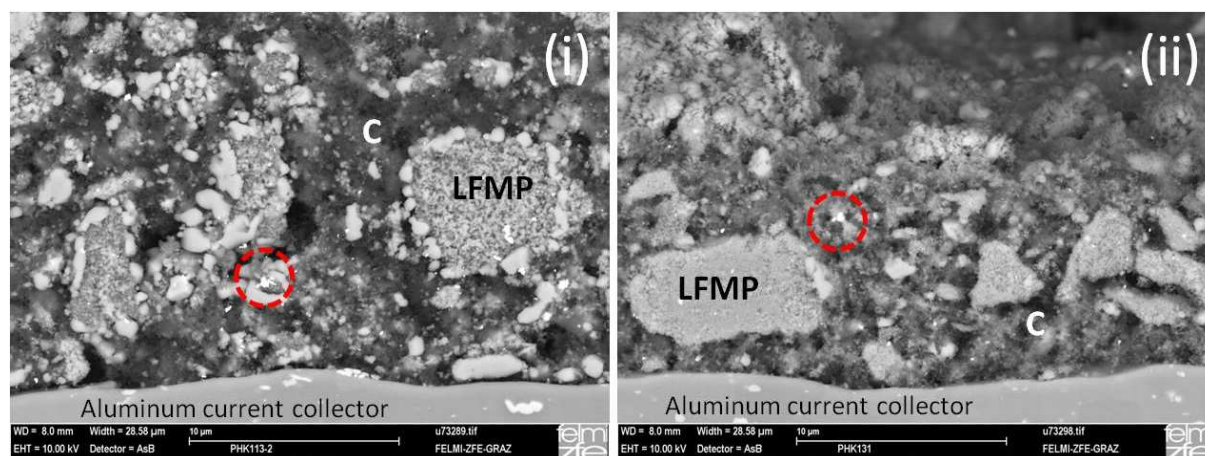


Figure 44: SEM-BSE images of the slope cuts of (i) electrode F and (ii) electrode L.

Whereas a solid solution is formed for sample F and L, the post-annealing step at 700 °C of the manual mixture of 0.5 eq. sample A with 0.5 eq. sample K and sucrose in an agate mortar does not result in the formation of a solid solution. This difference is also evident in Table 22 and will be discussed later.

Table 22: Comparison of the lattice parameters of samples F, L and M with the standard deviations in brackets.

	a / Å	b / Å	c / Å	Volume / Å ³
Sample F	10.3890(1)	6.0536(1)	4.7191(1)	296.79
Sample L	10.3832(3)	6.0493(2)	4.7185(2)	296.37
Sample M	10.3967(2)	6.0734(1)	4.7280(1)	298.54

Electrochemical tests. As mentioned above, two distinct redox couples are apparent in the cyclic voltammetric chromatograms for sample F, L and M. CC charge and discharge profiles for the first cycle of the three different materials are shown in Figure 45. The specific discharge capacity of sample K is remarkably increased by the formation of the solid solution with Fe in sample F and L, no matter if the particles are synthesized directly through microwave irradiation of both $\text{Fe}(\text{CH}_3\text{COO})_2$ and $\text{Mn}(\text{CH}_3\text{COO})_2 \cdot 4\text{H}_2\text{O}$ or through ball-mill mixing of sample A and sample K. Regarding the microwave synthesizing method, the slightly higher values for the lattice parameters a, b, c and the total cell volume might cause a superior capacity compared to the mechanically mixed powder (cf. Table 22). Sample M exhibits even higher values for a, b, c and the cell volume, respectively. Since sample M is no solid solution, a mixture of the unit cells for LMP and LFP occurs, leading most probably to this increase in lattice parameters.

The superior mixing during the microwave synthesis in solution might lead to a more even distribution of manganese and iron within the lattice, causing a lower charge transfer resistance for sample F. Active material F, L and M exhibit an initial discharge capacity of 139 mAh g^{-1} , 127 mAh g^{-1} and 91 mAh g^{-1} , respectively.

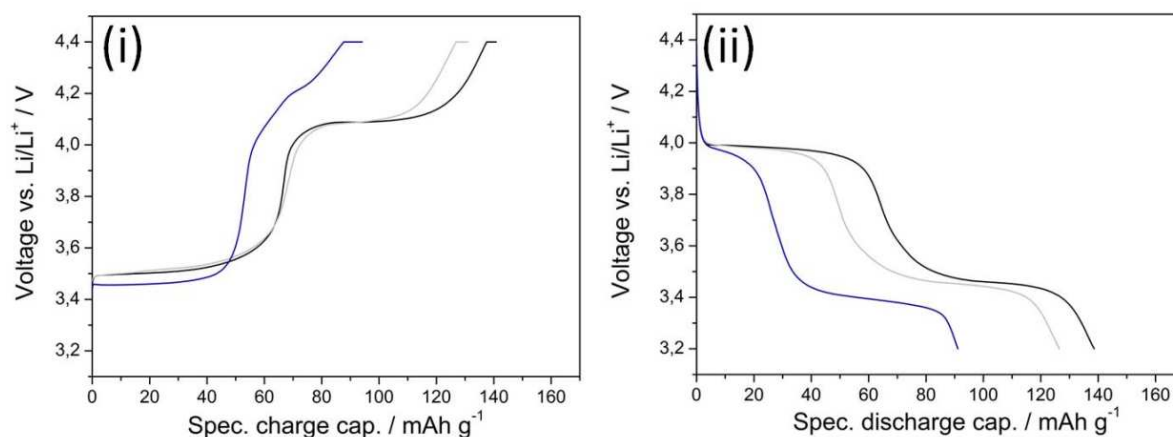


Figure 45: (i) CC charge profiles and (ii) CC discharge profiles for electrode F (black), electrode L (grey) and electrode M (blue). For each material the 1st cycle at 0.1 C and 25 °C is shown.

Figure 46 displays the development of the specific discharge capacities among 50 CC cycles and the rate capability tests of the three different materials. The materials are stable upon cycling, showing 97 % for sample F, 99 % for sample L and 100 % for sample M of their initial discharge capacity after 50 CC charge/discharge cycles. Since the capacity for the samples after their exposure to higher current densities is approximately the same, the materials are stable to higher C-rates. Anyway, the higher C-rates diminish the capacities of the samples. Whereas at 0.5 C the specific discharge capacities are 126, 110 and 81 mAh g⁻¹ for electrode F, L and M, they decrease at 1 C to 115, 106 and 69 mAh g⁻¹, respectively.

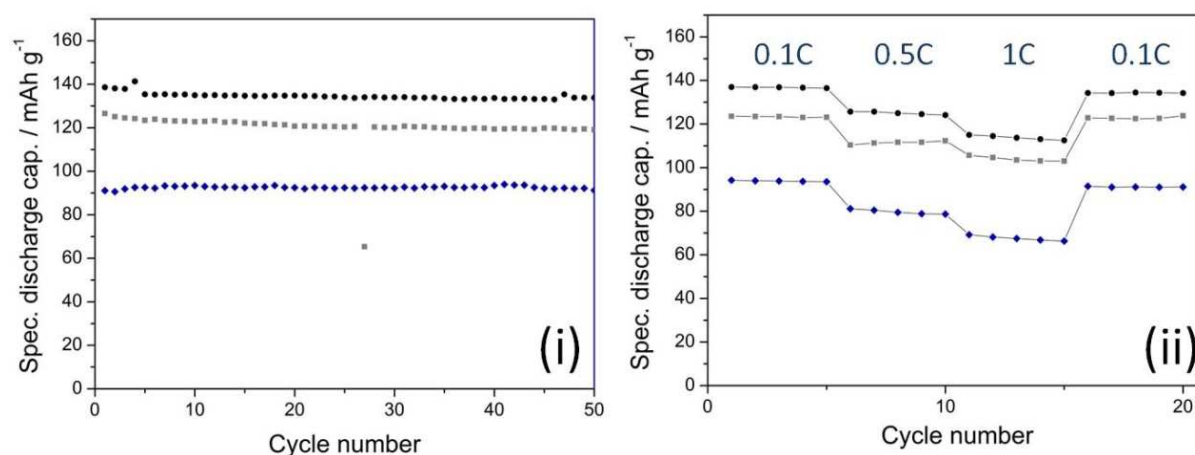


Figure 46: (i) Specific discharge capacities vs. cycle number at 25 °C with a C-rate of 0.1 and (ii) rate capability tests for electrode F (black), electrode L (grey) and electrode M (blue).

According to Figure 47, two distinct voltage plateaus are visible for all materials at a C-rate of 0.1 C. By increasing the CC charge/discharge rate, the second plateau slightly disappears for sample F, whereas the first plateau disappears for sample M. Regarding sample F, the second fading plateau (Fe²⁺/Fe³⁺) might result from the formation of a solid solution with particles that show diverse kinetics upon lithium insertion/deinsertion. On the contrary, the individual particles of LMP and LFP

for sample M behave different when the charge densities are increased. Therefore, at higher C-rates, active material L suffers from lower overpotentials compared to active material F and M, which results in higher discharge potentials for both, the delithiation of LMP and LFP. Hence, sample L seems to be kinetically favored, even though the overall achievable capacity is higher for sample F in all experiments.

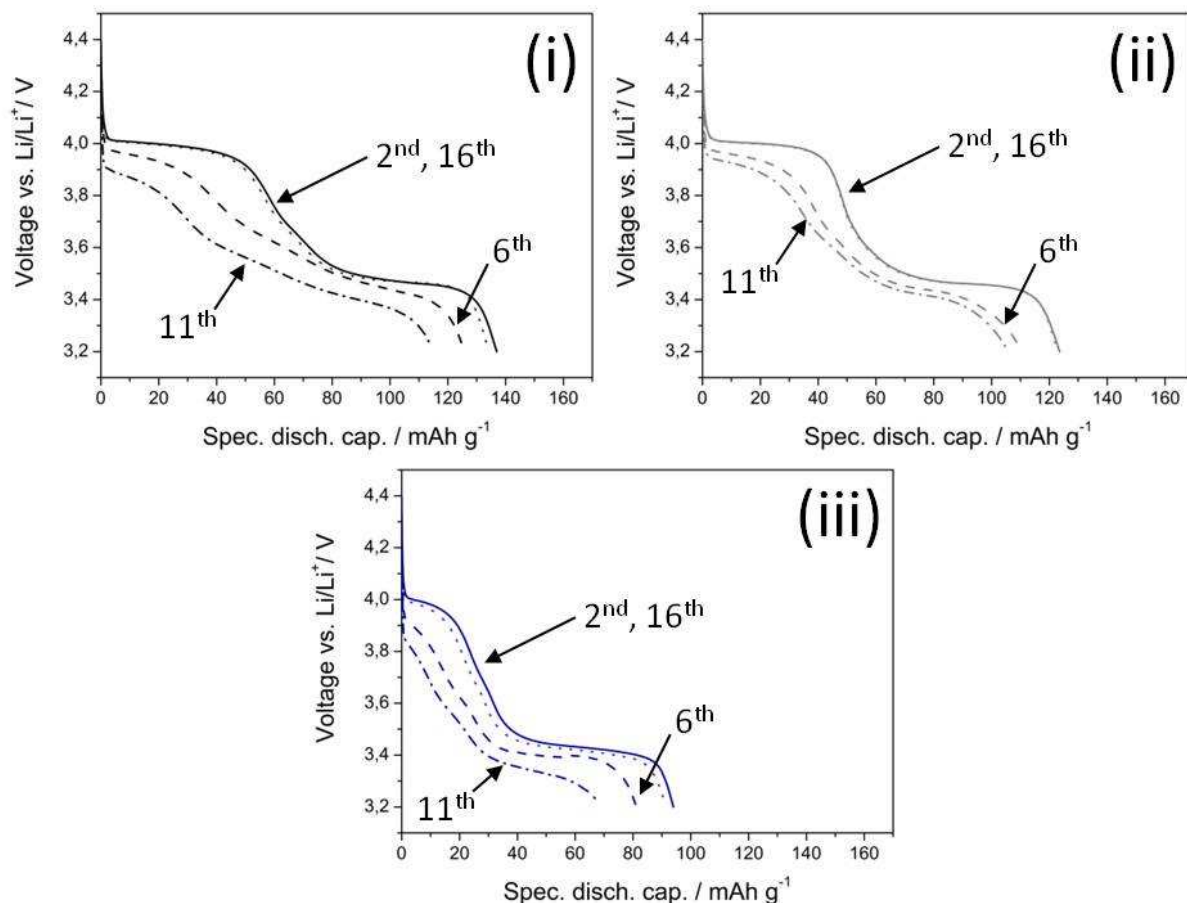


Figure 47: Discharge profiles of (i) sample F (black), (ii) sample L (grey) and (iii) sample M (blue). The 2nd, 6th, 11th and 16th cycle corresponding to Figure 46 (ii) are shown.

It is evident that the formation of solid solutions $\text{LiFe}_x\text{Mn}_{1-x}\text{PO}_4/\text{C}$ leads to superior electrochemical behavior compared to sample M and poorly-conducting sample K.

4.1.2.4 Isovalent doping of equimolar $\text{LiFeMnPO}_4/\text{C}$

The aliovalent doping with 0.01 eq. and 0.02 eq. Zr^{4+} does not lead to a significant improvement or deterioration of the electrochemical performance compared to undoped $\text{LiFe}_{0.5}\text{Mn}_{0.5}\text{PO}_4/\text{C}$. Therefore, this thesis only deals with isovalent doping of LFMP with different concentrations of Mg^{2+} .

Structural characterization. Figure 48 illustrates the XRD patterns of some magnesium-doped powders in comparison to sample F. It is evident, that the spectra are similar with regard to their peak positions and intensities and no impurities are detected. An increase in magnesium content leads to a shift to slight higher angles.

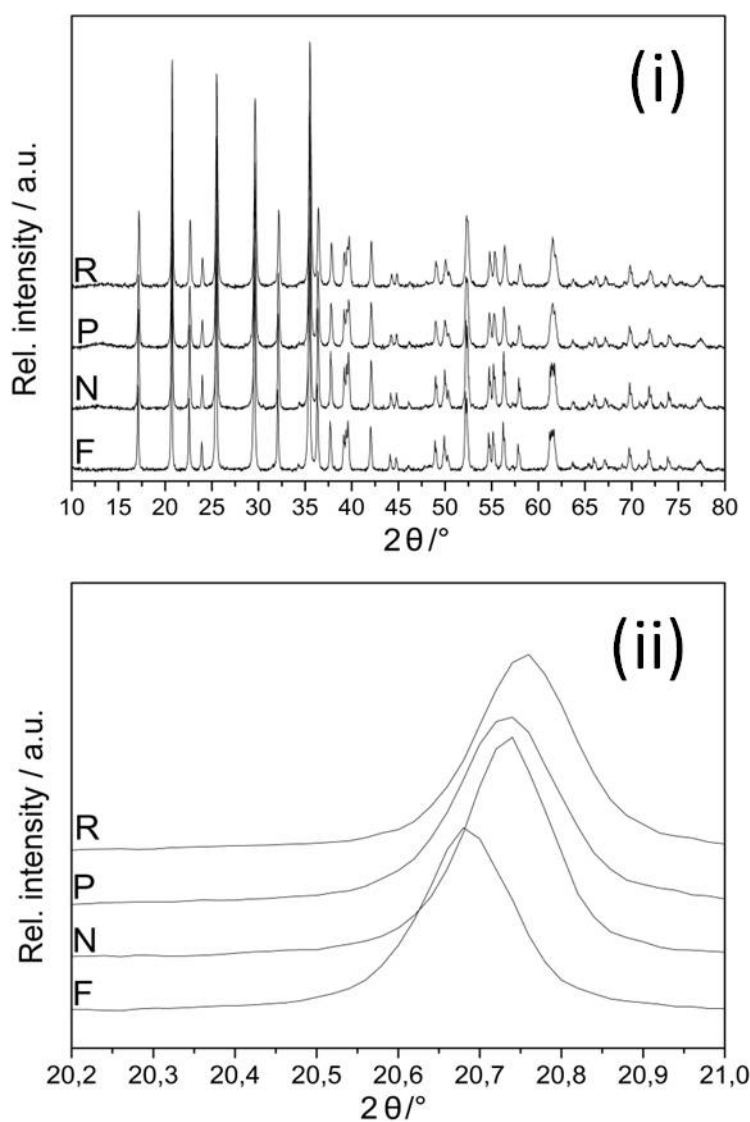


Figure 48: XRD patterns of the (i) magnesium doped LFMP in comparison to sample F. (ii) Magnified view of the same samples from 20.2-21.0 ° 2θ. Only magnesium doped samples N, P and R are shown to avoid complexity.

The decrease in cell volume (cf. Table 23) is caused by the insertion of the smaller Mg^{2+} -ion into the crystal lattice.

Table 23: Lattice parameters of the Mg-doped samples in comparison to sample F. The standard deviation of the lattice constants is shown in brackets.

Sample	a / Å	b / Å	c / Å	Volume / Å ³
F	10.3890(1)	6.0536(1)	4.7191(1)	296.79
N	10.3840(4)	6.0510(2)	4.7203(2)	296.59
O	10.3844(2)	6.0505(1)	4.7186(1)	296.47
P	10.3761(6)	6.0486(4)	4.7209(3)	296.29
Q	10.3770(3)	6.0470(1)	4.7177(1)	296.03
R	10.3672(6)	6.0426(3)	4.7216(3)	295.78

SEM-BSE images of the slope cut of sample P show that the doped sample has a similar morphology as the undoped one. The nanosized particles agglomerate to huger particles with a few μm in size. Particle sizes are non-uniform and all of them are well surrounded by a carbonaceous matrix. By comparing Figure 49 to Figure 44 it is obvious that the particles of the magnesium doped samples do not have any denser particles at the edge of the LFMP agglomerates. EDX spectra reveal that both as „LFMP” marked particles in Figure 49 contain magnesium. Some abrasion of TC grinding balls is detected as well (red, dashed circle).

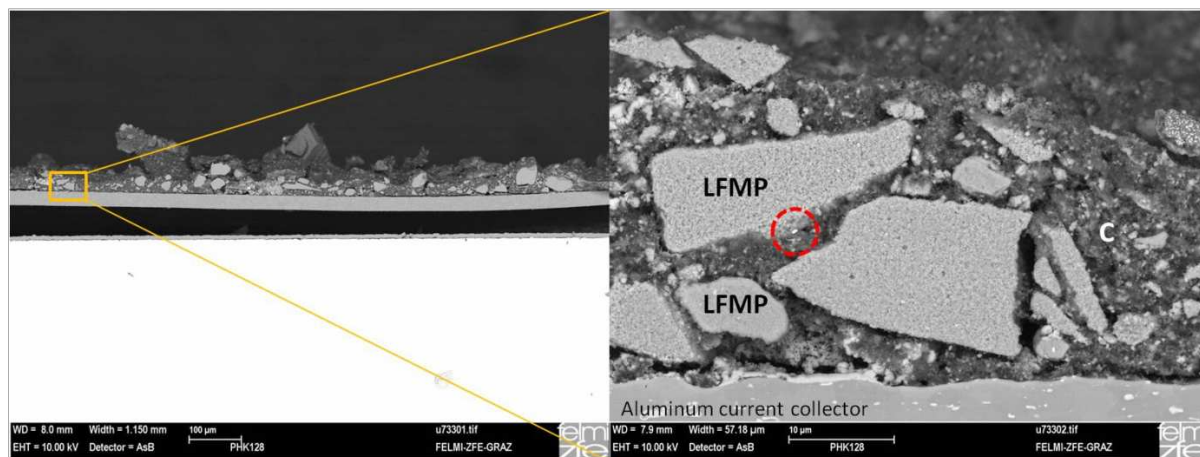


Figure 49: SEM-BSE images of the slope cut of sample P.

Electrochemical tests. As shown by Figure 50, the insertion of Mg^{2+} into the crystal lattice definitely influences the electrochemical performance of the samples. Whereas the position of the $\text{Fe}^{2+}/\text{Fe}^{3+}$ redox couple is quite similar, the reduction of $\text{Mn}^{2+}/\text{Mn}^{3+}$ redox couple is shifted to a higher voltage (cf. Table 24). Therefore, the current peaks for the $\text{Mn}^{2+}/\text{Mn}^{3+}$ redox couple for the magnesium-doped sample are less separated and the reaction is more reversible as for sample F.

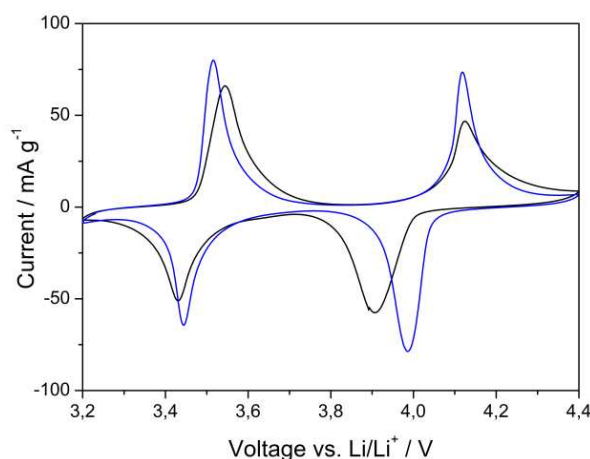


Figure 50: Comparison of the CVs of electrode F (black) and electrode P (blue).

The cause of peak potential shifting of $\text{Mn}^{2+}/\text{Mn}^{3+}$ redox couple is twofold. On the one hand, as mentioned in the theoretical part, the doping of phospho-olivines with isovalent Mg^{2+} leads to an

increase in electronic conductivity. Therefore, redox reactions may occur faster compared to undoped LFMP. On the other hand, magnesium shows a lower electronegativity than iron and manganese. Hence, the positive inductive effect leads to an enrichment of electron density on iron and manganese and their redox couples are shifted to higher voltages. Due to an influence of primarily the $\text{Mn}^{2+}/\text{Mn}^{3+}$ peak position, the better electrochemical performance is rather attributed to the increase in electronic conductivity.

Table 24: Maximum oxidation and reduction peaks vs. Li/Li^+ for the electrodes F, N and P.

	$\text{Fe}^{2+} \rightarrow \text{Fe}^{3+} / \text{V}$	$\text{Fe}^{3+} \rightarrow \text{Fe}^{2+} / \text{V}$	$\text{Mn}^{2+} \rightarrow \text{Mn}^{3+} / \text{V}$	$\text{Mn}^{3+} \rightarrow \text{Mn}^{2+} / \text{V}$
Electrode F	3.55	3.43	4.12	3.91
Electrode N	3.52	3.44	4.12	3.96
Electrode P	3.52	3.44	4.12	3.99

In consideration of the discharge profiles (cf. Figure 51) of the 1st cycles at 0.1 C it turns out that a magnesium content of 0.04 eq. leads to the highest discharge capacity in comparison to sample F.

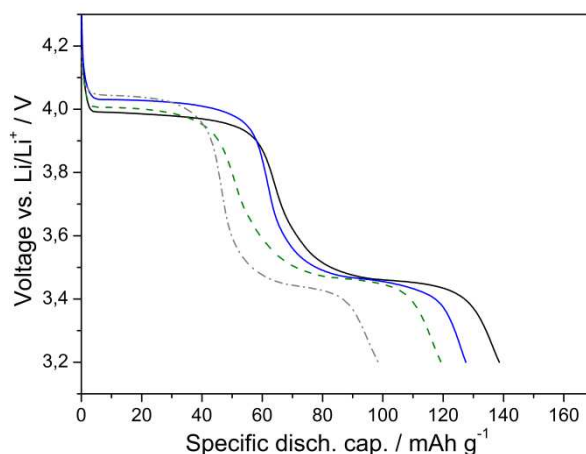


Figure 51: Profiles of the 1st discharge cycle of electrodes F (black), P (blue), N (green) and R (grey).

Therefore, electrochemical results are only shown for sample P. At 0.1 C, the undoped electrode F shows a slight superior electrochemical performance compared to electrode P (cf. Figure 52). After 50 CC cycles at 0.1 C, the initial discharge capacity of 139 mAh g^{-1} and 128 mAh g^{-1} decreases by 97 % and 95 % for active material F and P, respectively. At low current densities, sample F exhibits less capacity fading compared to the magnesium doped one.

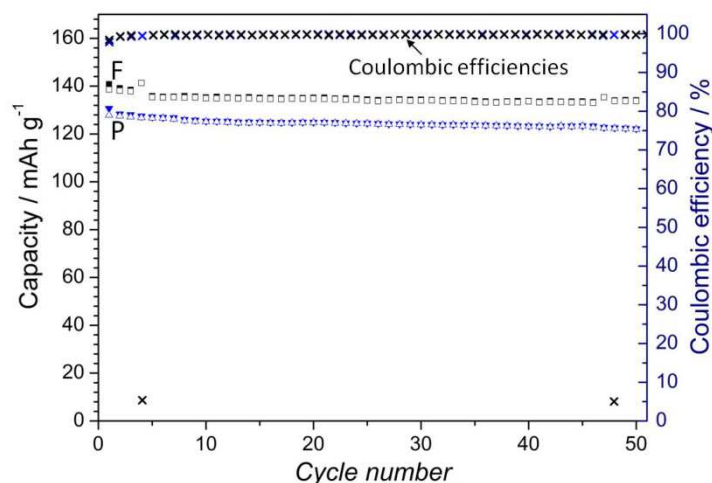


Figure 52: Specific capacities vs. cycle number at 25 °C with a C-rate of 0.1 and corresponding efficiencies for electrode F (black) and electrode P (blue).

At higher current densities an inverse behavior is detected. Both electrodes undergo also 200 cycles at 1 C charge/discharge current. It is obvious from Figure 53 that the magnesium doped sample shows a slightly better cycling stability than sample F. The initial discharge capacities at 1 C are 98 mAh g⁻¹ and 109 mAh g⁻¹ for sample F and sample P, respectively. The residual discharge capacity of sample F is 94 %. On the contrary, sample P is more stable with regard to cycling at higher C-rates, showing a residual discharge capacity of 97 %.

The steady demand for shorter charging times requires active materials that can sustain high current densities. To show the performance of doped and undoped phospho-olivines, as high C-rates such as 5 and 10 are applied to electrode F and P. Figure 54 displays the measured discharge profiles. It is striking that active material P reaches a specific discharge capacity of 50 mAh g⁻¹ at 10 C. At the same C-rate the undoped sample F shows a specific discharge capacity of 36 mAh g⁻¹. Therefore, the conclusion is that even if the doping with the isovalent Mg²⁺-ion does not enhance the capacities of phospho-olivines at low current densities, it definitely improves the high rate performance of the material. The magnesium doping might result in stabilization of the structure since a shortening of the bond lengths and additionally a reduction of the cell volume occurs. These results are consistent with those obtained by Huang et al. [75].

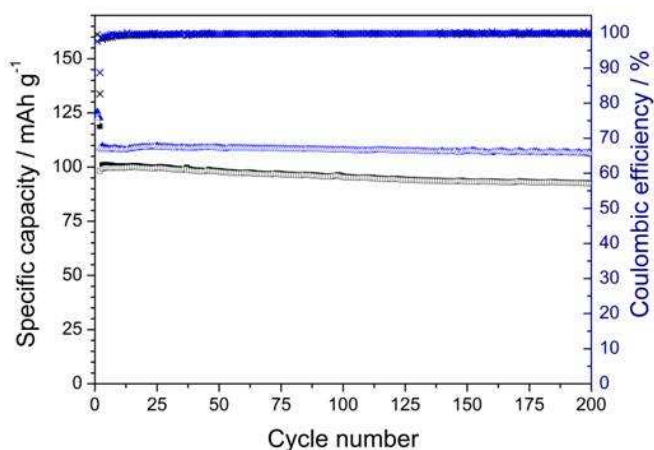


Figure 53: Specific capacities vs. cycle number of electrode F (black) and electrode P (blue) at 25 °C with a C-rate of 1 and corresponding efficiencies.

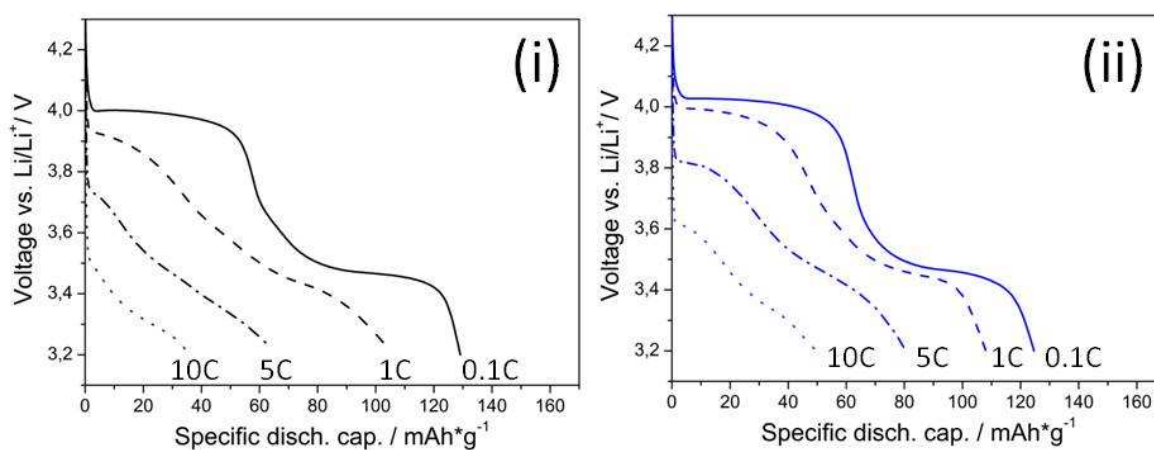


Figure 54: Discharge profiles of (i) electrode F (black) and (ii) electrode P (blue) at different C-rates.

4.1.2.5 Towards high voltage positive electrode materials $\text{LiFe}_x\text{Mn}_y\text{Co}_{1-x-y}\text{PO}_4$

To enhance the energy density of the LIB by applying high voltage cathode materials, solid solutions $\text{LiFe}_x\text{Mn}_y\text{Co}_{1-x-y}\text{PO}_4$ and LiCoPO_4/C are synthesized according to chapter 3.1.2. LiCoPO_4/C is synthesized to serve as reference sample for the comparison of the electrochemical properties. The electrochemical performance of this material is shown in Figure 55. As it can be seen in the CV, two peaks are visible during the extraction of lithium from the electrode. Bramnik et al. [169] attribute this behavior most probably to the formation of two new phases ($\text{Li}_{0.7}\text{CoPO}_4$ and CoPO_4) during charging of the battery. Within their research, they show that CC measurements are not sufficient enough to resolve the two voltage plateaus, whereas potentiostatic intermittent titration technique (PITT) is. The in situ synchrotron XRD studies clearly demonstrate the formation of two two phase regions among the oxidation of LiCoPO_4 . One phase consists of LiCoPO_4 and $\text{Li}_{0.7}\text{CoPO}_4$ whereas the other domain consists of $\text{Li}_{0.7}\text{CoPO}_4$ and CoPO_4 . In the measured CV the two phases are evident at 4.81 V vs. Li/Li^+ and 4.91 V vs. Li/Li^+ . The positions of the two oxidation peaks, which may also result

from polarization of LiCoPO_4/C or from electrolyte oxidation, coincide very well with results from Bramnik et al. [169].

The CC measurements reveal a capacity fade of the electrode. This capacity fading is most likely attributed to the electrolyte oxidation. The slow charging/discharging rate of 0.1 C even promotes the capacity fading since the electrode remains longer in the high voltage region where oxidation of the electrolyte occurs. The CC measurement in Figure 55 illustrates that the initial cycles exhibit a huge discrepancy between specific charge and discharge capacities, resulting in low efficiencies for each cycle. The efficiency is worst within the initial cycles. The reasons to this behavior might be electrolyte decomposition and the limited transport of ions and electrons within the electrode itself. The former can lead to concentration polarization of the electrode, whereas the latter is inherent for phospho-olivine materials. After the 10th cycle, the irreversible efficiency with a value of 20 % per cycle remains more or less unchanged. Only 34 % of the initial specific discharge capacity remains at the end of the 50 CC cycles.

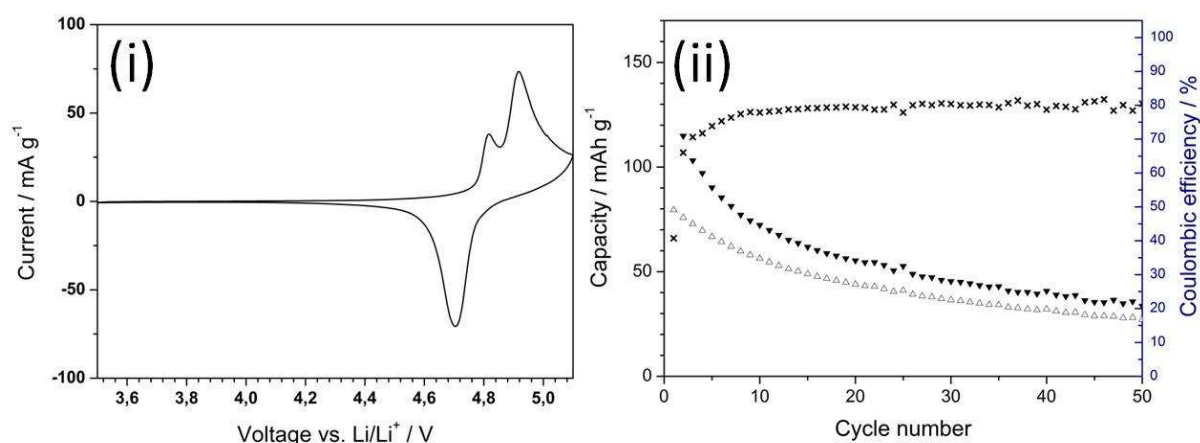


Figure 55: (i) 2nd cycle of the CV and (ii) CC measurement of LiCoPO_4/C .

The electrochemical stability window of the applied electrolyte as well as of another binary electrolyte mixture is shown in Figure 56. It should be noted that the measurement is carried out with a nonporous Pt working electrode. Therefore, results using the LiCoPO_4/C as working electrode may differ. The electrochemical stability window of the Purolyte[®] electrolyte is superior regarding its oxidative stability compared to the binary mixture of EC:EMC. The latter already shows oxidation after 5 V vs. Li/Li^+ . Therefore, application of the LiCoPO_4/C with redox potentials of 4.81 V vs. Li/Li^+ and 4.91 V vs. Li/Li^+ for the oxidation and 4.7 V vs. Li/Li^+ for the reduction reaction is problematic. The cycling behavior might be improved by the application of highly stable electrolytes that are less prone to oxidation at high voltages. But, binary mixtures of organic carbonates remain the electrolyte of choice for ionic conductivity and viscosity reasons so far.

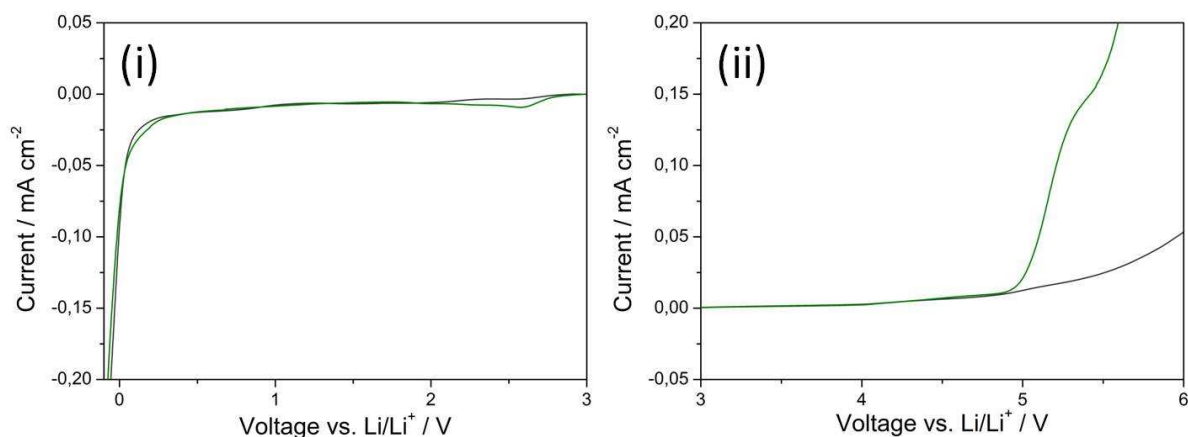


Figure 56: (i) Anodic stability and (ii) cathodic stability of used Purolyte[®] electrolyte (black) and 1 M LiPF₆ in EC:EMC (65.2:32.5, w/w + 2.3 wt% VC, green). The linear sweep voltammograms are recorded with Pt as working electrode at a scan rate of 1 mV s⁻¹.

Structural characterization. As can be seen from XRD diagram of sample S, the appearance of only one peak for the material indicates that a solid solution of the three transition metals has formed. The spectrum reveals the olivine phase and is, again, indexed as orthorhombic Pmnb space group.

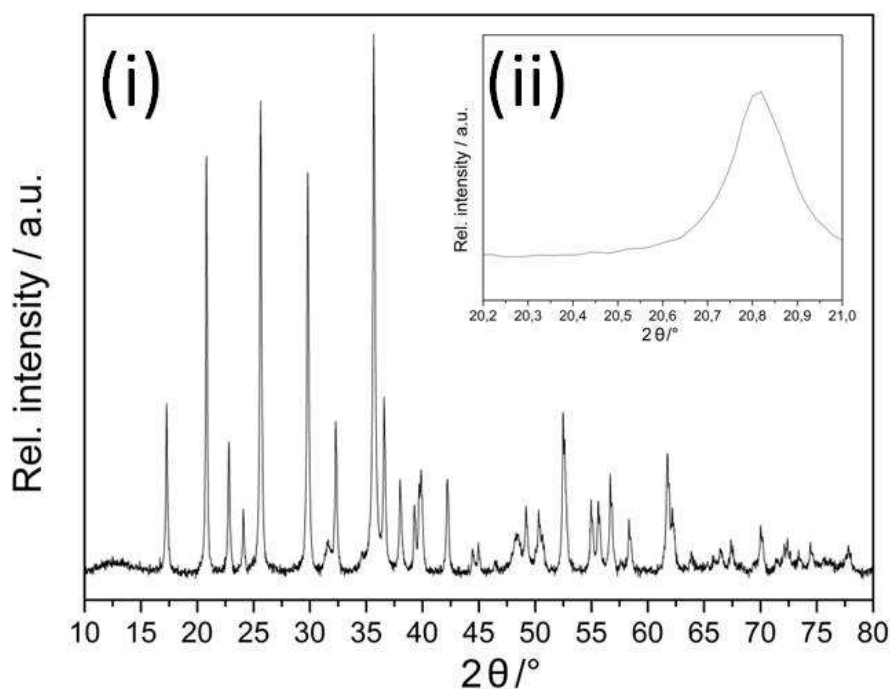


Figure 57: XRD patterns of sample S (i) between 10-80° 2θ and (ii) magnified view between 20.2-21.0° 2θ.

The lattice parameters for samples S, T, U and LiCoPO₄/C are summarized in Table 25. Whereas the cell volume increases with higher manganese and iron content, it decreases as the cobalt content is increased.

Table 25: Lattice parameters (a, b, c and cell volume) of sample S, T, U and LiCoPO₄/C. The standard deviation of the lattice constants is shown in brackets.

Sample	a / Å	b / Å	c / Å	Volume / Å ³
LiCoPO ₄ /C	10.2001(2)	5.9039(1)	4.7003(1)	283.05
S	10.3272(5)	6.0119(4)	4.7154(4)	292.76
T	10.3307(9)	6.0122(5)	4.7074(5)	292.38
U	10.3496(6)	6.0292(4)	4.7181(3)	294.41

Electrochemical tests. To decrease the amount of electrolyte oxidation and thereby enhance the cycle stability, solid solutions LiFe_xMn_yCo_{1-x-y}PO₄ are synthesized. Considering Figure 58, it is evident that three redox couples occur in the solid solution: Fe²⁺/Fe³⁺, Mn²⁺/Mn³⁺ and Co²⁺/Co³⁺. In comparison to Figure 55, no two phase reaction mechanism for the Co²⁺/Co³⁺ redox couple is visible. These results are in accordance with those obtained by Amine et al. [170] and indicate a reversible one stage redox reaction for Co²⁺/Co³⁺ within the solid solution LFMCP. This might be explained by less electrode polarization and parasitic reactions. The solid solution formation of Fe, Mn and Co diminishes the amount of electrolyte oxidation and hence, the mass transfer limitation at the electrode/electrolyte interface might be reduced as well.

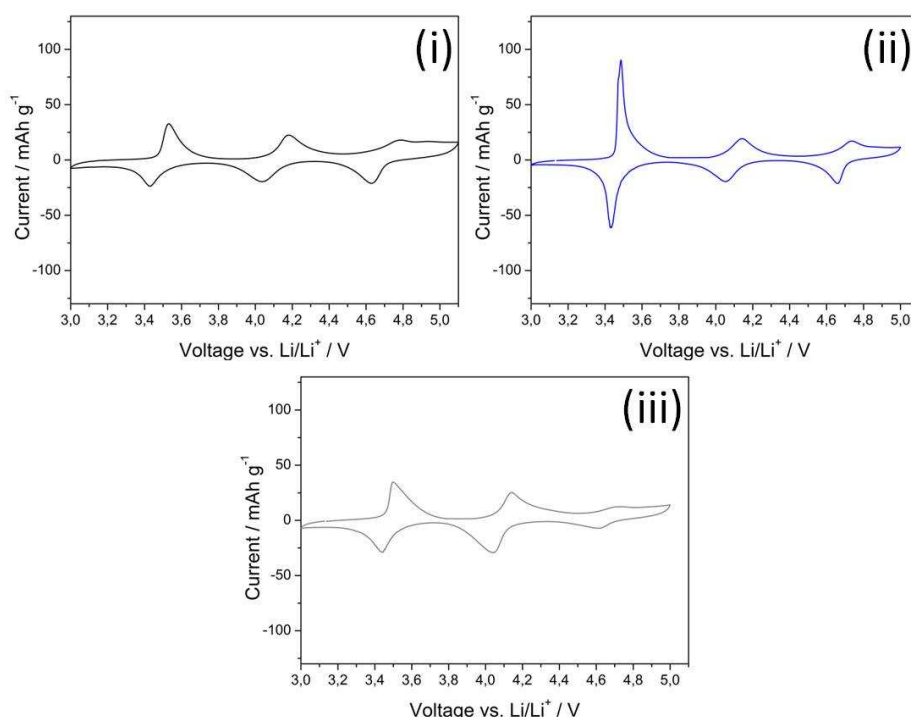


Figure 58: 2nd cycle of the CV for (i) electrode S (black), (ii) electrode T (blue) and (iii) electrode U (grey).

According to literature, the formation of a solid solution LiFe_xMn_yCo_{1-x-y}PO₄ shifts the Co²⁺/Co³⁺ redox potential to lower values. This is favorable for the stability of the electrolyte. Table 26 summarizes the values of the peak maxima obtained by CV measurements. The mutual influence of Fe, Mn and

Co is more pronounced for the oxidation than for the reduction reaction. By withdrawing electron density from the Fe-O and Mn-O bonds through the more electronegative cobalt, the peak positions of the $\text{Fe}^{2+}/\text{Fe}^{3+}$ and $\text{Mn}^{2+}/\text{Mn}^{3+}$ redox reactions are shifted to higher potentials with increasing cobalt content.

Table 26: Maximum of the oxidation and reduction peaks (V vs. Li/Li^+) of the 2nd cycle of the CV for the sample S, sample T and sample U.

Sample	$\text{Fe}^{2+} \rightarrow \text{Fe}^{3+}$	$\text{Fe}^{3+} \rightarrow \text{Fe}^{2+}$	$\text{Mn}^{2+} \rightarrow \text{Mn}^{3+}$	$\text{Mn}^{3+} \rightarrow \text{Mn}^{2+}$	$\text{Co}^{2+} \rightarrow \text{Co}^{3+}$	$\text{Co}^{3+} \rightarrow \text{Co}^{2+}$
S	3.53	3.43	4.18	4.03	4.79	4.63
T	3.48	3.43	4.14	4.05	4.73	4.65
U	3.50	3.44	4.14	4.03	4.72	4.61

Figure 59 displays the specific charge and discharge profiles of the 1st cycle of the CC measurement. Three plateaus, which correspond to the $\text{Fe}^{2+}/\text{Fe}^{3+}$, $\text{Mn}^{2+}/\text{Mn}^{3+}$ and $\text{Co}^{2+}/\text{Co}^{3+}$ redox reactions are visible for both the charge and discharge reactions. According to their molar fractions in the solid solution, these plateaus are more or less pronounced during the oxidation and reduction reactions.

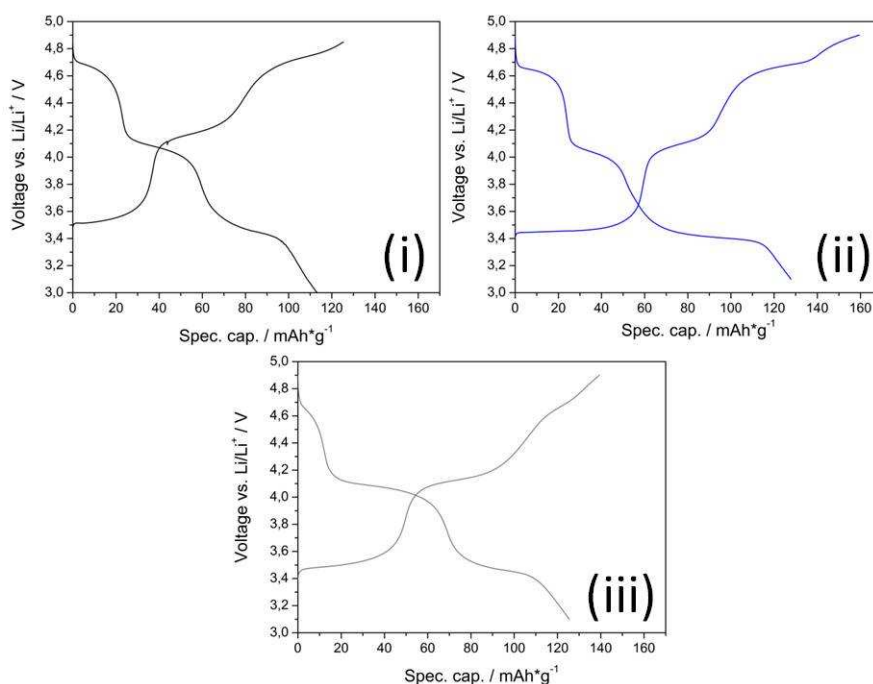


Figure 59: Voltage vs. capacity plots for the 1st cycle of CC measurement of (i) sample S (black), (ii) sample T (blue) and (iii) sample U (grey).

The highest charge capacity of 160 mAh g^{-1} is achieved for sample T. This value is close to the theoretical one. Nevertheless, sample S and U show an irreversible efficiency of approx. 10 %, while sample T exhibits twice as much. Regarding the specific discharge capacities, it is apparent that sample S shows a lower value compared to sample T and U. This phenomenon might be explained by the higher cobalt content and therefore, the higher electrolyte oxidation. By comparing these

samples to LiCoPO_4/C with a first irreversible efficiency of 40 %, the initial cycling performance is definitely improved.

But again, capacity fading arises with proceeding cycle time. Figure 60 illustrates the cumulated irreversible efficiency vs. cycle number. For the 1st and 2nd CC cycle, this value is highest for sample T, followed by sample S and sample U. After the 2nd CC cycle, the irreversible capacities follow a linear trend. It seems that the electrolyte oxidation remains constant for each CC cycle. The values for the irreversible capacities are 6-7 %, 15-16 % and 5 % for sample S, T and U, respectively. As can be seen from these results, an equimolar ratio between iron and manganese with less cobalt content in the solid solution seems favorable with regard to the electrochemical performance of $\text{LiFe}_x\text{Mn}_y\text{Co}_{1-x-y}\text{PO}_4/\text{C}$.

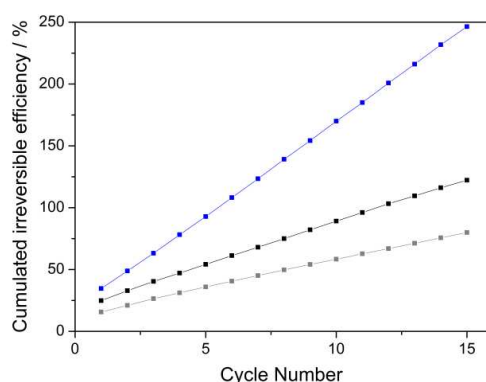


Figure 60: Cumulated irreversible efficiencies vs. cycle number for sample S (black), sample T (blue) and sample U (grey).

To sum up, the incorporation of Co into the crystal lattice of LFMP increases the practical energy density of the material compared to bare LiCoPO_4/C but is to the detriment of the cycle life of the LIB (cf. Table 27). Nevertheless, the calculated energy density of sample F is still superior compared to solid solutions of iron, manganese and cobalt. Unless no electrolyte is developed that is stable against high oxidation potentials, LiCoPO_4/C or solid solutions thereof with Mn and Fe will never be deployed. Anyway, the high theoretical energy density of LiCoPO_4/C should spur further research in novel electrolyte solutions.

Table 27: Specific energy densities for LiCoPO_4/C and the solid solutions of the three transition metals $\text{LiFe}_x\text{Mn}_y\text{Co}_{1-x-y}\text{PO}_4/\text{C}$.

Sample	Spec. cap. / mAh g^{-1} Theoretical	Energy density/ Wh kg^{-1} Theoretical	Energy density / Wh kg^{-1} For the 1 st discharge cycle	Energy density / Wh kg^{-1} For the 50 th discharge cycle
LiCoPO_4/C	167	802	360	121
S	169	696	437	225
T	169	668	482	19
U	167	665	480	439

4.1.3 Conclusion and outlook

Within this thesis, it is shown that an exact stoichiometry is necessary to reduce impurities such as heterosite species among solid state synthesis of $\text{LiFe}_x\text{Mn}_{1-x}\text{PO}_4/\text{C}$. Due to superior electrochemical characteristics of the sample which is synthesized by microwave solvothermal synthesis, this method is further improved. The device-specific parameters of the Anton Paar Monowave 300 limits the microwave irradiation time to a maximum achievable temperature of 300 °C for the reaction mixture. Hence, a post-thermal treatment of the samples is necessary to obtain well defined crystal structures. Furthermore, the decomposition of sucrose during the post-thermal treatment has turned out as a superior carbon source compared to Super P with regard to the energy density of the LIB. The optimum for the pH-value and the precursor concentration in TEG is 6.0-7.5 and 0.14 M, respectively. The particles are identified to form agglomerates in the sub-micrometer range. A decrease in particle size after the post-annealing step undertaken by ball milling has not turned out to be advantageous, since the electrochemical performance of the particles is lost.

Anyway, $\text{LiFe}_x\text{Mn}_{1-x}\text{PO}_4/\text{C}$ is successfully prepared by microwave assisted solvothermal synthesis with a post-annealing step. XRD patterns of the synthesized powders are in good agreement with ICSD reference diffractograms and reveal the olivine phase. An increase in the lattice parameters (a, b, c and cell volume) is observed if the manganese content is increased in $\text{LiFe}_x\text{Mn}_{1-x}\text{PO}_4/\text{C}$. According to XRD patterns, sample G shows only one peak in the spectrum whereas a mixture of 0.4 eq. of active material A and 0.6 eq. of active material K after the oven results in a splitting of the peaks. Two overlapping peaks are also apparent if the powders are mixed after the ball milling step and afterwards post annealed. Accordingly, the formation of a solid solution occurs for microwave solvothermal synthesis accompanied by a post-annealing step as well as for the ball milling step with the same post-thermal treatment.

The formation of solid solutions $\text{LiFe}_x\text{Mn}_{1-x}\text{PO}_4/\text{C}$ leads to superior electrochemical behavior and to a more stable olivine structure compared to poorly-conducting sample K. The two distinct redox couples $\text{Fe}^{2+}/\text{Fe}^{3+}$ and $\text{Mn}^{2+}/\text{Mn}^{3+}$ are both apparent in cyclic voltammograms and in the voltage vs. capacity profiles of CC experiments. Their position is definitely influenced by the iron and manganese content in the sample. Except for electrode F, specific discharge capacity raises if the iron content is increased, but unfortunately at the expense of manganese dissolution and its migration to the counter electrode. Anyway, the superior electrochemical behavior of sample F suggests that an equimolar mixture of iron and manganese within the solid solution is definitely favorable.

GITT measurements show a minor IR drop as well as a faster relaxation for the $\text{Fe}^{2+}/\text{Fe}^{3+}$ compared to the $\text{Mn}^{2+}/\text{Mn}^{3+}$ redox couple. Therefore, the lithium-ion diffusivity is faster for the oxidation and reduction reaction of iron.

Further analysis on the equimolar mixture shows that a solid solution is either formed by microwave irradiation and a post-annealing step or if sample A and sample K are initially ball-milled together with sucrose and then post annealed. Manual mixing of active material A with K before the post-annealing step does not lead to the formation of the solid solution. Since sample M exhibits a worse electrochemical behavior, slope cuts are just performed for sample F and L. They demonstrate a similar morphology for both samples meaning nanosized particles forming agglomerates up to several microns in size that are well embedded into a carbonaceous matrix.

Electrode F achieves a specific discharge capacity of 139 mAh g^{-1} and 115 mAh g^{-1} at 0.1 C and at 1 C , respectively. The two distinct voltage plateaus at 0.1 C exhibit a different behavior upon the application of higher C-rates. In the case of sample L the two distinct plateaus are clearly distinguishable at 1 C , while microwave synthesized sample F shows a rather fading character of the voltage profile for the $\text{Fe}^{3+}/\text{Fe}^{2+}$ redox reaction. The reason might be the lower over-potential of material L compared to sample F. Anyway, the highest energy density of 512 Wh kg^{-1} is achieved for the active material F that is prepared by microwave irradiation.

The isovalent doping of $\text{LiFe}_x\text{Mn}_{1-x}\text{PO}_4/\text{C}$ with magnesium leads to similar electrochemical characteristics at low C-rates compared to the undoped sample. Nevertheless, the rate performance is improved at high current densities. The insertion of 0.04 eq Mg into the crystal lattice results in a specific discharge capacity of 50 mAh g^{-1} at 10 C .

The 5 V cathode material LiCoPO_4/C suffers from severe capacity fading due to the instability of the electrolyte. The formation of solid solutions $\text{LiFe}_x\text{Mn}_y\text{Co}_{1-x-y}\text{PO}_4/\text{C}$ improves the electrochemical performance compared to sheer LiCoPO_4/C . The irreversible capacity of the 1st CC cycle is reduced and further cumulated irreversible efficiencies are improved. Nevertheless, capacity fading cannot be completely avoided and compared to $\text{LiFe}_x\text{Mn}_{1-x}\text{PO}_4/\text{C}$, the main advantage of high cycling stability disappears by the incorporation of Co into the crystal lattice. LiCoPO_4/C and solid solutions thereof with Fe and Mn further exhibit a worse practical, specific energy density compared to $\text{LiFe}_{0.5}\text{Mn}_{0.5}\text{PO}_4/\text{C}$.

For further improvements of the electrochemical performance of $\text{LiFe}_x\text{Mn}_{1-x}\text{PO}_4/\text{C}$, the influence of the solution medium among microwave assisted solvothermal synthesis and its impact on particle size should be determined. The carbon source might be crucial for the final electrode performance and therefore, other sources than sucrose should be investigated. The isovalent doping of the material is favorable for the electrode performance at high C-rates. Hence, other isovalent metals should be introduced into the crystal structure and their performance at high current densities should be investigated.

Regarding the improvement of CC cycling of $\text{LiFe}_x\text{Mn}_y\text{Co}_{1-x-y}\text{PO}_4/\text{C}$, as mentioned in literature for LiCoPO_4/C [171], two different approaches might be crucial to reduce electrolyte oxidation as well as capacity fading. On the one hand, variations in the electrolyte compositions regarding its high voltage stability should be performed. On the other hand, surface coatings of the material such as aluminum coatings from layer deposition could avoid or at least mitigate the electrolyte decomposition.

4.2 Aging behavior of a state-of-the-art LIB electrolyte

The trend towards an ever-higher energy density of LIBs makes the implementation of high voltage positive electrode materials indispensable. The application of LiMnPO_4 and LiCoPO_4 for *next generation LIBs* seems encouraging, due to a higher operating voltage and consequently resulting higher theoretical energy density compared to LiFePO_4 . Nevertheless, LiMnPO_4 suffers from worse lithium-ion diffusion kinetics and inferior electronic conductivity in contrast to LiFePO_4 . It is shown in section 4.1 that solid solutions of iron and manganese in phospho-olivines perform very well, achieving a high gravimetric energy density of 512 Wh kg^{-1} for $\text{LiFe}_{0.5}\text{Mn}_{0.5}\text{PO}_4/\text{C}$ cell chemistry. Even if the electrochemical performance of $\text{LiFe}_{0.5}\text{Mn}_{0.5}\text{PO}_4/\text{C}$ is good, manganese is detected on the counter electrode. Since Mn^{2+} dissolution might promote capacity fading of the LIB as mentioned in chapter 2.2.3.3 and is enhanced at higher temperature, the attention is now drawn to the thermal degradation of state-of-the-art electrolytes. It is important to gain definite comprehension of their thermal aging behavior to make reliable statements about this impact on Mn^{2+} dissolution.

Due to contradictions in literature regarding electrolyte decomposition products and different housing materials, the influence of glassware and polymer surface on thermal electrolyte degradation is first examined. All samples are analyzed according to Figure 61. Further, the impact of protic impurities and silicon species on thermal degradation of the electrolytes is shown. Especially the progression of acid formation (e.g. HF) is followed, since it might be crucial for Mn^{2+} dissolution. Finally, the effects of aged state-of-the-art electrolytes on the electrochemical performance are shown by test cells using carbon coated LFP as positive electrode material. For this experiments, DEC and EC are chosen as solvents, since previous studies have shown that this composition leads to faster degradation compared to e.g. DMC. Generally, all samples show a slight decrease in water content and no further decomposition products are detected by GC-MS of liquid samples.

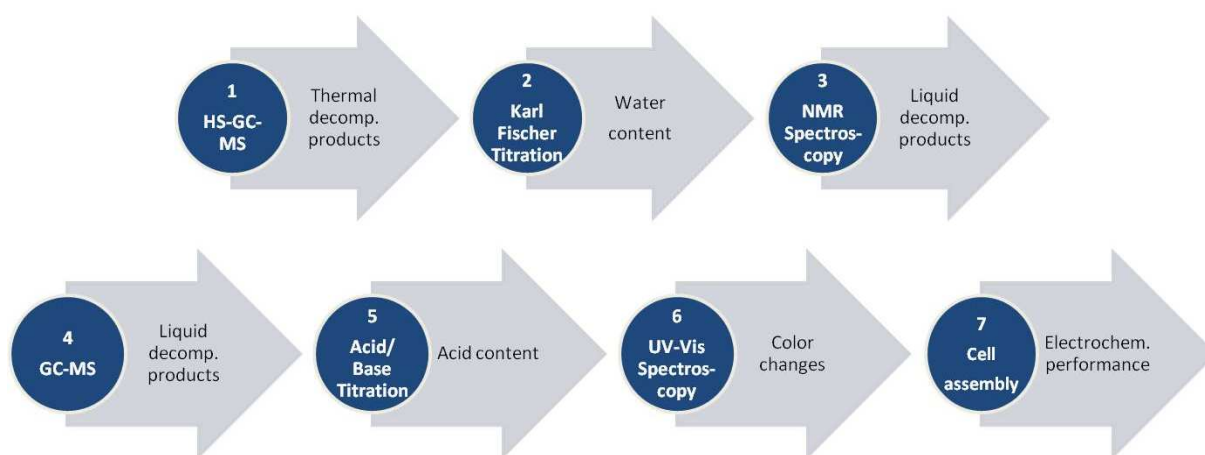


Figure 61: Analysis methods and determined characteristics of the electrolytes aged in pouch bags.

4.2.1 Aging caused by packaging materials

The theoretical part already tackled the problem of different housing materials for liquid electrolytes, which might have an influence on their thermal degradation. Yang et al. [123], for instance, shows that addition of water to the electrolyte does only lead to an enhancement in the acid content upon aging if the electrolyte is not in contact with glassware. On the contrary, other researchers [119][131] find a variety of thermal degradation products but all electrolyte aging experiments are performed in glassware. Therefore, this topic is dealt in greater depth within this chapter and the influence of glassy surface on electrolyte degradation is examined.

4.2.1.1 Glassy surface

If the electrolyte is sealed in Duran® NMR tubes, the ^1H -, ^{19}F -, ^{31}P -, ^{13}C -NMR spectra are in good agreement with the published results of Campion et al. [119] and Ravdel et al. [122] even if a lower decomposition temperature of 60 °C is used. As shown in Table 28, most of the decomposition products already occur after 2 days at elevated temperature.

Table 28: Overview of decomposition products occurring in 1 M LiPF₆ in EC:DEC (40:60, w/w) upon aging at 60 °C in flame sealed, Duran® NMR tubes (^{19}F - and ^{31}P -NMR spectra).

Exposure time	Nucleus	δ/ppm	m	J/Hz	Product species
2 days	$^{19}\text{F} / ^{31}\text{P}$	-74,2 / -144,4	d / sept	708 / 708	LiPF ₆
	$^{19}\text{F} / ^{31}\text{P}$	-85,0 / -19,9	d / t	947 / 947	O=PF ₂ (OH)
	$^{19}\text{F} / ^{31}\text{P}$	-86,0 / -20,8	d / t	1005 / 1005	O=PF ₂ (OEt)
	$^{19}\text{F} / ^{31}\text{P}$	-89,5 / -34,8	d / q	1068 / 1068	O=PF ₃
	^{19}F	-156,4	s		HF
28 days*	$^{19}\text{F} / ^{31}\text{P}$	-85,1 / -10,4	d / d	961 / 961	O=PF(OEt) ₂
	^{19}F	-87,15	d	926	O=PF(OH) ₂
	^{19}F	-212,5	tq	47,9 (CH ₂); 26,7 (CH ₃)	EtF

*Additional decomposition products to those already occurring after 2 days at 60 °C

Difluoro substituted compounds appear after two days, monofluoro substituted decomposition products are observed after 28 days at 60 °C. Monofluoro substituted degradation products develop, if either O=PF₂(OH) is reacting with water or if O=PF₂(OEt) is reacting with further organic carbonate. Since signals in ^{31}P -NMR spectra are overlapping, no clear phosphorus signal is identified for O=PF(OH)₂ with a coupling constant of 926 Hz. The electrolyte samples aged at elevated temperature in sealed Duran® NMR tubes turn yellowish to brownish with increasing time (cf. Figure 62). This change in color may result from the increasing amount of alkylated mono- and difluorinated decomposition products (π -bonding). Further, a white precipitate, which is identified as LiF, is formed on the bottom of the NMR tubes.

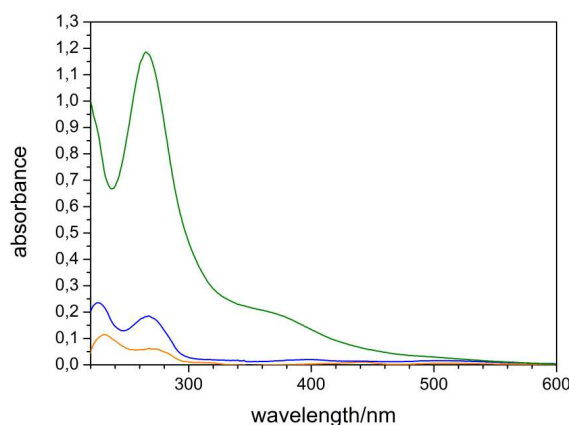


Figure 62: UV-Vis spectrum of 1 M LiPF₆ in EC:DEC (40:60, w/w) aged at 60 °C and in contact with glassware after 2 days (orange), 7 days (blue) and 28 days (green).

Owing to the applied column, acid decomposition products such as fluorophosphoric acids cannot be identified via GC-MS.

Concerning the electrolyte decomposition in glassy headspace vials, phosphoryltrifluoride O=PF₃ (m/z= 104, 85, 69) is present in the background of the electrolyte without any additives. After 2 days at 60 °C the gaseous phase of the thermally aged electrolyte contains Et₂O (m/z= 59, 45, 31), O=PF₂(OEt) (m/z= 115, 103, 85) and O=PF(OEt)₂ (m/z= 155, 127, 81), as shown in Table 29. As for samples aged in Duran[®] NMR tubes, the change of color is also apparent in glassy headspace-GC-MS vials and white precipitate forms on the bottom.

Table 29: Summary of decomposition products of 1 M LiPF₆ in EC:DEC (40:60, w/w) detected by either NMR spectroscopy or HS-GC-MS measurements upon aging at 60 °C in different packaging materials.

Product species	Glassy/Duran [®] surface	Polymer surface
O=PF ₂ (OH)	2 days (NMR)	2 days (NMR)
O=PF ₂ (OEt)	2 days (NMR, HS-GC-MS)	28 days (HS-GC-MS)
O=PF ₃	2 days (NMR)	-
HF	2 days (NMR)	-
O=PF(OEt) ₂	2 days (HS-GC-MS) 28 days (NMR)	-
O=PF(OH) ₂	28 days (NMR)	-
EtF	28 days (NMR)	-
Et ₂ O	2 days (HS-GC-MS)	28 days (HS-GC-MS)

4.2.1.2 Polymer surface

In contrast, aging of the electrolyte in a pouch bag has not led to any detectable decomposition products, except for the difluorinated phosphoric acid ($\text{O}=\text{PF}_2(\text{OH})$). No significant enhancement of its peak intensity has occurred after 28 days at 60 °C compared to the freshly prepared electrolyte. No change in color of the electrolyte samples is observed.

After 28 days exposition at elevated temperature in a pouch bag, the gas-filled compartment of aged electrolytes only contains traces of Et_2O ($m/z= 59, 45, 31$) and traces of $\text{O}=\text{PF}_2(\text{OEt})$ ($m/z= 115, 103, 85$). Since NMR-spectroscopy is less sensitive than GC-MS, decomposition products such as Et_2O or $\text{O}=\text{PF}_2(\text{OEt})$ cannot be identified using this technique because they only occur in trace quantities, if pouch bags are used as sample housing.

As shown by Heider et al. [132] the impact of higher temperature onto the electrolytes generally leads to a faster decrease in water content accompanied by a faster increase in total acid content. Exactly this behavior is followed by acid-base titration and coulometric Karl Fisher titration. During aging the total amount of free acid evolves steadily, depending on the initial concentration of protic impurities and temperature (cf. Figure 63). After 28 days at elevated temperature the total acid content rises even above $4500 \mu\text{g g}^{-1}$ if the electrolyte is in contact with glassware, whereas it stays below $250 \mu\text{g g}^{-1}$ for the electrolyte aged in a pouch bag. Hence the higher the applied temperature and the more the electrolyte is in contact with $-\text{Si}-\text{O}-$ groups from glassware, the more conductive salt decomposition is caused.

To sum up, these findings clearly show that only if the electrolyte is in contact with glass surface during aging the results of NMR-spectroscopy and GC-MS distinguish tremendously from the electrolyte aged in sealed pouch bags. Therefore, the SiO_2 -surface probably promotes the LiPF_6 decomposition.

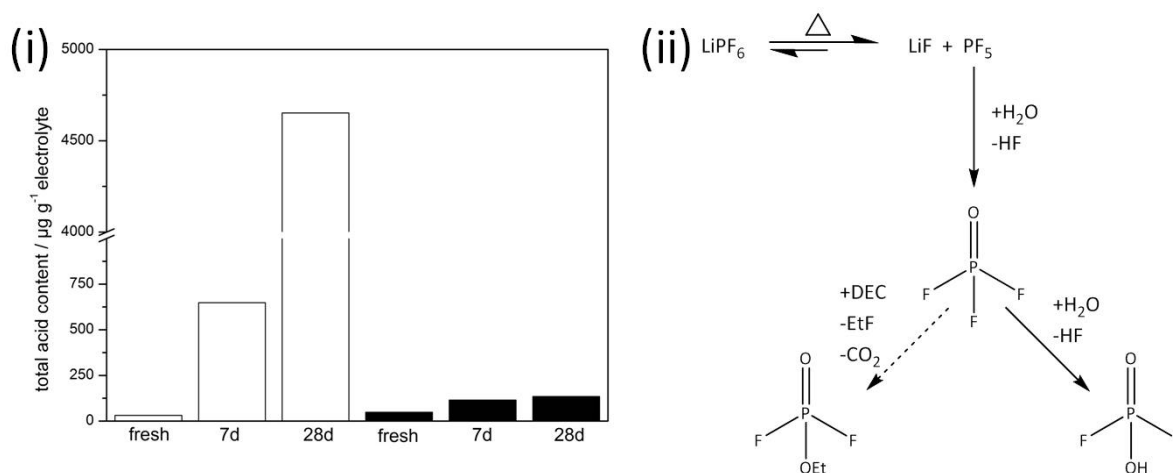


Figure 63: (i) Total acid content of the electrolyte aged during contact with glass vials (white) and with polymer surface (black). (ii) Proposed electrolyte decomposition if only polymer surface is in contact with the electrolyte. The dashed arrow shows the product which is only detected by HS-GC-MS.

Since the aging of electrolytes in air tightly sealed pouch bags mostly resembles the environment of a commercial LIB and is closest to real application, further analysis of electrolyte aging is performed in pouch bags to avoid the environmental impact of e.g. glass surface.

4.2.2 Aging caused by protic impurities

According to literature, an increase in protic impurities leads to a faster decomposition of electrolytes. In commercial LIBs, these protic traces may origin, for example, from electrolyte solvents, poor quality of LiPF₆ (adsorbed HF), aqueous processing of electrode slurries or from the hygroscopy of most common cathode materials and subsequent insufficient electrode drying.

To show the influence of protic contamination on the thermal degradation in a battery-like environment, a certain amount of deionized water as well as of undried LFP powder with a well-known water content are separately added to the chosen electrolyte system and air tightly sealed under argon atmosphere. Hereby, the addition of deionized water should simulate the infiltration of moisture by passive components like the electrolyte or the separator, while the addition of the LFP powder should demonstrate the impact of poorly dried active material. Furthermore, undried LFP powder may offer a catalytic surface in the degradation process in contrast to solely added deionized water.

4.2.2.1 Deionized water

As shown by the NMR spectra in Figure 64, the direct addition of 1000 ppm deionized water only leads to the decomposition product O=PF₂(OH). A minor increase in the peak intensity of O=PF₂(OH) is detected upon storage at elevated temperature with time. No change of color of the electrolyte samples is observed. To determine the increase in decomposition product O=PF₂(OH) quantitatively, inversion recovery experiments are recorded for the electrolyte samples. Benzotrifluoride is used as internal standard and quantification of the total amount of O=PF₂(OH) occurs according to the following equation.

$$m_{O=PF_2(OH)} = \frac{I_{O=PF_2(OH)}}{I_{std}} \times \frac{N_{std}}{N_{O=PF_2(OH)}} \times \frac{M_{O=PF_2(OH)}}{M_{std}} \times \frac{P_{std}}{100} \times m_{std} \quad \text{eq. 30}$$

m Mass / g

I Intensity of the integrals

N Number of NMR active nuclei within the structure

M Molecular weight / g mol⁻¹

P Purity of the internal standard Benzotrifluoride (*std*) / %

The addition of 1000 ppm deionized water leads to an approximate increase of 75 % of O=PF₂(OH) peak intensity upon aging at 60 °C for 28 days compared to its initial concentration, although its concentration in the electrolyte samples is still nominal.

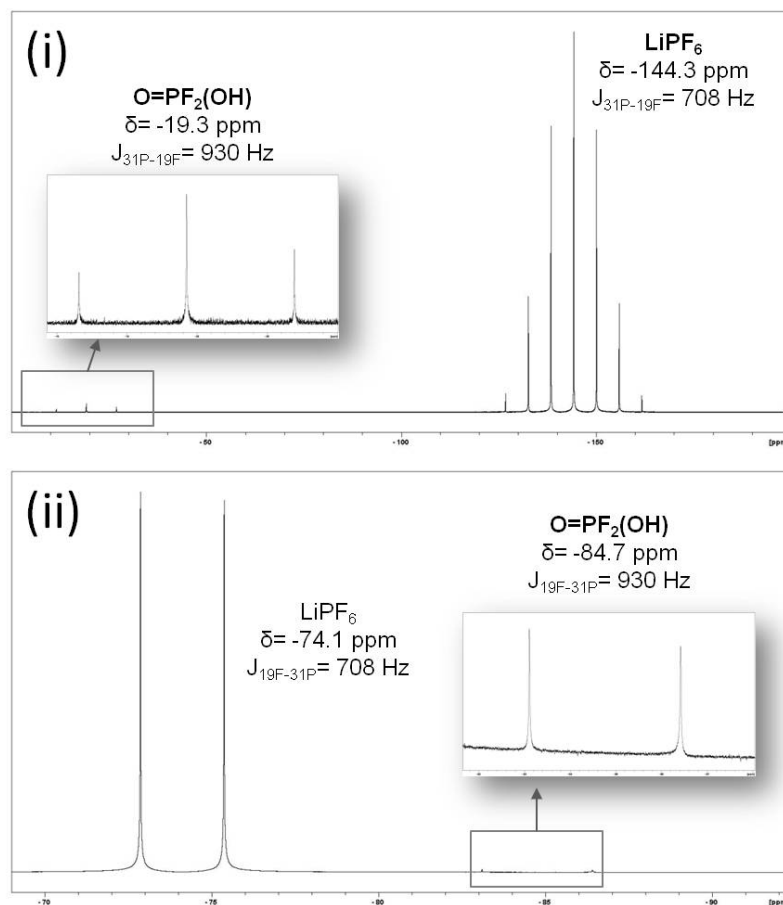
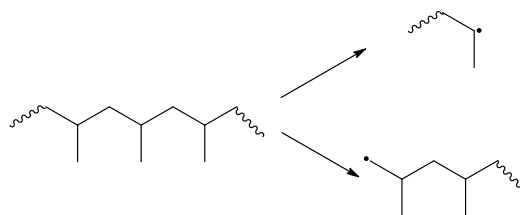


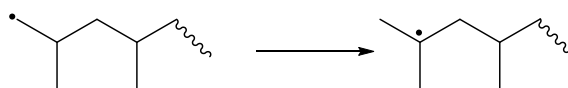
Figure 64: (i) ^{31}P -NMR and (ii) ^{19}F -NMR spectra of 1 M LiPF_6 in EC:DEC (40:60, w/w) aged at 60 °C for 28 days and added 1000 ppm deionized water.

As shown by HS-GC-MS measurements the direct addition of deionized H_2O to the electrolyte samples leads to the formation of Et_2O ($m/z = 59, 45, 31$) and a slight amount of $\text{O}=\text{PF}_2(\text{OEt})$ ($m/z = 115, 103, 85$) in the gaseous phase. Ethanol EtOH ($m/z = 45, 31, 15$) most probably stems from the cleaning of the headspace syringe. Moreover traces of some hydrocarbons are identified like 2-methylprop-1-ene ($m/z = 56, 41, 39$), 2-fluoro-2-methylpropane or fluoroethane ($m/z = 61, 41$), (*E*)-4-methylpent-2-ene ($m/z = 84, 69, 41$) and its tautomer 2-methylpent-2-ene ($m/z = 84, 69, 41$), 2,4,4-trimethylpent-1-ene ($m/z = 112, 97, 57$) and its tautomer 2,4,4-trimethylpent-2-ene ($m/z = 112, 97, 55$). The unsaturated, branched hydrocarbons stem from the decomposition of the inner layer of the pouchbag (polypropylene). It is well-known that acids and increased temperature enhance the cleavage of the polymer chain [172]. To proof this statement, a pouch bag that contains 48 wt% HF and 0.015 g n- SiO_2 is aged for 5 days at 60 °C. Exactly the same unsaturated, branched hydrocarbons and SiMe_2F_2 ($m/z = 81, 47$) are detected. Hence, the hydrocarbons among electrolyte degradation stem from the decomposition of the inner layer of the pouch bag.

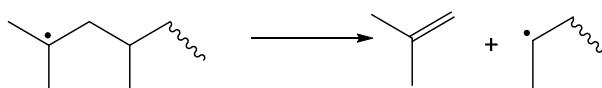
Taking the research of Tsuchiya and Sumi [173] as well as of Bockhorn et al. [174] into account, the following radical formation of the polypropylene chain can be assumed:



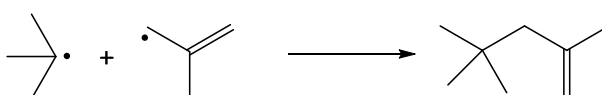
eq. 31



eq. 32



eq. 33



eq. 34

The elevated temperature initiates the polypropylene breakdown and is enhanced by the presence of acids within the electrolyte mixture. Firstly, according to eq. 31, primary and secondary radical molecules develop. The tertiary radical is formed through rearrangement reaction from the primary one (cf. eq. 32). The remaining hydrocarbons and their tautomers result from hydrogen transfer reactions, radical transfer reactions, β -scission and/or radical recombination reactions (cf. eq. 33, eq. 34).

The titration of the electrolyte with 0.002 M Na_2CO_3 -solution shows definitely that the total acid amount is much higher compared to the electrolyte aged with and without undried LFP in a pouch bag. Hence, the higher the applied temperature and the higher the concentration of protic impurities, the more conductive salt decomposition is caused as shown by Figure 65.

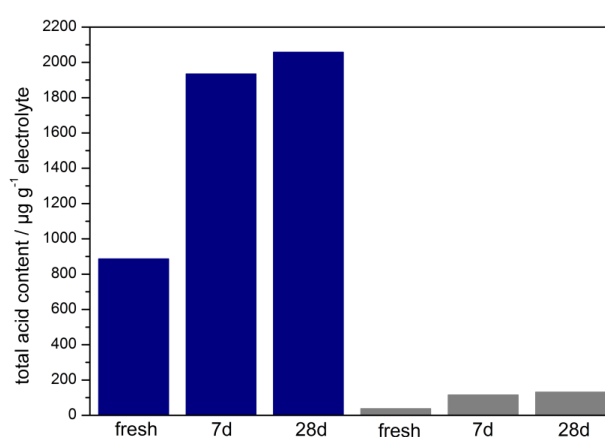
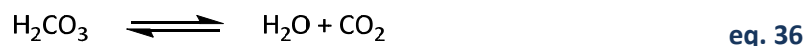
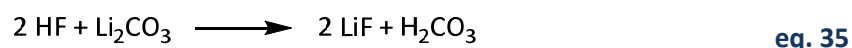


Figure 65: Comparison of the total acid content of the electrolyte aged with 1000 ppm deionized water (blue) and with undried LFP powder (grey).

This increased acid content might be problematic since HF could etch parts of the SEI (eq. 35) on the negative electrode or promote, if contained, the manganese dissolution of the positive one (cf. Figure 19).



4.2.2.2 Undried positive electrode material (LFP)

As for the electrolyte samples with added deionized water, NMR spectra show that the addition of undried LFP only leads to the formation of $\text{O}=\text{PF}_2(\text{OH})$ without any change of color among prolonged heat exposure of the electrolyte.

As illustrated in Figure 66, the addition of undried LFP leads to similar gaseous decomposition products as for the electrolyte with 1000 ppm water. If the samples are aged for 28 days at 60 °C, small amounts of 2-methylprop-1-ene ($m/z= 56, 41, 39$), traces of 2-fluoro-2-methylpropane or fluoroethane ($m/z= 61, 41$) and Et_2O ($m/z= 59, 45, 31$) are determined by HS-GC-MS measurement.

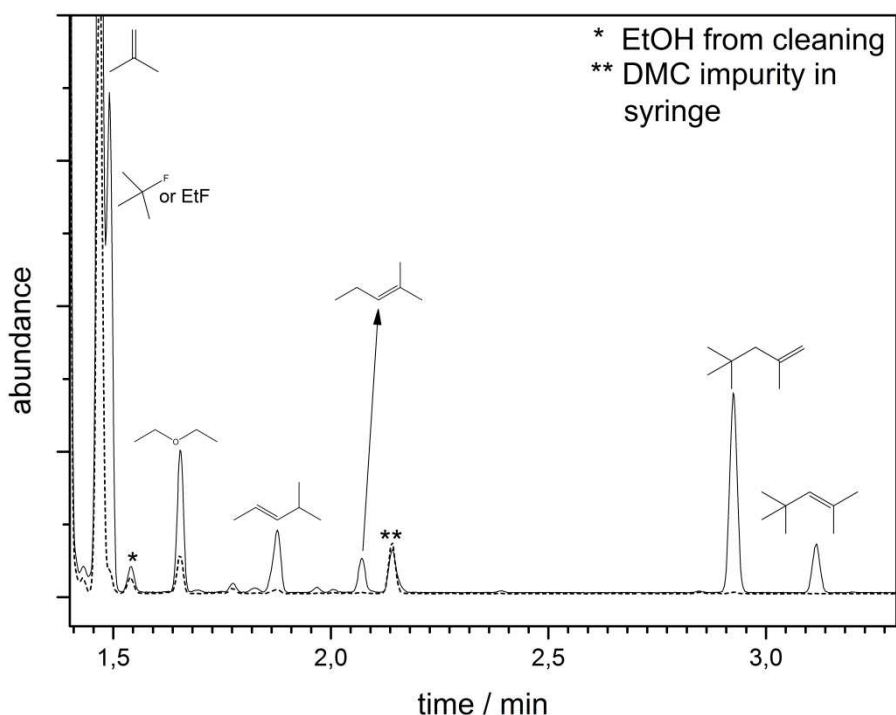


Figure 66: HS-GC-MS chromatograms of the electrolyte aged at 60 °C for 28 days containing either 1000 ppm of deionized water (black, solid line) or 1000 ppm water incorporated in LFP (black, dotted line).

The acid/base titration shows that no acceleration of the electrolyte degradation is visible neither at ambient nor at elevated temperature when undried LFP is added. Approximately the same amounts of acid are detected for the electrolyte with and without added undried LFP aged in pouch bags. Thus, at ambient and elevated temperature the incorporated water in the LFP remains within the powder.

To sum up, the addition of the aforementioned protic impurities to the electrolyte and following aging in pouch bags at elevated temperature leads to the formation of $\text{O}=\text{PF}_2(\text{OH})$ and a slight amount of gaseous products. Generally, undried LFP causes less decomposition of the electrolyte and behaves similar as the pure electrolyte aged in a pouch bag. Nevertheless, the direct addition of deionized water induces the evolution of huge amounts of acid, which might be problematic for the electrochemical performance of the LIB.

4.2.3 Aging caused by silicon species

The thermal degradation of 1 M LiPF_6 in EC:DEC (40:60, w/w) up to monofluoro substituted decomposition products only occurs, if the electrolyte is in contact with Duran® NMR tubes or Supelco® glass vials. To clearly demonstrate whether or not the silicon surface is the main promoter of thermal decomposition, a certain amount of electrolyte in pouch bags containing n- SiO_2 powder is exposed to ambient and elevated temperature. The n- SiO_2 powder should simulate the surface of glassy, sealed NMR-tubes and glassy ampoules, respectively. By addition of dried n- SiO_2 powder to one batch the interferences of absorbed water and the electrolyte should be eliminated. To further examine if absorbed water on the surface of the powder leads to an even faster acceleration of the electrolyte degradation, undried n- SiO_2 powder is added to another batch. Since it turns out that the n- SiO_2 powder definitely influences the electrolyte degradation, problems might be caused by the application of silicon materials as negative electrode material. The -Si-O- surface groups of silicon might influence the thermal decomposition of state-of-the-art electrolytes as well. Hence, a certain amount of dried n-Si powder was added to the chosen electrolyte system and air tightly sealed under argon atmosphere.

4.2.3.1 n- SiO_2 powder (Dried and undried)

Figure 67 illustrates the ^{19}F -NMR and ^{31}P -NMR spectrum of the aged electrolyte containing dried n- SiO_2 powder after 28 days at 60 °C. It is apparent that beside the conductive salt LiPF_6 , decomposition products such as $\text{O}=\text{PF}_2(\text{OH})$ and $\text{O}=\text{PF}_2(\text{OEt})$ occur. ^1H - and ^{13}C -NMR spectra confirm this result. Therefore, the added dried n- SiO_2 powder definitely enhances the thermal aging compared to the electrolyte that is aged in pouch bags. Table 30 summarizes the decomposition products occurring at 60 °C after 2 days and 28 days. Phosphoryl trifluoride $\text{O}=\text{PF}_3$ is only detected after 2 days since it is consumed within the autocatalytic decomposition cycle (eq. 37 to eq. 39).

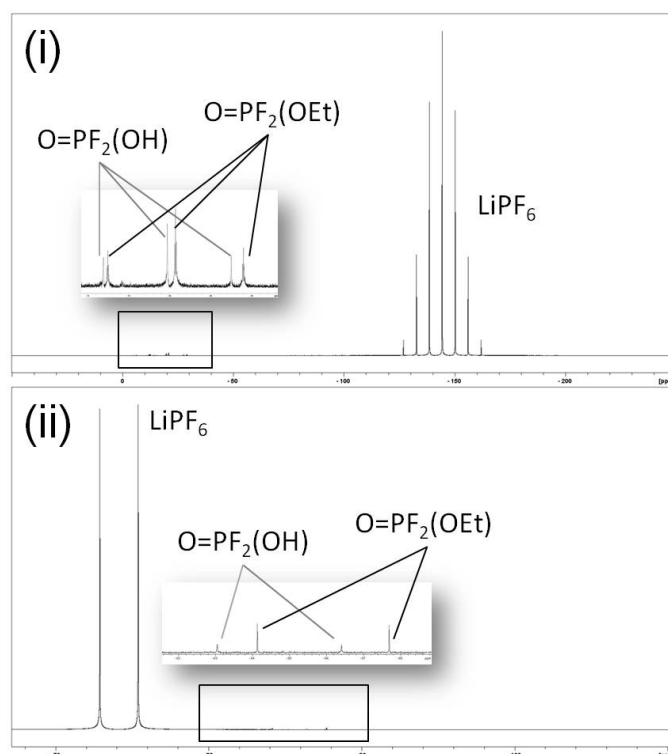


Figure 67: (i) ^{31}P -NMR spectrum and (b) ^{19}F -NMR spectrum of 1 M LiPF_6 in EC:DEC (40:60, w/w) and dried n- SiO_2 powder after 28 days at 60 °C.

Both the addition of undried and of dried n- SiO_2 powder leads to the same decomposition of the electrolyte. In conclusion, the different water content of n- SiO_2 powder does not influence the electrolyte aging according to the NMR spectra.

Table 30: Overview of decomposition products occurring in 1 M LiPF_6 in EC:DEC (40:60, w/w) at 60 °C with added dried and undried n- SiO_2 powder (^{19}F - and ^{31}P -NMR spectra).

exposure time	nucleus	δ/ppm	m	J/Hz	species
2 days	$^{19}\text{F} / ^{31}\text{P}$	-74,1 / -144,3	d / sept	708 / 708	LiPF_6
	$^{19}\text{F} / ^{31}\text{P}$	-84,7/ -19,8	d / t	947 / 947	$\text{O}=\text{PF}_2(\text{OH})$
	$^{19}\text{F} / ^{31}\text{P}$	-85,9 / -20,7	d / t	1005 / 1005	$\text{O}=\text{PF}_2(\text{OEt})$
	$^{19}\text{F} / ^{31}\text{P}$	-89,5 / -34,6	d / q	1068 / 1068	$\text{O}=\text{PF}_3$
28 days	$^{19}\text{F} / ^{31}\text{P}$	-74,1 / -144,3	d / sept	708 / 708	LiPF_6
	$^{19}\text{F} / ^{31}\text{P}$	-84,7/ -19,7	d / t	947 / 947	$\text{O}=\text{PF}_2(\text{OH})$
	$^{19}\text{F} / ^{31}\text{P}$	-85,9 / -20,7	d / t	1005 / 1005	$\text{O}=\text{PF}_2(\text{OEt})$



According to HS-GC-MS measurements, the addition of n-SiO₂ powder leads to the formation of diethyl ether, fluorinated hydrocarbons and unsaturated hydrocarbons (cf. Figure 68). Ethylene fluoride (m/z= 47, 33, 27) is identified in the background of the argon signal. No difference occurs according to the electrolyte decomposition products between dried and undried n-SiO₂ powder. It is noticeable, regarding to the HS-GC-MS spectra that the addition of n-SiO₂ powder leads to exactly the same gaseous decomposition products as the addition of 1000 ppm deionized water (cf. Figure 66 and Figure 68). Again, the huge amount of evolved acids causes the degradation of the inner pouch bag polyolefin layer.

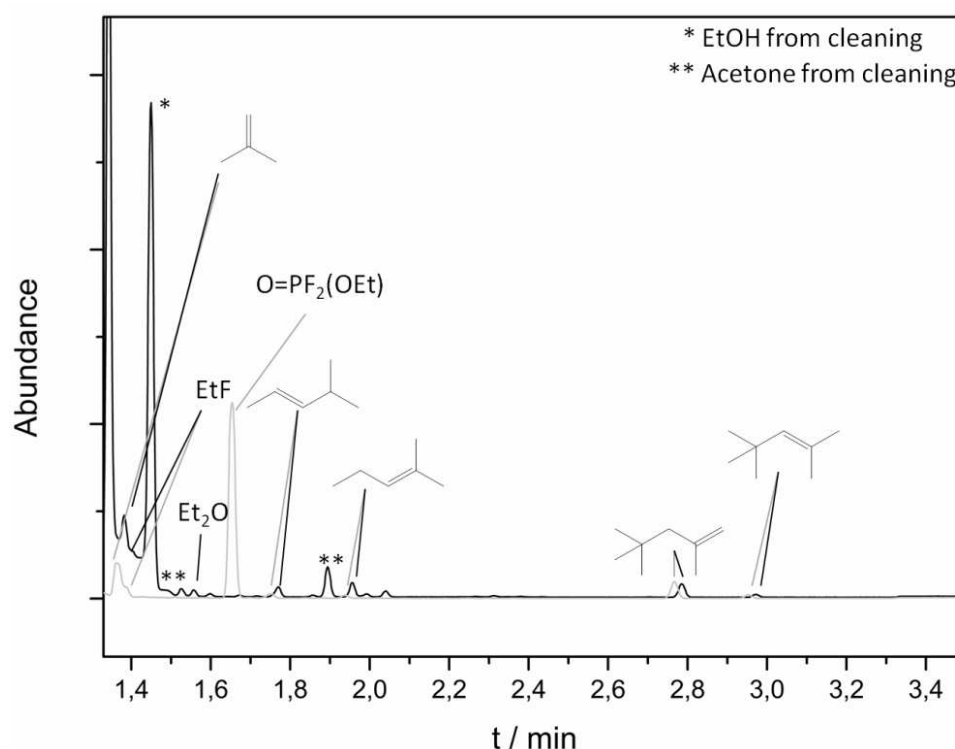


Figure 68: HS-GC-MS spectra after 2 days at 60 °C of 1 M LiPF₆ in EC:DEC (40:60, w/w) with added undried n-SiO₂ powder (black, solid line) and dried n-SiO₂ powder (grey, solid line).

The rising amount of HF and fluorinated phosphoric acids with electrolyte exposure time consumes a higher amount of base Na₂CO₃ during acid-base titration. As can be seen in Figure 69, absorbed water on n-SiO₂ does not lead to higher values of acid formation compared to the electrolyte aged with the dried one. Anyway, it can be noted that n-SiO₂ powder is definitely a promoter of the electrolyte decomposition and is even more severe than protic impurities. Therefore, the highly reactive surface of n-SiO₂ might react with the hydrolysis products of LiPF₆. Lux et al. proposed that n-SiO₂ powder consumes 4 molecules of HF and leads to the formation of the gaseous product SiF₄ and 2 molecules of water [130].



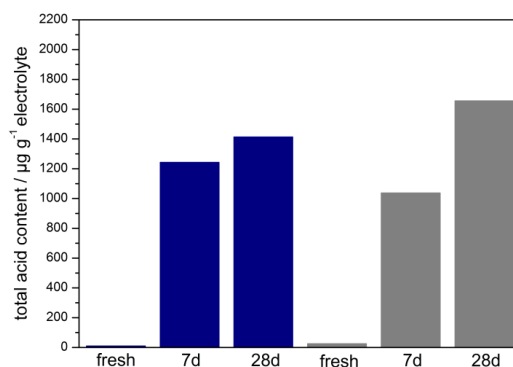
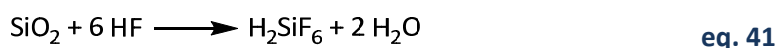


Figure 69: Comparison of the evolvement of free acids for the electrolyte containing either undried n-SiO₂ powder (blue) or dried n-SiO₂ powder (grey) stored up to 28 days at 60 °C.

The etching of the glass surface and the n-SiO₂ powder occurs most probably according to Christe and Wilson [175] and Pande et al. [176], and leads first of all to the formation of hydrofluorosilicic acid H₂SiF₆, which is stable in aqueous media (cf. eq. 41).



Since the electrolyte is mostly composed of aprotic media and only minimum water is contained either in its solvents or released through the etching reaction, H₂SiF₆ is decomposed to lead SiF₄.



Nevertheless, SiF₄, which should appear in the NMR spectrum at -162 ppm [177] is not detected. The only unassigned peak appears in the ¹⁹F-NMR spectrum of the flame sealed Duran[®] NMR tube at -149 ppm. The resonance might correspond to SiF₄ since the surrounding media of the electrolyte can lead to a shift to lower field (F⁻, HF⁻ and HF²⁻). Further, SiF₄ is not detected by HS-GC-MS measurements. It is possible that SiF₄ reacts with the GC column. Therefore, a metal capillary tube (Ultra alloy[®] EGA tube) is installed instead of the HP-5ms GC column. Anyway, it is not possible to detect SiF₄ with this column either. The reason to that is the similar stationary phase compared to the HP-5ms GC column. Therefore, the decomposition product might react with the stationary phase as well, leading only to one clearly detectable peak with a m/z ratio of 85. This m/z ratio might belong to O=PF₂ or even to SiF₃. Hence, uncoated metal capillary tubes and other ionization methods that are more sensitive to the detection of the molecular ion peak should be applied to be able to detect SiF₄.

As for the samples aged in sealed Duran[®] NMR tubes, a hyperchromic shift in the UV-Vis spectrum occurs at the peak maximum of ~274 nm. Therefore, the samples absorb more ultraviolet light upon aging.

4.2.3.2 n-Si powder

Since the difference between dried and undried n-SiO₂ powder is negligible, n-Si powder is only added in its undried form. Considering NMR spectroscopy and GC-MS spectrometry, the same decomposition products are identified as mentioned in section 4.2.3.1. Therefore, the surface groups of n-Si powder cause the same thermal decomposition pathway of 1 M LiPF₆ in EC:DEC compared to n-SiO₂ powder. As shown in Figure 70, there is a difference in the intensity of the ³¹P-NMR signal of O=PF₂(OEt). Whereas the triplet is clearly obvious in the spectrum of the electrolyte with added undried n-SiO₂ powder, it is only minor if n-Si powder is contained. This indicates that the electrolyte decomposition at elevated temperature is slower when undried n-Si powder is added compared to the electrolyte with added undried n-SiO₂ powder.

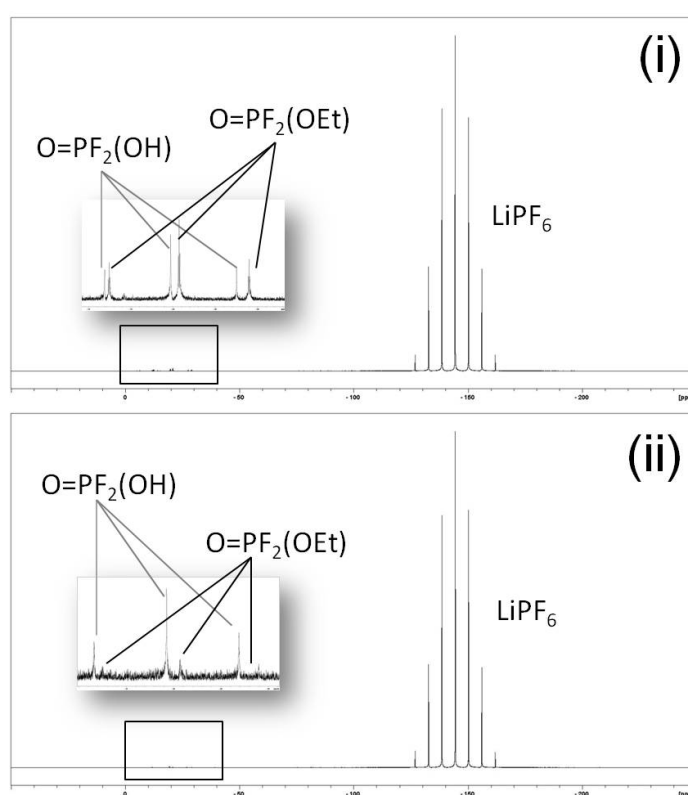


Figure 70: Comparison of the ³¹P-NMR spectrum of 1 M LiPF₆ in EC:DEC (40:60, w/w) with added (i) undried n-SiO₂ powder and (ii) undried n-Si powder after 28 days at 60 °C.

Another difference is observed regarding the total acid content. Figure 71 summarizes the results for the electrolyte with added n-Si powder. The acid content of 1 M LiPF₆ in EC:DEC with added n-Si powder is tenfold lower compared to the electrolytes that contained n-SiO₂ powder. According to eq. 37 to eq. 39 the more -Si-O- surface groups are accessible to the electrolyte, the more acids such as HF or O=PF₂(OH) are generated. Regarding both results, from NMR spectroscopy and acid-base titration, the limited amount of -Si-O- surface groups on n-Si powder leads to a slower thermal degradation of the electrolyte compared to n-SiO₂ powder.

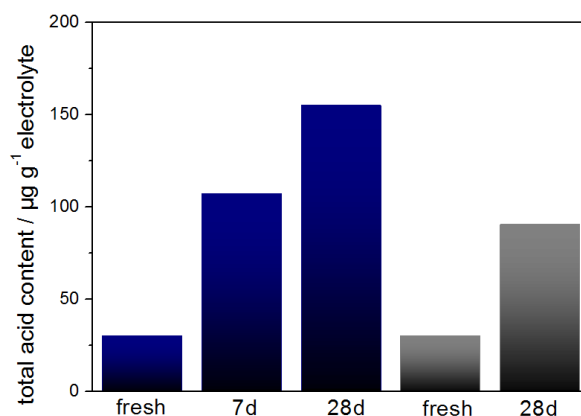


Figure 71: Amount of total acids in 1 M LiPF_6 in EC:DEC (40:60, w/w) containing undried n-Si powder at 60 °C (blue) and at ambient temperature (grey).

4.2.4 Electrochemical behavior of aged electrolytes

It is important to examine the effects of thermally degraded electrolyte, especially considering misuse, harsh storage conditions or failure of the cooling element. Within this chapter, the focus is on the electrochemical performance of test cells assembled by using some of the thermally exposed electrolytes from chapter 4.2.1 to 4.2.3. As decomposition of the electrolyte proceeds faster with elevated temperature and with progressive time, only the electrolytes aged for 28 days at 60 °C are applied.

4.2.4.1 Pouch cells with industrially manufactured electrodes

The assembly of the test cells occurs with a well known battery chemistry used in automotive application: Graphite and carbon coated LFP as negative and positive electrode material, respectively. In order to determine the origin of the differences in voltage profiles, a lithium metal reference electrode is implemented. According to Wu et al. [178] and Belt et al. [179], the application of metallic lithium as reference electrode is possible due to an adequately stable potential among time and temperature. The advantages of lithium metal reference electrode are twofold: On the one hand it sufficiently monitors the individual electrode performances. On the other hand, it is possible to determine the degree of delithiation/lithiation of the materials since the scaling is the same. Nevertheless, metallic lithium is not as stable as NHE reference electrode and possible developments of surface layers as well as polarization effects must not be neglected. These results (cf. Figure 72) agree with literature [178] [179] and show that the measured and calculated cell voltages are in good agreement.

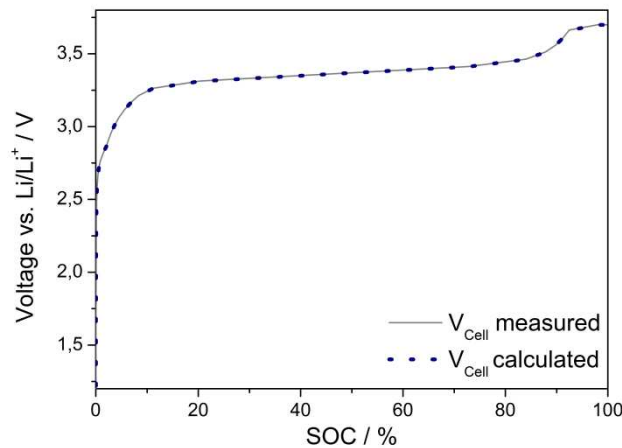


Figure 72: Comparison of the theoretical and calculated cell voltage vs. Li/Li^+ for the cell with the fresh electrolyte.

Figure 73 displays the voltage vs. SOC profile of the formation cycle at 0.1 C for the cell. The cell voltage is similar for the fresh electrolyte and the electrolyte aged in a pouch bag until a value of 30 % SOC is achieved. As the charging proceeds, the resistance of the cell is lowest for the fresh electrolyte, whereas it is highest for the electrolyte that is in contact with glassy surface and n-SiO_2 powder.

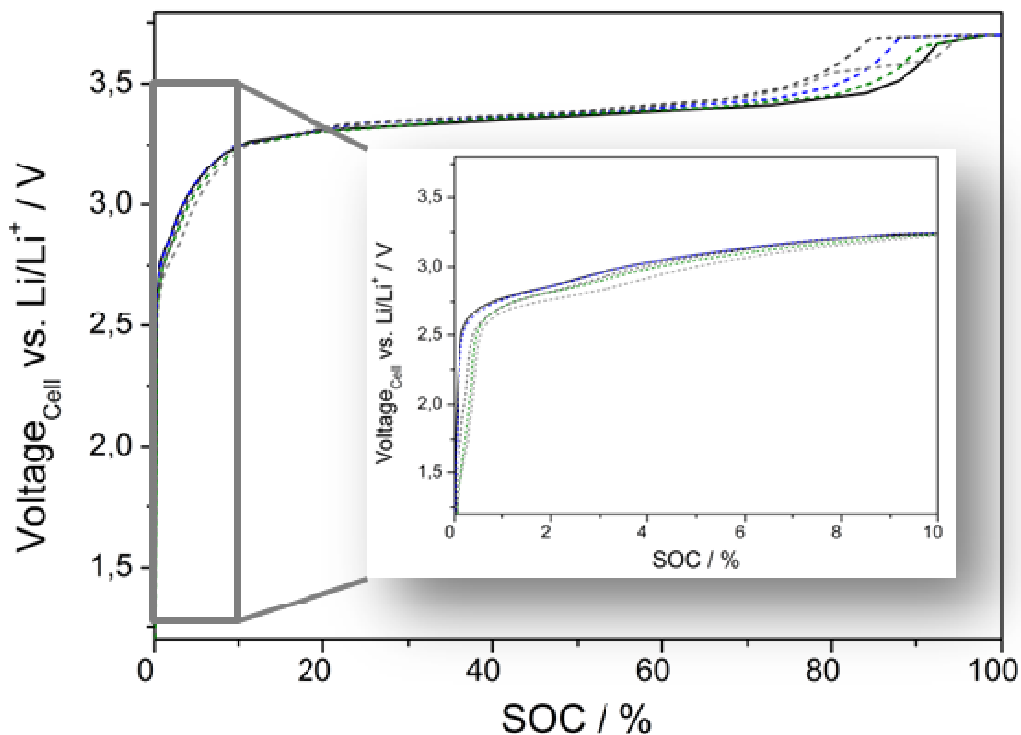


Figure 73: Voltage vs. state-of-charge (SOC) plot of the overall cell voltage vs. Li/Li^+ . Fresh electrolyte (black, solid line) and aged electrolytes: In contact with polymer surface (blue), in contact with glassy surface (grey), with 1000 ppm deionized H_2O (green) and with dried n-SiO_2 powder (dark grey).

The influence of the aged electrolytes on the SEI formation step is of particular interest. Figure 74 displays the voltage vs. SOC plot of the first charge cycle for graphite. It is obvious, that the onset of the SEI formation is at 0.8 V vs. Li/Li^+ . Most reduction occurs for the aged electrolyte in contact with

glassy surface. Since the applied glassware is not dried before sealing, absorbed water as well as -Si-O- surface groups influence the electrolyte decomposition. Therefore, more decomposition products compared to H₂O or n-SiO₂ powder develop among aging. The contained impurities lead to enhanced irreversible decomposition during the formation cycle. According to expectations, the sample with dried n-SiO₂ powder shows more reduction at the anode surface and therefore a higher resistance among charging. In contrast, the resistance among charging for all other aged electrolytes is lower in comparison to the fresh electrolyte. Considering the difference in voltage profiles of anode to cathode, it appears that it is approximately the same for all electrolytes. Therefore, the conclusion is that the small differences in voltage profiles after the SEI formation most possibly originate from a slight difference in positioning of the reference electrode or from contact resistances between metallic lithium and the nickel current collector.

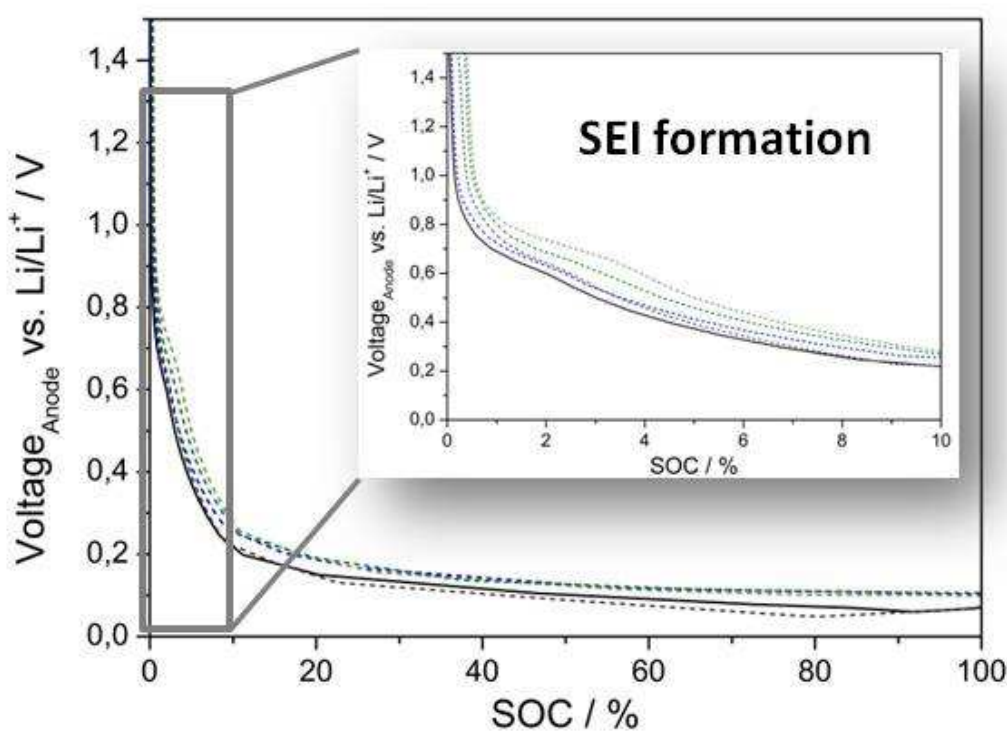


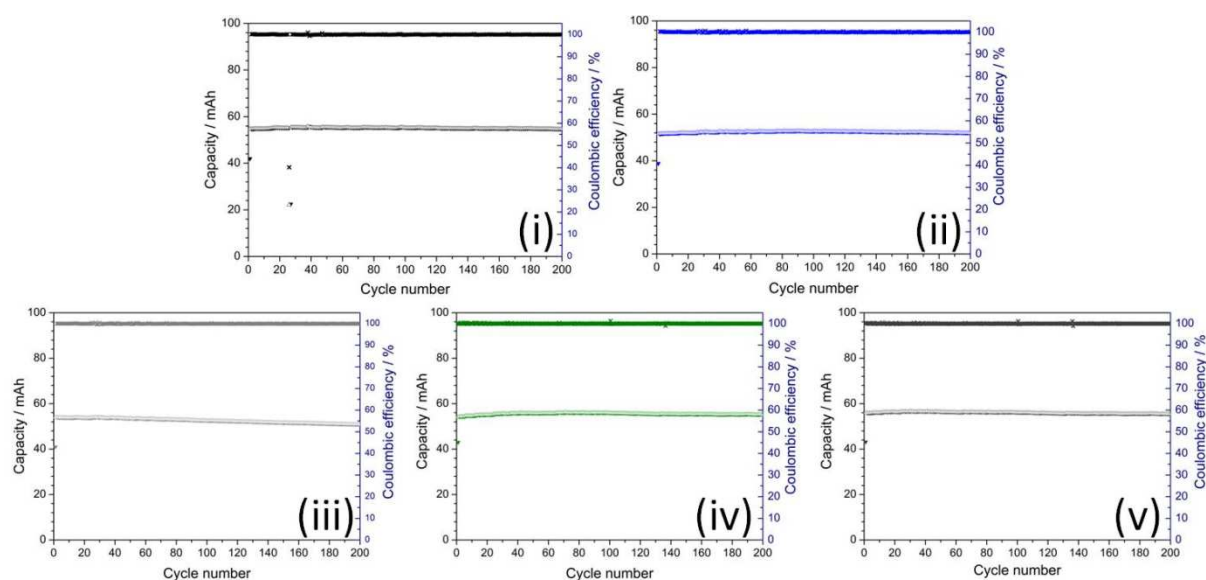
Figure 74: Voltage vs. state-of-charge (SOC) plot for the graphite electrode vs. Li/Li⁺. Fresh electrolyte (black, solid line) and aged electrolytes: In contact with polymer surface (blue), in contact with glassy surface (grey), with 1000 ppm deionized H₂O (green) and with dried n-SiO₂ powder (dark grey).

Table 31 summarizes the charge capacities, discharge capacities and efficiencies that are preserved from the formation cycle. The efficiencies are highest for the fresh electrolyte and the electrolyte aged in a pouch bag. Less than 90 % of efficiency is achieved for the other samples. Hence, water as well as -Si-O- surface groups definitely decrease the charge recovery of the first cycle due to a higher amount of SEI formation and corrosion reactions. Hence, the aging conditions of the electrolyte are crucial in terms of the electrochemical performance of the cell, especially considering the specific energy.

Table 31: Charge and discharge capacities as well as efficiencies for the 1st cycle of the formation procedure.

Sample	Charge cap. / mAh	Discharge cap. / mAh	Efficiency / %
Fresh	69.5	64.7	93.1
Aged in PB	67.3	62.4	92.7
Aged in glass vials	69.2	62.0	89.6
+ 1000 ppm H ₂ O	71.2	61.8	86.8
+ dried n-SiO ₂	69.4	63.9	85.4

The results of the CC curves are summarized in Figure 75 and Table 32. According to the cell specifications, a capacity of 57-58 mAh can be expected at 1 C. Therefore, our results for the initial discharge capacities nearly reach the expected value. It is evident that all cells show a good performance among cycling. The reason for this is most probably the stable cell chemistry.

**Figure 75: Stability during 200 CC cycles of (i) fresh electrolyte and aged electrolytes (ii) in a pouch bag, (iii) in glassy vials, (iv) with 1000 ppm H₂O and (v) with undried n-SiO₂ powder.**

Regarding Table 32, the electrochemical performance of the thermally aged electrolyte in a pouch bag is similar to the fresh one. Even the addition of protic impurities to the electrolyte and subsequent aging at elevated temperature only influences the SEI formation in the 1st CC cycle, but has no impact on further cycling. A correlation exists between the capacity retention and the contact of electrolyte to glass surface or n-SiO₂ during degradation. Upon cycling, the discharge capacity significantly decays if the utilized electrolyte is aged in flame sealed glass vials. Exactly the same behavior, but to a lesser extent, is noticed if the electrolyte is degraded in contact to dried n-SiO₂ powder. Accordingly, the conclusion is that the housing material of the electrolytes during storage is crucial in terms of electrochemical performance of the cell.

Table 32: Initial discharge capacities of the 1st CC cycle and corresponding values of capacity retention after 200 CC cycles.

Sample	Initial discharge cap. / mAh	Capacity retention / %
Fresh	55	99.8
Aged in PB	52	100.0
Aged in glass vials	54	94.0
+ 1000 ppm H ₂ O	55	100.0
+ dried n-SiO ₂	56	98.9

Even if the cycle performance is similar for the fresh and aged electrolytes, the mean discharge voltages differ after prolonged cycling for the aged electrolytes (cf. Table 33). Whereas the fresh electrolyte approximately reaches the same mean discharge voltage after cycling, all aged electrolytes exhibit an increase in cell resistance. Among all aged electrolytes, the cell resistance is highest for the electrolyte aged with 1000 ppm of water and lowest for the electrolyte aged with dried n-SiO₂ powder. Hence, the conclusion is that the surface films and parasitic reactions made from the aged electrolytes have a higher resistance among lithium insertion/extraction compared to the fresh electrolyte.

Table 33: Mean discharge voltages vs. Li/Li⁺ of the 1st and 200th cycle and their absolute difference value.

Sample	Initial voltage / V	Voltage after 200 cycles / V	Δ / mV
Fresh	3.1387	3.1384	0.3
Aged in PB	3.1326	3.1377	5.1
Aged in glass vials	3.1298	3.1368	7.0
+ 1000 ppm H ₂ O	3.1161	3.1069	9.2
+ dried n-SiO ₂	3.1401	3.1371	3

4.2.4.2 Electrochemical performance of LFMP/C half cells containing the aged electrolytes

To show the influence of the aged electrolytes on the cycle performance of solvothermal microwave synthesized solid solutions, Swagelok[®]-T-cells of sample C and sample G are assembled. Therefore, the electrolyte aged in a pouch bag with 1000 ppm deionized water and the electrolyte aged in a glass vial for 28 days at 60 °C are used. These electrolytes are chosen since their amounts of total acids evolved are highest. As known to literature, manganese dissolution is enhanced by acid contents within the electrolyte. Therefore, the effect of high acid contents in the electrolyte on cycling performance is examined. Figure 76 clearly demonstrates that the aged electrolytes lead to capacity fading of the LIB. After 50 CC cycles at 0.1 C, the initial discharge capacity diminishes remarkably for the aged electrolytes compared to the fresh one.

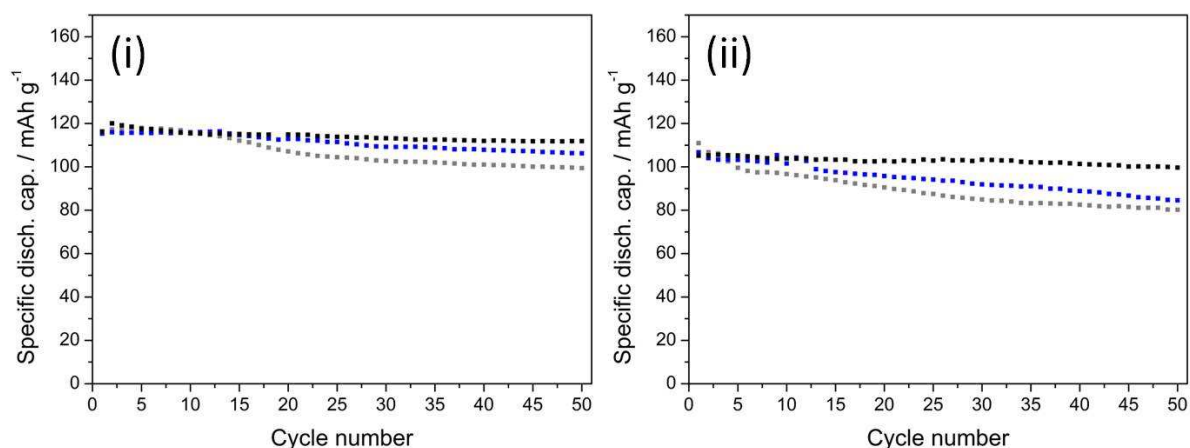


Figure 76: Specific discharge capacities vs. cycle number of the Swagelok®-T-cells cycled with 0.1 C at 25 °C for (i) electrode C and (ii) electrode G. Fresh electrolyte (black), electrolyte aged with 1000 ppm deionized water (blue) and electrolyte aged in a glass vial (grey).

Table 34 summarizes the capacity retentions of the initial discharge capacities. It is evident that the highest capacity fading of the LFMP solid solution results if the electrolyte aged in glass vials is added. Further, the higher the manganese content, the lower the capacity retention. Hence, the evoked acids such as HF and O=PF₂OH upon electrolyte aging definitely lead to a decay in the electrochemical performance, whereby an increase of the dissolved manganese might be the reason.

Table 34: Summary of initial discharge capacities and corresponding capacity retention after 50 CC cycles.

Electrode C	Initial disch. cap. / mAh g ⁻¹	Cap. retention / %
Fresh	116	96
Aged in glass vials	116	86
+ 1000 ppm H ₂ O	115	92
Electrode G	Initial disch. cap. / mAh g ⁻¹	Cap. retention / %
Fresh	105	95
Aged in glass vials	111	72
+ 1000 ppm H ₂ O	107	79

4.2.5 Conclusion and Outlook

To sum up, a method for the characterization of the thermal aging of LIB electrolytes is developed. This method ensures the exclusion of environmental impacts such as e.g. glass surface. Especially the surface of glassware as well as n-SiO₂ powder serves as degradation promoter and leads to the reaction of LiPF₆ with carbonate solvents. Therefore, aging of 1 M LiPF₆ in EC:DEC occurs at a rather low speed as far as influencing variables such as catalytic surface, ambient air, protic impurities and too high temperatures are excluded. Even aging of the electrolyte with added n-Si powder leads to its decomposition. Unfortunately, the elevated temperature and the evolved high amount of acids that result if the electrolyte is in contact with 1000 ppm H₂O or n-SiO₂ powder lead to a slight decomposition of the inner pouch bag layer. Nevertheless, the results suggest that the polypropylene decomposition is likely to have hardly any influence on the electrolyte degradation since only unsaturated, branched hydrocarbons are detected via HS-GC-MS measurements.

This result promotes further investigations to examine the thermally degraded electrolytes in battery test cells. The implementation of metallic lithium on a nickel current collector as reference electrode is successfully performed. Therefore, the cathodic and anodic performances are detected separately. This is of particular interest since the monitoring of the performance of each electrode is useful to improve the cell performance, increase the cycle life and reduce costs of the LIB.

From these results it is evident that most irreversible loss of capacity during the SEI forming step occurs, if the electrolyte has been in contact with glassware during aging. This result is in good accordance with the analysis results of the thermally aged electrolytes. Further, the aged electrolyte with 1000 ppm H₂O shows the second highest amount of reduction at the graphite electrode. Anyway, the prolonged cycling of the test cells with aged electrolyte that contained 1000 ppm H₂O show a good long term performance with hardly any decay in discharge capacity retention. Therefore, the conclusion is that acidic hydrogens from difluorophosphoric acid O=PF₂(OH) as well as from hydrofluoric acid HF are reduced on the anodic surface within the first charge cycle. Afterwards, they do not have an influence on CC performance. Hence, the formed SEI on graphite most probably resembles the SEI from the fresh and the aged electrolyte in a pouch cell.

This contrasts sharply, if the thermal degradation of the electrolyte occurs in contact with glassware or n-SiO₂. The capacity retention after 200 CC cycles at 1 C is lowest if the electrolyte is in contact with glassware, followed by the electrolyte that is aged with dried n-SiO₂ powder. Considering the NMR spectroscopy and GC-MS results, the negative impact on cycling performance most probably stems from the formation of ethyl difluorophosphate O=PF₂(OEt), ethyl monofluorophosphate O=PF(OEt)₂, ethylene fluoride EtF and diethyl ether Et₂O. The developed SEI on graphite might differ from that formed by the fresh electrolyte, resulting in a less stable as well as less flexible surface

layer. Further, the amount of active lithium within the electrolyte is lower since during electrolyte decomposition LiF is formed. Therefore, the electrochemical performance of the cells might be worse as well.

The cell performance of LFMP solid solutions degrades, if either aged electrolytes in glass vials or aged electrolytes with 1000 ppm deionized water are used for cell assembly. A reason to that might be the increase in manganese dissolution. To further proof this assumption, ICP-OES measurements of the lithium metal counter electrodes should be performed and the composition of the resulting SEI on the lithium metal should be examined.

This method, as per description (cf. Figure 61), is and was used to study the influence of different battery components on the thermal aging of the electrolyte and their consequences for electrochemical performance. Due to non-disclosure agreements, these results are not embodied in this thesis.

Future research should focus on the thermal aging of electrolytes and their immediate effects on various battery chemistries. Hence, it should be possible to conclude if the electrochemical performance decline is influenced by the degraded electrolyte to a greater or lesser extent. To gain insight into the resulting electrode/electrolyte interfaces, surface techniques such as SEM-EDX, Fourier transform infrared spectroscopy FTIR and X-ray photoelectron spectroscopy should be applied.

5 Appendix

5.1 List of Chemicals

Table 35: Summary of the used chemicals.

Chemicals	Supplier	Purity
Acetone	Fisher Scientific	≥ 99.97 %
Ammonium dihydrogenphosphate	Sigma Aldrich	98+ %
Cobalt(II) acetate tetrahydrate	Alfa Aesar	≥ 98 %
Dichloromethane	Roth	≥ 99.9 %
Diethylene Carbonate ^a	Sigma Aldrich	≥ 99 %
Dusazin	Fritsch	
Ethylene Carbonate	Acros Organics	≥ 99 %
Hydrofluoric acid	Sigma Aldrich	≥ 48 %
Hydrochloric acid	Merck	suprapur
Iron(II) acetate	Strem Chemicals Inc.	97 %
Iron(II) oxalate dihydrate	Alfa Aesar	99 %
Lithium carbonate	Sigma Aldrich	99.995 %
Lithium hexafluorophosphate	Stella Chemifa Corp.	b.g. ^b
Lithium hydroxide monohydrate	Fluka	≥ 99 %
Lithiumironphosphate	Clariant Int. Ltd.	
Magnesium(II) acetate tetrahydrate	Sigma Aldrich	≥ 99 %
Manganese(II) acetate tetrahydrate	Sigma Aldrich	99 %
Manganese(II) oxalate dihydrate	Alfa Aesar	99 %
n-Si powder	Nanostructured & Amorphous Materials Inc.	99 %
n-SiO ₂ powder	Sigma Aldrich	99 %
Nitric acid ^c		
N-Methyl-2-pyrrolidone	Alfa Aesar	99.5 %
Phosphoric acid	Fluka	85 %
Polyvinylidenfluorid Kynar [®] 761	Creavis Technologies	
Purolyte [®] A6 Series	Novolyte Technologies	b.g.
Sodium pyrophosphate	Alfa Aesar	+ 97 %
Super P [™] Li	Timcal Ltd.	
Tetraethylene glycol	Sigma Aldrich	99 %

^aDistilled for further purification

^bBattery grade

^cPurified by subboiling

5.2 List of Programs for CC experiments

Table 36: GITT program of the Swagelok®-T-cells (PH_GITT_LFMP.000)

STEP 1 (Repeated 35 times)		
Mode	Parameter	Voltage / V
Charge	0.05 C for 40 minutes	4.4
	Rest for 2 hours	
STEP 2 (Repeated 35 times)		
Mode	Parameter	Voltage / V
Discharge	0.05 C for 40 minutes	3.2
	Rest for 2 hours	
STEP 3 (1 full cycle)		
Mode	C-Rate	Voltage / V
Charge	0.1	4.4
Discharge	0.1	3.2

5.3 References

- [1]. **A. J. Bard, M. Stratmann.** *Encyclopedia of Electrochemistry*. Germany : Wiley-VCH GmbH & Co. KGaA, 2007. Chapter 7.
- [2]. <http://www.splung.com/content/sid/3/page/batteries>. [Online] 11. 02. 2015.
- [3]. http://batteryuniversity.com/learn/article/battery_developments. [Online] 11. 02. 2015.
- [4]. **F. Beck, P. Rüetschi.** *Electrochim. Acta.* 45, 2000, p. 2467-2482.
- [5]. **C. Wessells, R. Ruffo, R. A. Huggins, Y. Cui.** *Electrochem. Solid-State Lett.* 13, 2010, p. A59-A61.
- [6]. **Dell, R. M.** *Solid State Ionics.* 134, 2000, p.139-158.
- [7]. **T. Yamahira, H. Kato, M. Anza.** *Nonaqueous electrolyte secondary battery.* US5053297 A Japan, 1990.
- [8]. **N.-S. Choi, Z. Chen, S. A. Freunberger, X. Ji, Y.-K. Sun, K. Amine, G. Yushin, L. F. Nazar, J. Cho, P. G. Bruce.** *Angew. Chem.* 124, 2012, p. 10136.
- [9]. <http://industrial.panasonic.com/ww/products/batteries/secondary-batteries/lithium-ion/cylindrical-type/NCR18650B>. [Online] 27. 04. 2015.
- [10]. **F.R. Kalhammer, B. M. Kopf, D. H. Swan, V. P. Roan, M. P. Walsh.** *Status and Prospects for Zero Emissions Vehicle technology - Report of the ARB Independent Expert panel 2007.* p.25.
- [11]. http://www.iea.org/publications/freepublications/publication/WEO_ES_German. [Online] 12. 02. 2015.
- [12]. **D. A. Notter, M. Gauch, R. Widmer, P. Wäger, A. Stamp, R. Zah, H.-J. Althaus.** *Environ. Sci. Technol.* 44, 2010, p. 6650-6556.
- [13]. **D. Larcher, J.-M. Tarascon.** *Nat. Chem.* 7, 2015, p. 19-29.
- [14]. <http://www.eucar.be/publications>. 20 years of collaboration in automotive research and innovation. [Online] 12. 02. 2015.
- [15]. <http://www.eucar.be/publications>. The Electrification of the Vehicle and the Urban Transport System. [Online] 13. 02. 2015.
- [16]. **D. Linden, T. B. Reddy.** *Handbook of batteries 3rd edition.* USA : Mc-Graw Hill, 2002. Chapter 1-3, 23.
- [17]. **C. Daniel, J. O. Besenhard.** *Handbook of battery materials 2nd edition.* Germany : WILEY-VCH Verlag & Co. KGaA, 2012. Chapter 1.
- [18]. **C. H. Hamann, W. Vielstich.** *Elektrochemie.* Germany : WILEY-VCH Verlag GmbH & Co KGaA, 2005. Chapter 3, 9.
- [19]. **Treptow, R. S.** *J. Chem. Ed.* 79, 2002, p. 334-338.

- [20]. **M. Winter, R. J. Brodd.** *Chem. Rev.* 104, 2004, p. 4245-4269.
- [21]. **Schmickler, W.** *Grundlagen der Elektrochemie.* Germany : Vieweg & Sohn Verlagsgesellschaft mbH, 1996. Chapter 1.
- [22]. **Stangl, C.** *Doctoral Thesis.* 2011. p.21.
- [23]. **M. M .Doeff, R. J. Brodd.** *Batteries for Sustainability.* USA : Springer, 2013. Chapter 2, 3.
- [24]. **Yoshino, A.** *Angew. Chem. Int. Ed.* 51, 2012, p. 5798-5800.
- [25]. **A. Patil, V. Patil, D. W. Shin, J.-W. Choi, D.-S. Paik, S.-J. Yoon.** *Mater. Res. Bull.* 43, 2008, p. 1913-1942.
- [26]. **Brandt, K.** *Solid State Ionics.* 69, 1994, p. 173-183.
- [27]. **Peled, E. J.** *Electrochem. Soc.* 26, 1979, p. 2047-2051.
- [28]. **K. Mizushima, P.C. Jones, P. J. Wiseman, J. B. Goodenough.** *Mater. Res. Bull.* 15, 1980, p. 783-789.
- [29]. **M. Lazzari, B. Scrosati.** *J. Electrochem. Soc.* 127, 1980, p. 773-774.
- [30]. **S. Morzilli, B. Scrosati.** *Electrochim. Acta.* 30, 1985, p. 1271-1276.
- [31]. **B. Di Pietro, M. Patriarca, B. Scrosati.** *J. Power Sources* 8, 1982, p. 289-299.
- [32]. **D. W. Murphy, J. Broadhead, B. C. H. Steele.** *Materials for Advanced Batteries.* New York : Plenum Press, 1980. p. 145-161.
- [33]. **J.-M. Tarascon, M. Armand.** *Nature* 414, 2001, p. 359-367.
- [34]. **N. Nitta, G. Yushin.** *Part. Part. Syst. Charact.* 31, 2014, p. 317-336.
- [35]. **Y. Wang, H. Li, P. He, E. Hosono, H. Zhou.** *Nanoscale* 2, 2010, p. 1294-1305.
- [36]. **J. B. Goodenough, Y. Kim.** *Chem. Mater.* 22, 2010, p. 587-603.
- [37]. **R. Marom, S. Francis Amalraj, N. Leifer, D. Jacob, D. Aurbach.** *J. Mater. Chem.* 21, 2011, p. 9938-9954.
- [38]. **Pistoia, G.** *Lithium-Ion Batteries, Advances and Applications.* Amsterdam : Elsevier, 2014. Chapter 1.
- [39]. **T. Zheng, Y. Liu, E. W. Fuller, S. Tseng, U.v. Sacken, J. R. Dahn.** *J. Electrochem. Soc.* 142, 1995, p. 2581-2590.
- [40]. **M. Wakihara, O. Yamamoto.** *Lithium Ion Batteries: Fundamentals and Performance.* Tokyo : Kodansha Ltd., 1998. Chapter 6.
- [41]. **J. O. Besenhard, H. P. Fritz.** *Angew. Chem. Int. Ed. Engl.* 22, 1983, p. 950-975.
- [42]. **J. R. Dahn, A. K. Sleigh, H. Shi, J. N. Reimers, Q. Zhong, B. M. Way.** *Electrochim. Acta* 38, 1993, p. 1179-1191.
- [43]. **M. Winter, J. O. Besenhard, M. E. Spahr, P. Novák.** *Adv. Mater.* 10, 1998, p. 725-763.

- [44]. **I. Cameán, A. Ramos, N. Cuesta, A. B. Gracia.** *J. Electrochem. Soc.* 161, 2014, p. A2026-A2030.
- [45]. **S. J. Harris, A. Timmons, D. R. Baker, C. Monroe.** *Chem. Phys. Lett.* 485, 2010, p. 265-274.
- [46]. **T. Tran, K. Kinoshita.** *J. Electroanal. Chem.* 386, 1995, p. 221-224.
- [47]. **D. Aurbach, B. Markovsky, I. Weissman, E. Levi, Y. Ein-Eli.** *Electrochim. Acta* 45, 1999, p. 67-86.
- [48]. **X. Y. Song, K. Kinoshita, T. D. Tran.** *J. Electrochem. Soc.* 143, 1996, p. L120-L122.
- [49]. **M. Liang, L. Zhi.** *J. Mater. Chem.* 19, 2009, p. 5871-5878.
- [50]. **Dey, A. N.** *J. Electrochem. Soc.* 118, 1971, p. 1547-1549.
- [51]. **Zhang, W.-J.** *J. Power Sources* 196, 2011, p. 13-24.
- [52]. **C. Liang, M. Gao, H. Pan, Y. Liu, M. Yan.** *J. Alloys Compd.* 575, 2013, p. 246-256.
- [53]. **W. Wang, M. K. Datta, P. N. Kumta.** *J. Mater. Chem.* 17, 2007, p. 3229-3237.
- [54]. **M. N. Obrovac, L. Christensen, D. B. Le, J. R. Dahn.** *J. Electrochem. Soc.* 154, 2007, p. A849-A855.
- [55]. **J. O. Besenhard, M. Hess, P. Komenda.** *Solid State Ionics.* 40/41, 1990, p. 525-529.
- [56]. **H. B. Wu, J. S. Chen, H. H. Hng, X. W. Lou.** *Nanoscale* 4, 2012, p. 2526-2542.
- [57]. **O. Poizot, S. Laruelle, S. Grungeon, L. Dupont, J.-M. Tarascon.** *Nature* 407, 2000, p. 496-499.
- [58]. **L. Aldon, P. Kubiak, M. Womes, J. C. Jumas, J. Olivier-Fourcade, J. L. Tirado, J. I. Corredor, C. Pérez Vicente.** *Chem. Mater.* 16, 2004, p. 5721-5725.
- [59]. **E. Ferg, R. J. Gummow, A. de Kock.** *J. Electrochem. Soc.* 141, 1994, p. L147-L150.
- [60]. **X. Sun, P. V. Radovnovic, B. Cui.** *New J. Chem.* 39, 2015, p. 38-63.
- [61]. **A. K. Padhi, K. S. Nanjundaswamy, J. B. Goodenough.** *J. Electrochem. Soc.* 144, 1997, p. 1188-1194.
- [62]. **H. Huang, S.-C. Yin, L. F. Nazar.** *Electrochem. Solid-State Lett.* 4, 2001, p. A170-A172.
- [63]. **K. Zaghib, A. Guerfi, P. Hovington, A. Vijh, M. Trudeau, A. Mauger, J. B. Goodenough, C. M. Julien.** *J. Power Sources* 232, 2013, p. 357-369.
- [64]. **B. L. Ellis, K. T. Lee, L. F. Nazar.** *Chem. Mater.* 22, 2010, p. 691-714.
- [65]. **O. K. Park, Y. Cho, S. Lee, H.-C. Yoo, H.-K. Song, J. Cho.** *Energy Environ. Sci.* 4, 2011, p. 1621-1633.
- [66]. **V. Srinivasan, J. Newman.** *J. Electrochem. Soc.* 151, 2004, p. A1517-A1529.
- [67]. **C. Delmas, M. Maccario, L. Croguennec, F. Le Cras, F. Weill.** *Nat. Mater.* 7, 2008, p. 665-671.
- [68]. **G. Brunetti, D. Robert, P. Boyle-Guillemaud, J. L. Rouvière, E. F. Rauch, J. F. Martin, J. F. Colin, F. Bertin, C. Cayron.** *Chem. Mater.* 23, 2011, p. 4515-4524.

- [69]. **Z. Chen, J. R. Dahn.** *J. Electrochem. Soc.* 149, 2002, p. A1184-A1189.
- [70]. **C. Delacourt, P. Poizot, S. Levasseur, C. Masquelier.** *Electrochem. Solid-State Lett.* 9, 2006, p. A352-A355.
- [71]. **C. A. J. Fisher, V. M. H. Prieto, M. S. Islam.** *Chem. Mater.* 20, 2008, p. 5907-5915.
- [72]. **N. Meethong, Y.-H. Kao, S. A. Speakman, Y.-M. Chiang.** *Adv. Funct. Mater.* 19, 2009, p. 1060-1070.
- [73]. **H. Liu, Q. Cao, L. J. Fu, C. Li, Y. P. Wu, H. Q. Wu.** *Electrochem. Commun.* 8, 2006, p. 1553-1557.
- [74]. **X. Ou, G. Liang, L. Wang, S. Xu, X. Zhao.** *J. Power Sources* 184, 2008, p. 543-547.
- [75]. **Y. Huang, Y. Xu, X. Yang.** *Electrochim. Acta* 113, 2013, p. 156-163.
- [76]. **V. Etacheri, R. Marom, R. Elazari, G. Salitra, D. Aurbach.** *Energy Environ. Sci.* 4, 2011, p. 3243-3262.
- [77]. **N. V. Kosova, O. A. Podgornova, E. T. Devyatkina, V. R. Podugolnikov, S. A. Petrov.** *J. Mater. Chem. A* 2, 2014, p. 20697-20705.
- [78]. **C. Delacourt, L. Laffont, R. Bouchet, C. Wurm, J.-B. Leriche, M. Morcette, J.-M. Tarascon, C. Masquelier.** *J. Electrochem. Soc.* 152, 2005, p. A913-A921.
- [79]. **Y. Cao, J. Duan, G. Hu, F. Jiang, Z. Peng, K. Du, H. Guo.** *Electrochim. Acta* 98, 2013, p. 183-189.
- [80]. **X.-L. Pan, C.-Y. Xu, D. Hong, H.-T. Fang, L. Zhen.** *Electrochim. Acta* 87, 2013, p. 303-308.
- [81]. **T. Muraliganth, A. Manthiram.** *J. Phys. Chem. C* 114, 2010, p. 15530-15540.
- [82]. **D. Bhuvaneshwari, Gangulibabu, C.-H. Doh, N. Kalaiselvi.** *Int. J. Electrochem. Sci.* 6, 2011, p. 3714-3728.
- [83]. **S. K. Martha, J. Grinblat, O. Haik, E. Zinigrad, T. Drezen, J. H. Miners, I. Exnar, A. Kay, B. Markovsky, D. Aurbach.** *Angew. Chem. Int. Ed.* 48, 2009, p. 8559-8563.
- [84]. **J. Hong, F. Wang, X. Wang, J. Graetz.** *J. Power Sources* 196, 2011, p. 3659-3663.
- [85]. **L. Damen, F. De Giorgio, S. Monaco, F. Veronesi, M. Mastragostino.** *J. Power Sources* 218, 2012, p. 250-253.
- [86]. **D. Wang, C. Ouyang, T. Drézen, I. Exnar, A. Kay, N.-H. Kwon, P. Guerec, J. H. Miners, M. Wang, M. Grätzel.** *J. Electrochem. Soc.* 157, 2010, p. A225-A229.
- [87]. **A. Paoella, G. Bertoni, E. Dilena, S. Marras, A. Ansaldo, L. Manna, C. George.** *Nano Lett.* 14, 2014, p. 1477-1483.
- [88]. **D.-W. Han, Y.-M. Kang, R.-Z. Yin, M.-S. Song, H.-S. Kwon.** *Electrochem. Commun.* 11, 2009, p. 138-140.

- [89]. H. Li, Y. Chen, L. Chen, H. Jiang, Y. Wang, H. Wang, G. Li, Y. Li, Y. Yuan. *Electrochim. Acta* 143, 2014, p. 407-414.
- [90]. R. Koksang, J. Barker, H. Shi, M. Y. Saidi. *Solid State Ionics* 84, 1996, p. 1-21.
- [91]. Goodenough, J. B. *J. Power Sources* 174, 2007, p. 996-1000.
- [92]. B. Xu, D. Qian, Z. Wang, Y. S. Meng. *Mater. Sci. Eng. B.* 73, 2012, p. 51-65.
- [93]. J. M. Tarascon, W. Wang, F. K. Shokoohi, W. R. McKinnon, S. Colson. *J. Electrochem. Soc.* 138, 1991, p. 2859-2864.
- [94]. R. J. Gummow, A. de Kock, M. M. Thackeray. *Solid State Ionics* 69, 1994, p. 59-67.
- [95]. X. Xiao, D. Ahn, Z. Liu, J.-H. Kim, P. Lu. *Electrochem. Commun.* 32, 2013, p. 31-34.
- [96]. A. J. Smith, S. R. Smith, T. Bynne, J. C. Burns, J. R. Dahn. *J. Electrochem. Soc.* 159, 2012, p. A1696-A1701.
- [97]. E. Hu, S. M. Bak, S. D. Senanayake, X.-Q. Yang, K.-W. Nam, L. Zhang, M. Shao. *J. Power Sources* 277, 2015, p. 193-197.
- [98]. Goodenough, J. B. *J. Solid State Electrochem.* 16, 2012, p. 2019-2029.
- [99]. R. Tripathi, G. Popov, X. Sun, D. H. Ryan, L. F. Nazar. *J. Mater. Chem. A.* 1, 2013, p. 2990-2994.
- [100]. B. L. Ellis, T. N. Ramesh, W. N. Rowan-Weetaluktuk, D. H. Ryan, L. F. Nazar. *J. Mater. Chem.* 22, 2012, p. 4759-4766.
- [101]. P. Barpanda, M. Ati, B. V. Melot, G. Rousse, J.-N. Chotard, M.-L. Doublet, M. T. Sougrati, S. A. Corr, J.-C. Jumas, J.-M. Tarascon. *Nat. Mater.* 10, 2011, p. 772-779.
- [102]. H. Y. Tran, C. Täubert, M. Fleischhammer, P. Axmann, L. Küppers, M. Wohlfahrt-Mehrens. *J. Electrochem. Soc.* 158, 2011, p. A556-561.
- [103]. A. J. Smith, S. R. Smith, T. Byrne, J. C. Burns, J. R. Dahn. *J. Electrochem. Soc.* 159, 2012, p. A1696-A1701.
- [104]. S. B. Chikkannanavar, D. M. Bernardi, L. Liu. *J. Power Sources* 248, 2014, p. 91-100.
- [105]. T. R. Jow, M. S. Ding, K. Xu, S. S. Zhang, J. L. Allen, K. Amine, G. L. Henriksen. *J. Power Sources* 119-121, 2009, p. 343-348.
- [106]. J. M. Tarascon, D. Guyomard. *Solid State Ionics* 69, 1994, p. 293-305.
- [107]. K. Xu, S. P. Ding, T. R. Jow. *J. Electrochem. Soc.* 146, 1999, p. 4172-4178.
- [108]. W. Xu, X. Chen, F. Ding, J. Xiao, D. Wang, A. Pan, J. Zheng, X. S. Li, A. B. Padmaperuma, J.-G. Zhang. *J. Power Sources* 213, 2012, p. 304-316.
- [109]. Xu, K. *Chem. Rev.* 104, 2004, p. 4303-4417.
- [110]. G. G. Eshetu, S. Grugeon, G. Gachot, D. Mathiron, M. Armand, S. Laruelle. *Electrochim. Acta* 102, 2013, p. 133-141.

- [111]. **P. Murmann, P. Niehoff, R. Schmitz, S. Nowak, H. Gores, N. Ignatiev, P. Sartori, M. Winter, R. Schmitz.** *Electrochim. Acta* 114, 2013, p. 658-666.
- [112]. **L. Zhou, B. L. Lucht.** *J. Power Sources* 205, 2012, p. 439-448.
- [113]. **S. E. Sloop, J. K. Pugh, S. Wang, J. B. Kerr, K. Kinoshita.** *Electrochem. Solid-State Lett.* 4, 2001, p. A42-A44.
- [114]. **N. Kamaya, K. Homma, Y. Yamakawa, M. Hirayama, R. Kanno, M. Yonemura, T. Kamiyama, Y. Kato, S. Hama, K. Kawamoto, A. Mitsui.** *Nat. Mater.* 10, 2011, p. 682-686.
- [115]. **Masquelier, C.** *Nat. Mater.* 10, 2011, p. 469-650.
- [116]. **Fergus, J. W.** *J. Power Sources* 195, 2010, p. 4559-4569.
- [117]. **L. Damen, M. Lazzari, M. Mastragostino.** *J. Power Sources* 19, 2011, p. 8692-8695.
- [118]. **A. Barré, B. Deguilhem, S. Grollequ, M. Gérard, F. Suard, D. Riu.** *J. Power Sources* 241, 2013, p. 680-689.
- [119]. **C. L. Champion, W. Li, B. L. Lucht.** *J. Electrochem. Soc.* 152, 2005, p. A2327-A2334.
- [120]. **J. Yamaki, Y. Shinjo, T. Doi, S. Okada, Z. Ogumi.** *J. Electrochem. Soc.* 162, 2015, p. A520-A530.
- [121]. **X.-G. Teng, F.-Q. Li, P.-H. Ma, Q.-D. Ren, S.-Y. Li.** *Thermochim. Acta* 436, 2005, p. 30-34.
- [122]. **B. Ravdel, K. M. Abraham, R. Gitzendanner, J. DiCarlo, B. Lucht, C. Champion.** *J. Power Sources* 119-121, 2003, p. 805-810.
- [123]. **H. Yang, G. V. Zhuang, P. N. Ross Jr.** *J. Power Sources* 161, 2006, p. 573-579.
- [124]. **J. S. Gnanaraj, E. Zinigrad, L. Asraf, H. E. Gottlieb, M. Sprecher, M. Schmidt, W. Geissler, D. Aurbach.** *J. Electrochem. Soc.* 150, 2003, p. A1533-A1537.
- [125]. **S. Wilken, M. Treskow, J. Scheers, P. Johansson, P. Jacobsson.** *RSC Advances* 3, 2013, p. 16359-16364.
- [126]. **A. Xiao, W. Li, B. L. Lucht.** *J. Power Sources* 162, 2006, p. 1282-1288.
- [127]. **S. E. Sloop, J. B. Kerr, K. Kinoshita.** *J. Power Sources* 119-121, 2003, p. 330-337.
- [128]. **T. Kawamura, S. Okada, J. Yamaki.** *J. Power Sources* 156, 2006, p. 547-554.
- [129]. **L. Terborg, S. Weber, F. Blaske, S. Passerini, M. Winter, U. Karst, S. Nowak.** *J. Power Sources* 242, 2013, p. 832-837.
- [130]. **S. F. Lux, I. T. Lucas, E. Pollak, S. Passerini, M. Winter, R. Kostecki.** *Electrochem. Commun.* 14, 2012, p. 47-50.
- [131]. **S. F. Lux, J. Chevalier, I. T. Lucas, R. Kostecki.** *Electrochem. Lett.* 2, 2013, p. A121-A123.
- [132]. **U. Heider, R. Oesten, M. Jungnitz.** *J. Power Sources* 81-82, 1999, p. 191-122.
- [133]. **Peled, E.** *J. Power Sources* 9, 1983, p. 253-266.

- [134]. **D. Aurbach, Y. Ein-Eli, B. Markovsky, A. Zaban, S. Luski, Y. Carmeli, H. Yamin.**
J. Electrochem. Soc. 142, 1995, p. 2882-2890.
- [135]. **P. Verma, P. Maire, P. Novák.** *Electrochim. Acta* 55, 2010, p. 6332-6341.
- [136]. **E. Peled, D. B. Tow, A. Merson, A. Gladkikh L. Burstein, D. Golodnitsky.** *J. Power Sources* 97-98, 2001, p. 52-57.
- [137]. **D. Aurbach, B. Markovsky, A. Shechter, Y. Ein-Eli, H. Cohen.** *J. Electrochem. Soc.* 143, 1996, p. 3809-3820.
- [138]. **V. A. Agubra, J. W. Fergus.** *J. Power Sources* 268, 2014, p. 153-162.
- [139]. **Aurbach, D.** *J. Power Sources* 89, 2000, p. 206-218.
- [140]. **D. Aurbach, K. Gamolsky, B. Markovsky, Y. Gofer, M. Schmidt, U. Heider.** *Electrochim. Acta* 47, 2002, p. 1423-1439.
- [141]. **H. Ota, Y. Sakata, A. Inoue, S. Yamaguchi.** *J. Electrochem. Soc.* 151, 2004, p. A1659-A1669.
- [142]. **J. Vetter, P. Novák, M. R. Wagner, C. Veit, K.-C. Möller, J. O. Besenhard, M. Winter, M. Wohlfahrt-Mehrens, C. Vogler, A. Hammouche.** *J. Power Sources* 147, 2005, p. 269-281.
- [143]. **X. Xiao, Z. Liu, L. Baggetto, G. M. Veith, K. L. More, R. R. Unocic.** *Phys. Chem. Chem. Phys.* 16, 2014, p. 10398-10402.
- [144]. **A. Hammami, N. Raymond, M. Armand.** *Nature* 424, 2003, p. 635-636.
- [145]. **G. Gachot, S. Grugeon, G. G. Eshetu, D. Mathiron, P. Ribière, M. Armand, S. Laruelle.**
Electrochim. Acta 83, 2012, p. 402-409.
- [146]. **W. Li, B. L. Lucht.** *J. Electrochem. Soc.* 153, 2006, p. A1617-A1625.
- [147]. **K. Edström, T. Gustafsson, J. O. Thomas.** *Electrochim. Acta* 50, 2004, p. 397-403.
- [148]. **D. Aurbach, B. Markovsky, G. Salitra, E. Markevich, Y. Talyossef, M. Koltypin, L. Nazar, B. Ellis, D. Kovacheva.** *J. Power Sources* 165, 2007, p. 491-499.
- [149]. **L. Liao, X. Cheng, Y. Ma, P. Zuo, W. Fang, G. Yin, Y. Gao.** *Electrochim. Acta* 87, 2013, p. 466-472.
- [150]. **M. Wohlfahrt-Mehrens, C. Vogler, J. Garche.** *J. Power Sources* 127, 2004, p. 58-64.
- [151]. **H. Tsunekawa, S. Tanimoto, R. Marubayashi, M. Fujita, K. Kifune, M. Sano.**
J. Electrochem. Soc. 149, 2002, p. A1326-A1331.
- [152]. **P. Arora, Z. J. Zhang.** *Chem. Rev.* 104, 2004, p. 4419-4462.
- [153]. **Zhang, S. S.** *J. Power Sources* 164, 2007, p. 351-364.
- [154]. **M. Kirchhöfer, J. v. Zamory, E. Paillard, S. Passerini.** *Int. J. Mol. Sci.* 15, 2014, p. 14868-14890.
- [155]. **M. M. Thackeray, C. Wolverton, E. D. Isaacs.** *Energy Environ. Sci.* 5, 2012, p.7854-7863.

- [156]. **Abraham, K. M.** *J. Phys. Chem. Lett.* 6, 2015, p. 830-844.
- [157]. **B. Scrosati, J. Garche.** *J. Power Sources* 195, 2010, p. 2419-2430.
- [158]. **V. Srinivasan, J. Newman.** *J. Electrochem. Soc.* 151, 2004, p.A1530-A1538.
- [159]. **Z. Chen, J. R. Dahn.** *J. Electrochem. Soc.* 149, 2002, p. A1184-A1189.
- [160]. **S.-Y. Chung, J. T. Bloking, Y.-M. Chiang.** *Nat. Mater.* 1, 2002, p. 123-128.
- [161]. **A. V. Murugan, T. Muraliganth, A. Manthiram.** *J. Phys. Chem. C* 112, 2008, p. 14665-14671.
- [162]. **K. Lee, I.-B. Shim, C. S. Kim.** *J. Appl. Phys.* 107, 2010, p. 09A522-1-09A522-3.
- [163]. **A. S. Andersson, B. Kalska, J. Häggström, J. O. Thomas.** *Solid State Ionics* 130, 2000, p. 41-52.
- [164]. **J.-K. Kim, G. Cheruvally, J.-J. Ahn, H.-J. Ahn.** *J. Phys. Chem. Solids* 69, 2008, p. 1257-1260.
- [165]. **S. Franger, F. L. Cras, C. Bourbon, H. Rouault.** *Electrochem. Solid-State Lett.* 5, 2002, p. A231-A233.
- [166]. **A. F. Holleman, E. and N. Wiberg.** *Lehrbuch der Anorganischen Chemie.* Germany : Walter de Gruyter, 2007. p. 1636-1645.
- [167]. **S. K. Martha, J. Grinblat, O. Haik, E. Zinigrad, T. Drezen, J. H. Miners, I. Exnar, A. Kay, B. Markovsky, D. Aurbach.** *Angew. Chem. Int. Ed.* 48, 2009, p. 8559-8563.
- [168]. **W. Weppner, R. A. Huggins.** *J. Solid State Chem.* 22, 1977, p. 279-308.
- [169]. **N. N. Bramnik, K. Nikolowski, C. Baethz, K. G. Bramnik, H. Ehrenberg.** *Chem. Mater.* 19, 2007, p. 908-915.
- [170]. **K. Amine, H Yasuda, M. Yamachi.** *Electrochem. Solid-State Lett.* 2000, Bd. 3, p. 178-179.
- [171]. **Eftekhari, A.** *J. Electrochem. Soc.* 151, 2004, p. A1456-A1460.
- [172]. **M. Zanetti, G. Camino, P. Reichert, R. Mülhaupt.** *Macromol. Rapid Commun.* 22, 2001, p. 176-180.
- [173]. **Y. Tsuchiya, K. Sumi.** *J. Polym. Sci. A-1.* 1969, Bd. 7, p. 1599-1607.
- [174]. **H. Bockhorn, A. Hornung, U. Hornung, D. Schawaller.** *J. Anal. Appl. Pyrol.* 48, 1999, p. 93-109.
- [175]. **K. O. Christe, W. W. Wilson.** *J. Fluorine Chem.* 46, 1990, p. 339-342.
- [176]. **A. A. Pande, G. Levitin, D. W. Hess.** *J. Electrochem. Soc.* 157, 2010, p. G147-G153.
- [177]. **V. Ebsworth, J. Turner.** *J. Phys Chem.* 67, 1963, p. 805-807.
- [178]. **Q. Wu, W. Lu, J. Parkash.** *J. Power Sources* 88, 2000, p. 237-242.
- [179]. **J. R. Belt, D. M. Bernardi, V. Utgikar.** *J. Electrochem. Soc.* 161, 2014, p. A1116-A1126.
- [180]. **G. Q. Liu, H. T. Kuo, R. S. Liu, C. H. Shen, D. S. Shy, X. K. Xing, J. M. Chen.** *J. Alloys Compd.* 496, 2010, p. 512-516.

5.4 Parts of publication of the doctoral thesis

1. **P. Handel, G. Fauler, K. Kapper, M. Schmuck, C. Stangl, R. Fischer, F. Uhlig, S. Koller.**
J. Power Sources 267, 2014, p. 255-259.
2. **P. Handel, C. Stangl, C. God, M. Filzwieser, F. Uhlig, H. Schroettner, S. Koller.**
ECS Trans. 66, 2015, *accepted*.